



Characterization of methane adsorption in shales using low-field NMR

By

Kaishuo Yang

Supervisors:

Professor Michael L. Johns

Professor Eric F. May

Doctor Ming Li

Fluid Science & Resources Research Group

School of Engineering

Department of Chemical Engineering

*This thesis is presented for the degree of Doctor of Philosophy of The
University of Western Australia*

2022

Thesis Declaration

I, Kaishuo Yang, certify that:

This thesis has been substantially accomplished during enrolment in this degree.

This thesis does not contain material which has been submitted for the award of any other degree or diploma in my name, in any university or other tertiary institution.

In the future, no part of this thesis will be used in a submission in my name, for any other degree or diploma in any university or other tertiary institution without the prior approval of The University of Western Australia and where applicable, any partner institution responsible for the joint-award of this degree.

This thesis does not contain any material previously published or written by another person, except where due reference has been made in the text and, where relevant, in the Authorship Declaration that follows.

This thesis does not violate or infringe any copyright, trademark, patent, or other rights whatsoever of any person.

This thesis contains published word and/or work prepared for the publication, some of which has been co-authored.

Signature:

A solid black rectangular box used to redact the author's signature.

Date: 10 Feb 2022

Abstract

Natural gas production from unconventional shale gas reservoirs has gained increasing worldwide focus, spurred largely by improvements in production techniques. Gas storage in shale preliminarily consists of a combination of three types: (1) free natural gas within pores and fractures; (2) adsorbed natural gas on nano-scale organic pore surfaces and (3) effectively dissolved natural gas in hydrocarbon liquids and other formation fluids. Knowledge that allows for accurate estimation of both adsorbed and free gas in shale is critical to the prediction of gas-in-place and hence potential hydrocarbon productions. Moreover, unlike conventional hydrocarbon reservoirs, shales feature both comparatively low porosity and permeability with a significant semi-solid organic content and complex nanostructures, leading to much more complex experimental characterizations of shale. The work presented in this dissertation thus ultimately aims at the characterization and quantitative estimation of natural gas content in shale cores using low-field NMR relaxometry techniques.

Molecular diffusion is a critical transport phenomenon of hydrocarbons in heterogeneous porous media such as carbonates and shales. ‘Diffusive’ tortuosity (τ_d), which is defined as the ratio of the bulk fluid diffusion coefficient to the restricted diffusion coefficient was initially measured in heterogeneous carbonate rock cores ranging in permeability from 2 to 5300 mD, hopefully as a precursor to shales but interesting in their own right as heterogeneous rock cores, applying pulsed field gradient (PFG) nuclear magnetic resonance (NMR) methodology to measure τ_d . Supercritical methane was adapted as the probe molecule with ‘diffusive tortuosity’ shown to be independent of both pressure and diffusion observation time for the selected range of conditions, as required. The resultant ‘diffusive’ tortuosity measurements (which ranged from 3.1-5.6) were then compared against independent electrical conductivity measurements of tortuosity using a two-electrode impedance technique applied to the carbonate samples saturated with brine solution. Agreement between the ‘diffusive tortuosity’, as measured by PFG NMR, and ‘electrical’ tortuosity was remarkably good (within 10%).

Following on from this, characterization of shale rocks in terms of semi-solid bitumen and capillary trapped water in organic/inorganic pores was made using NMR techniques. This was applied to a range of shale samples with variable moisture content (realized via variable system relative humidity) in an attempt to assess the accuracy of such an approach to delineate the inherent, predominantly bitumen signal from that of the added water. NMR free induction

decay (FID) and Carr-Purcell-Meilboom-Gill (CPMG) measurements were conducted at a range of ^1H NMR frequencies (20, 40 and 60 MHz) and the consequential spliced data were interpreted using a combined Gaussian and exponential inversion method. Consistently, the Gaussian component of the resultant T_2^*/T_2 distribution was found to be independent of moisture content, scaling rather with the total organic content of the respective shale cores. In contrast, the exponential component of the resultant T_2^*/T_2 distribution was found to scale linearly with the moisture content of the shale cores.

Dynamics of ethane confined to mesoporous silica materials exhibiting mean pore diameters between 6 and 50 nm were measured using low-field (12.7 MHz) ^1H NMR relaxation measurements; such pore length-scales are broadly consistent with gas adsorption in shales. NMR-based isotherms within the range 25-50 bar and at ambient temperature were acquired and incorporated the ethane condensation point. NMR-derived excess adsorption capacities were observed to be in excellent agreement with *ex-situ* gravimetric ethane adsorption measurements. The application of T_2 and diffusion coefficient distribution measurements was demonstrated to be a consistent delineator of meso-pore adsorption and inter-particle occupation.

Finally, methane excess adsorption capacities were quantitatively characterized using low-field (12.7 MHz) NMR measurements in two intact shale rocks at a temperature of 24 °C with pressure up to 150 bar. The resultant transverse relaxation time (T_2) spectra indicate three distinct peaks with peak P1 ($T_2 < 1$ ms) representing adsorbed methane in organic pores, peak P2 ($T_2=1-10$ ms and $10-100$ ms for two different shale rock samples) indicating gas methane constrained in inorganic pores and peak P3 (with the longest T_2) corresponding to bulk gas methane in fractures. The shale sample featuring lower total organic content (TOC) but higher clay mineral content showed greater adsorption capacities compared to the organic-rich shale sample, suggesting that clay minerals rather than TOC contribute to additional surface area and hence larger adsorption capacity in this limited study. NMR-based methane excess adsorption isotherms using a combination of mass balance calculation and integrals of NMR peaks P2 and P3 were compared to those from *ex-situ* gravimetric method with excellent agreement observed. However, the integrated amplitudes of the adsorbed phase (peak P1) displayed nearly identical trends with the independent measurements, there was a pressure-independent loss of NMR signal from adsorbed methane components with comparatively short T_2 times.

Contents

| | |
|--|-----------|
| Thesis Declaration..... | 2 |
| Abstract..... | 3 |
| Contents | 5 |
| List of Tables | 9 |
| List of Figures..... | 10 |
| Acknowledgements | 14 |
| Authorship Declaration: Co-Authored Publications..... | 16 |
| Chapter 1 Thesis Introduction..... | 20 |
| 1.1 Introduction..... | 20 |
| 1.2 Research focus | 21 |
| 1.3 Dissertation Outline | 22 |
| 1.4 References..... | 24 |
| Chapter 2 Quantitative Tortuosity Measurements of Carbonate Rocks Using Pulsed Field Gradient NMR | 28 |
| 2.1 Abstract..... | 28 |
| 2.2 Introduction..... | 29 |
| 2.3 Background..... | 30 |
| 2.3.1 Dispersion and Tortuosity | 30 |
| 2.3.2 Tortuosity definitions | 31 |
| 2.4 Experimental Details | 35 |
| 2.4.1 NMR diffusion measurements..... | 36 |
| 2.4.2 Electrical Measurements | 39 |
| 2.5 Results and Discussion | 40 |

| | |
|--|-----------|
| 2.5.1 X-ray CT Density Images..... | 40 |
| 2.5.2 Self-diffusion Coefficient Measurements..... | 42 |
| 2.5.3 ‘Electrical’ Tortuosity | 47 |
| 2.6 Conclusions..... | 49 |
| 2.7 References..... | 49 |
| Chapter 3 Shale Rock Core Analysis using NMR: Effect of bitumen and water content | 57 |
| 3.1 Abstract..... | 57 |
| 3.2 Introduction..... | 58 |
| 3.3 Background..... | 60 |
| 3.4 Experimental Details | 64 |
| 3.4.1 Shale Samples – Description and Preparation..... | 64 |
| 3.5 Results and Discussion | 66 |
| 3.5.1 Spliced FID and CPMG Data | 66 |
| 3.5.2 Moisture Content Correlation..... | 69 |
| 3.5.3 Organic Matter Correlation | 71 |
| 3.5.4 Influence of ¹ H NMR Measurements Frequency | 72 |
| 3.6 Conclusions..... | 74 |
| 3.7 References..... | 74 |
| Chapter 4 Low-field NMR Relaxation Analysis of Ethane Adsorption in Mesoporous Silicas..... | 82 |
| 4.1 Abstract..... | 82 |
| 4.2 Introduction..... | 83 |
| 4.3 Theoretical Background..... | 85 |
| 4.3.1 Adsorption and Capillary Condensation | 85 |
| 4.3.2 NMR Relaxation and Diffusion in Porous Media | 86 |
| 4.4 Experimental section | 87 |
| 4.4.1 Materials | 87 |

| | |
|---|------------|
| 4.4.2 Material Characterization | 87 |
| 4.4.3 NMR measurements | 88 |
| 4.4.4 NMR Data Processing | 92 |
| 4.4.5 Gravimetric Adsorption Measurements | 92 |
| 4.5 Results and Discussion | 94 |
| 4.5.1 Bulk Ethane Measurements | 94 |
| 4.5.2 Initial Material Characterization..... | 96 |
| 4.5.3 NMR Ethane Adsorption Measurements..... | 97 |
| 4.6 Conclusions..... | 104 |
| 4.7 References..... | 104 |
| Chapter 5 Quantitative Characterization of Methane Adsorption in Shale Using Low-field NMR | 112 |
| 5.1 Abstract..... | 112 |
| 5.2 Introduction..... | 113 |
| 5.3 NMR Background..... | 115 |
| 5.4 Experimental Section..... | 116 |
| 5.4.1 Materials | 116 |
| 5.4.2 Total Organic Content | 117 |
| 5.4.3 Scanning Electron Microscopy..... | 117 |
| 5.4.4 Nitrogen Adsorption/Desorption Isotherms | 120 |
| 5.4.5 Gravimetric Adsorption..... | 122 |
| 5.4.6 NMR Experiments..... | 123 |
| 5.5 Results and Discussion | 125 |
| 5.5.1 Bulk Methane Calibration | 125 |
| 5.5.2 NMR T_2 Distributions and T_1 - T_2 Maps of Methane in Shales..... | 126 |
| 5.5.3 Evaluation of Methane Adsorption | 129 |
| 5.6 Conclusions..... | 132 |

| | |
|---|------------|
| 5.7 References..... | 133 |
| Chapter 6 Conclusions and Future Work | 137 |
| 6.1 Conclusions..... | 137 |
| 6.2 Future Work..... | 139 |
| 6.2.1 Impact of organic content and clay minerals on methane adsorption capacities in shales | 139 |
| 6.2.2 NMR measurements of ethane saturated shales | 139 |
| 6.2.3 CO ₂ -CH ₄ displacement in shales for enhance gas recovery (EGR) | 140 |
| 6.2.4 References | 141 |

List of Tables

| | |
|---|-----|
| Table 2.1. Petro-physical properties of the carbonate rock cores. | 36 |
| Table 2.2. NMR APGSTE experiment parameters. | 39 |
| Table 2.3. Log-mean T_1 and T_2 relaxation times for Methane. | 42 |
| Table 2.4. Diffusion coefficient and ‘diffusive’ tortuosity for bulk methane and the four carbonate rock cores as a function of pressure | 45 |
| Table 2.5. ‘Electrical’ resistivity and tortuosity..... | 47 |
| Table 4.1. Material textural properties of mesoporous CARiACT Q6, Q15 and Q50 silicas. | 88 |
| Table 4.2. Silica bed porosity data obtained from NMR measurements of water saturated samples. Intraparticle and interparticle porosity values represent the percentage of the total porosity found within the intraparticle mesopores and interparticle spaces, respectively..... | 97 |
| Table 5.1. Summary of results from nitrogen adsorption/desorption measurements..... | 121 |

List of Figures

Figure 1.1. (a) U.S. natural gas production and (b) U.S natural gas production by type in 2020.20

Figure 2.1. Schematic plot of normalized dispersion coefficient against Péclet number for a typical porous media with a grain size of d_p31

Figure 2.2. Diffusion coefficient of brine solution restricted in a Berea sandstone rock core. The blue dash line indicates the inverse tortuosity asymptote.34

Figure 2.3. Schematic of the NMR tortuosity measurement apparatus. The red arrows indicate the direction of flow for methane and confining fluid respectively.37

Figure 2.4. The “13-interval” APGSTE pulse sequence used for diffusion measurements in rock cores.38

Figure 2.5. X-ray CT scan images of carbonate rock core (a) Estailades, (b) Indiana, (c) Ketton, (d) Portland. The yellow lines indicate the overall 3D bulk dry density profile.41

Figure 2.6. NMR signal attenuation of bulk methane at various experimental pressures. The dashed lines indicate the fit of **Equation (2.11)**.43

Figure 2.7. Methane free diffusion coefficient as a function of pressure, as acquired in this work and from literature data.44

Figure 2.8. Sample NMR PFG signal attenuation data for restricted self-diffusion coefficient of methane at 20 °C in the Estailades carbonate sample as a function of pressure.45

Figure 2.9. Restricted diffusion coefficient of methane as a function of observation time Δ at pressures of 50 and 100 bar for carbonate rock (a) Estailades, (b) Ketton, (c) Portland and (d) Indiana respectively. The dashed lines indicate the corresponding tortuosity asymptotes.47

Figure 2.10. Comparison of ‘diffusive’ and ‘electrical’ tortuosity for all four carbonate samples. The solid line is the line of equivalence.48

Figure 2.11. Photo of Indiana carbonate rock core; substantial pores can be observed on the core surface.49

Figure 3.1. Mass changes (wt. %) of shale rock cores with relative humidity (RH) due to moisture adsorption.65

Figure 3.2. Bruker Minispec NMR spectrometer with multiple magnets providing ^1H NMR frequencies of 10 (not used in this study), 20, 40 and 60 MHz, respectively.66

Figure 3.3. Signal attenuation fitted with the simultaneous Gaussian and Exponential (SGE) method (**Equation (3.4)**) – the full fit) for a shale sample at an NMR frequency of 40 MHz and at a relative humidity of 99 %.67

Figure 3.4. (a) Relaxation time distribution of spliced FID and CPMG method for a shale rock core sample measured at 40 MHz as a function of relative humidity. (b) Area of each of the three peaks as a function of relative humidity. 68

Figure 3.5. Calibrated NMR equivalent H₂O volume vs. gravimetrically measured H₂O uptake. Results are from data measured at 40 MHz. 70

Figure 3.6. (a) Integrated Gaussian and exponential component area changes from spliced signal decays as a function of sample mass for shale rock core sample at a measured NMR frequency of 40 MHz. (b) Variation in the respective exponential peak areas as a function of sample mass (and hence moisture content). (c) and (d) Data for another shale sample showing very consistent results. 71

Figure 3.7. Correlation of Gaussian peak signal (area) with independently measured organic matter content of shale rock cores. 72

Figure 3.8. Standard deviation of the Gaussian component area (as determined across the different relative humidities applied) for different NMR frequencies. 73

Figure 4.1. BJH pore size distributions of mesoporous CARiACT Q6, Q15 and Q50 silicas. 88

Figure 4.2. Schematic of the experimental apparatus employed to perform NMR measurements. 89

Figure 4.3. NMR radio frequency (RF) pulse sequence diagram for (a) CPMG measurements and (b) PGSTE measurements. Thick and thin bars represent 180° and 90° RF pulses, respectively, while white data points indicate the recorded echo magnitudes. In (b) gradient pulse timings (G axis) are given according to the notation of Tanner (Tanner, 1970). 91

Figure 4.4. Schematic of the experimental apparatus used for gravimetric adsorption measurements. 94

Figure 4.5. (a) Direct correlation of bulk ethane saturation pressure data (obtained from NIST) with measured NMR signal magnitudes. (b) Ethane density evolution as a function of pressure. 95

Figure 4.6. T₂ relaxation distributions obtained from water saturated packed beds of mesoporous Q-silicas. 97

Figure 4.7. Calibrated NMR isotherms of ethane in the mesoporous silicas Q6, Q15 and Q50, as compared to the bulk. Fully reversible isotherms are seen across all silica materials. 99

Figure 4.8. Direct comparison of the excess gas phase ethane adsorption capacities *q_{ex}* obtained via NMR and gravimetric measurements at pressures between 25 bar and 39 bar. 101

Figure 4.9. (a) T_2 distributions acquired from ethane in a packed bed of Q15 silica as a function of pressure between 31 bar and 44 bar. (b) Integrated NMR signal intensities for the two T_2 populations present within the gas phase (pressure <40 bar). (c) Diffusion distributions for ethane in Q15 silica within the same pressure range. (d) Integrated NMR signal intensities for components in diffusion distributions. (e) Direct comparison between relaxation and diffusion derived absolute intraparticle gas phase ethane capacities, demonstrating excellent agreement. 103

Figure 5.1. Tescan Oxford SEM EDS (left) and freshly fractured surface of shale samples (right). 118

Figure 5.2. (a) SEM image and (b) elemental map around an organic inclusion in the Mancos shale sample. The shale matrix is dominated by clay with minor carbonate and apatite content. 118

Figure 5.3. SEM images of the Mancos sample showing (a) structured organic matter imbedded in a shale matrix, (b) amorphous organic matter within framboidal pyrite, and (c) same spectrum point as shown in **Figure 5.3(b)** taken with secondary electron image showing organic matter interbedded with clay platelets. 119

Figure 5.4. SEM images of (a) the EF shale, (b) corresponding elemental map of **Figure 5.4(a)**, microfossils sitting between larger apatite and crystalline carbonate grains; (c) zoomed in shot of the microfossils for the EF shale, and (d) corresponding elemental map of **Figure 5.4(c)**. Organic matter is hosted in microfossil matrix with occasional framboidal pyrite. 120

Figure 5.5. Nitrogen adsorption and desorption isotherms for (a) Mancos and (b) EF samples at a temperature of 77K. 121

Figure 5.6. Schematic of experimental apparatus used in the NMR measurements. 124

Figure 5.7. Schematic of the NMR pulse sequences for (a) CPMG measurements and (b) T_1 - T_2 inversion recovery-CPMG measurements. Thin and thick vertical bars represent 90° and 180° RF pulses, respectively. The echo time $T_E=2\tau_2$ and a range of τ_1 is repeated for the T_1 - T_2 measurements to encode T_1 125

Figure 5.8. (a) T_2 spectra of bulk gas methane at different pressures. (b) The correlation between the sum of signal intensity of T_2 peaks and molar quantity of bulk gas methane in the pressure range from 30 bar to 100 bar. 126

Figure 5.9. T_2 distributions of methane in (a) Mancos shale and (b) EF shale at different pressures. The P1 peaks of those two samples are reproduced in the inset as higher resolution. 127

Figure 5.10. Relationships between experimental pressures and the corresponding methane amount of T₂ peaks of adsorbed methane in organic pores (P1), free gas methane in larger inorganic pores (P2) and bulk gas methane in fractures (P3) for (a) the Mancos shale and (b) the EF shale. Note P1 and P3 are plotted on the secondary vertical axis with different scales. Error bars for peak P1 are sourced from repeated NMR experiments..... 128

Figure 5.11. T₁-T₂ maps of methane in (a) the Mancos shale at 50 bar, (b) the Mancos shale at 100 bar, (c) the EF shale at 50 bar and (d) the EF shale at 100 bar. 129

Figure 5.12. Comparison of excessive methane adsorption in (a) the Mancos shale and (b) the EF shale as a function of pressure. Blue circles are data obtained from gravimetric method; red crosses are sourced from the NMR peak P1 integrals; green squares are the normalized NMR peak P1 integrals by multiplying a constant. 130

Figure 5.13. Excessive methane adsorption in (a) the Mancos shale and (b) the EF shale as a function of pressure. Blue circles are data obtained from gravimetric method; orange rhombuses represent adsorption data acquired from the combination of mass balance calculation and the corresponding methane quantity obtained from the integrated areas of NMR peaks P2 and P3 in **Figure 5.9**..... 132

Acknowledgements

First and foremost, I would like to express my sincere gratitude to my supervisor Prof. Michael Johns for offering me this precious opportunity to start my PhD work in the Fluid Science and Resources research group at The University of Western Australia. Thank you for your guidance, patience, support, suggestions, encouragement and help with revising and completing the published papers in this thesis.

I would also like to thank my co-supervisor Prof. Eric May for the academic discussions and technical suggestions during every group meeting. I have benefited greatly from your support and guidance.

To my co-supervisor Dr. Ming Li, sincerely appreciate your great help with those complex and challenging experiments in labs. Thank you for your patient introduction to those NMR concepts and experimental instruments when I started my PhD work. Thanks for your time and guidance.

I would like to thank Dr. Paul Connolly, Dr. Neil Robinson, Dr. Nicholas Ling, Mr. Bin Yan and Mr. Razyq Nasharuddin for their help in so many ways. Paul, thanks for helping me design and build up the complex experimental setup and sharing your wonderful and exciting life experiences to me. Neil, appreciate your patience and professions when modifying my manuscripts, I have learnt a lot from you. Nick, thanks for helping me solve those tough questions when using those NMR instruments. Bin, thanks for spending your time walking around the ARRC building with me to take a deep breath of the fresh air. Razyq, it is always a wonderful and relaxing time to have lunch together with you. I also thank you all the FSR members who have helped me.

To my parents, thank you for providing me with opportunities to receive better educations and supporting me to study my PhD in Australia. You encourage me to overcome all the challenges and always be positive to life. Dad, thanks for letting me form the good learning habit and sorry for not having time to accompany you on fishing. Mum, thanks for your weekly chat and unwavering support for both my life and study.

To Siqi Chen, my partner, thanks for your warm support and accompany in my life to help me climb the mountain of PhD journey. Thanks for your understanding and caring in the four-year PhD study. I would not have completed this thesis without her strong support.

The PhD financial support from the Program of China Scholarship Council (No. 201708190001) is also gratefully acknowledged.

Authorship Declaration: Co-Authored Publications

In accordance with The University of Western Australia’s rules and regulations regarding Research Higher Degrees, this thesis has been organized as a series of publications.

The descriptions below summarize essential information regarding publications of which the candidate is the lead author. Chapters appear as published apart from style formatting and chapter referencing to ensure consistency and continuity throughout.

Paper 1

Yang, K., Li, M., Ling, N. N. A., May, E. F., Connolly, P. R. J., Esteban, L., Clennell, M. B., Mahmoud, M., El-Husseiny, A., Adebayo, A. R., Elsayed, M. M., & Johns, M. L. (2019). Quantitative Tortuosity Measurements of Carbonate Rocks Using Pulsed Field Gradient NMR. *Transport in Porous Media*, 130(3), 847–865. <https://doi.org/10.1007/s11242-019-01341-8>

Student’s Contribution to Work:

The student is the leading author of the publication. His contributions can be summarized as follows:

Development of NMR experiment protocols; Conducted NMR experimental work; Data processing and analysis; Drafting, redaction (with revisions from co-authors) and submission of the article.

Co-authors Signatures and Dates

Ming Li:



Date: 15 Feb 2022

Nicholas Ling:



Date: 15 Feb 2022

Eric F. May:



Date: 15 Feb 2022

Paul R.J. Connolly:



Date: 15 Feb 2022

Michael L. Johns:



Date: 15 Feb 2022

This manuscript appears as Chapter 2 in the thesis.

Paper 2

Yang, K., Connolly, P. R. J., Li, M., Seltzer, S. J., McCarty, D. K., Mahmoud, M., El-Husseiny, A., May, E. F., & Johns, M. L. (2020). Shale rock core analysis using NMR: Effect of bitumen and water content. *Journal of Petroleum Science and Engineering*, 195, 107847. <https://doi.org/10.1016/j.petrol.2020.107847>

Student's Contribution to Work:

The student is the leading author of the publication. His contributions can be summarized as follows:

Conducted NMR experimental work; Data analysis; Drafting, redaction (with revisions from co-authors) and submission of the article.

Co-authors Signatures and Dates

Paul R.J. Connolly:



Date: 15 Feb 2022

Ming Li:



Date: 15 Feb 2022

Eric F. May:



Date: 15 Feb 2022

Michael L. Johns:



Date: 15 Feb 2022

This manuscript appears as Chapter 3 in the thesis.

Paper 3

Yang, K., Sadeghi Pouya, E., Liu, L., Li, M., Yang, X., Robinson, N., May, E. F., & Johns, M. L. (2022). Low-Field NMR Relaxation Analysis of High-Pressure Ethane Adsorption in Mesoporous Silicas. *ChemPhysChem*, 23(4). <https://doi.org/10.1002/cphc.202100794>

Student's Contribution to Work:

The student is the leading author of the publication. His contributions can be summarized as follows:

NMR experiments; Data processing and analysis; Drafting, redaction (with revisions from co-authors) and submission of the article.

Co-authors Signatures and Dates

Ehsan Sadeghi Pouya:



Date: 15 Feb 2022

Libin Liu:



Date: 15 Feb 2022

Ming Li:



Date: 15 Feb 2022

Xiaoxian Yang:



Date: 15 Feb 2022

Neil Robinson:



Date: 15 Feb 2022

Eric F. May:



Date: 15 Feb 2022

Michael L. Johns:



Date: 15 Feb 2022

This manuscript appears as Chapter 4 in the thesis.

Paper 4

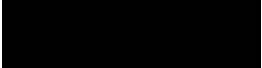
Yang, K., Connolly, P. R. J., Yang, X., Liu, L., Robinson, N., Li, M., Mahmoud, M., El-Husseiny, A., May, E. F., & Johns, M. L. (2022). Quantitative characterization of methane adsorption in shale using low-field NMR. In preparation, to be submitted to *Fuel*.

Student's Contribution to Work:

The student is the leading author of the publication. His contributions can be summarized as follows:

Sample preparations; NMR experiments; Data processing and analysis; Drafting, redaction (with revisions from co-authors) and submission of the article.

Co-authors Signatures and Dates

Paul R.J. Connolly:  Date: 15 Feb 2022

Xiaoxian Yang:  Date: 15 Feb 2022

Libin Liu:  Date: 15 Feb 2022

Neil Robinson:  Date: 15 Feb 2022

Ming Li:  Date: 15 Feb 2022

Eric F. May:  Date: 15 Feb 2022

Michael L. Johns:  Date: 15 Feb 2022

This manuscript appears as Chapter 5 in the thesis.

I, Michael L. Johns, certify that the student statements regarding the contributions to each of the work listed above are correct.

Coordinating supervisor signature: 

Date: 15 Feb 2022

Chapter 1 Thesis Introduction

1.1 Introduction

Successful implementation of technologies such as horizontal well drilling and hydraulic fracturing in unconventional hydrocarbon industries, has led to commercial production of hydrocarbons from shale reservoirs over the last two decades and the so called ‘Shale gas Revolution’ (Chen et al., 2019; Song & Kausik, 2019). According to the US Energy Information Administration (EIA), natural gas production of the USA has increased to approximately 35 trillion ft³ in 2020 and is estimated, despite the efforts to achieve net zero carbon emissions by 2050, to reach approximately 45 trillion ft³ in 2050 (U.S. Energy Information Administration, 2021). Among this production capacity, contributions from unconventional gas reservoirs have become one of the most significant energy supplies, accounting for more than 60% of the US total natural gas productions in 2020 and is predicted to steadily increase to represent virtually all natural gas production in the 2050s (U.S. Energy Information Administration, 2021). **Figure 1.1** presents the natural gas production and production by type in the US in 2020.

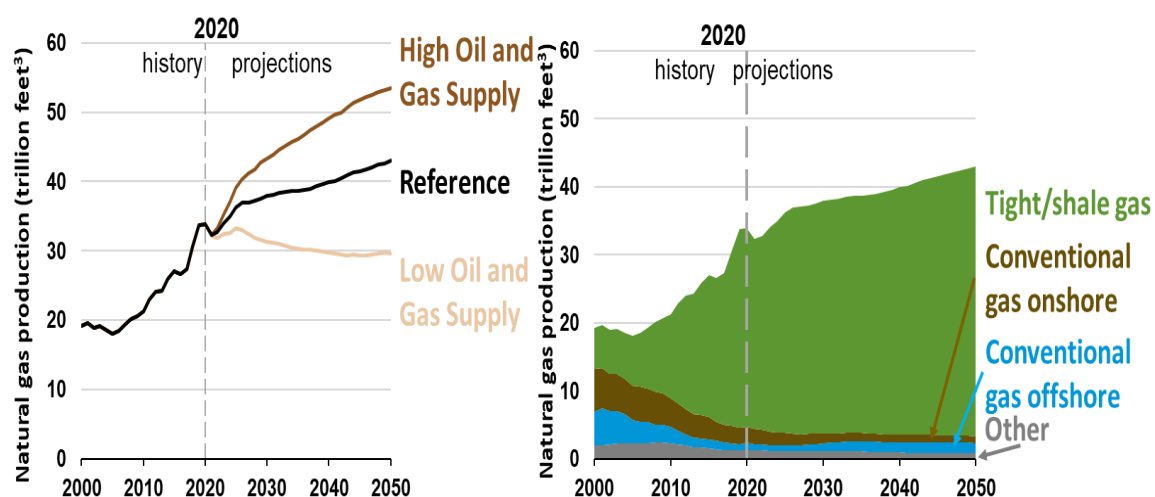


Figure 1.1. (a) U.S. natural gas production and (b) U.S. natural gas production by type in 2020.

For traditional sandstone or carbonate reservoirs, hydrocarbons migrate from source rocks through more permeable pathway to cap rocks due to buoyancy forces, where they accumulate. Shales are typically defined as fine-grained sedimentary rocks which contain

substantial organic matter or clays with porosities less than 10% and very low permeabilities; thus extractable hydrocarbons are effectively created in-place (Aplin & Macquaker, 2011; Washburn, 2014). The nanometer scale pore sizes in shales are several orders of magnitude smaller than those in conventional sandstones or carbonate, resulting in both challenging exploration and production (Ougier-Simonin et al., 2016). Moreover, due to the presence of immobile clay-bound water and organic matter such as kerogen and bitumen, the characterization of various components in shales becomes even more challenging (Song & Kausik, 2019). For gas-bearing shales, despite approximately 10% dissolved gas in residual fluids, the majority of shale gas appears as free gas confined in pores or fractures and adsorbed gas on organic pore surfaces (Curtis, 2002; Wang et al., 2019). The proportion of adsorbed gas varies widely from 40-85%, depending on the amount of organic content, its surface-to volume ratio, temperature, pressure etc. (Rani et al., 2015). Hence, accurate characterizations of shales and the adsorbed gas within them are critical to allow for more quantitative estimations of both shale reserves and their prospective productivity (Nikolaev & Kazak, 2019; Song & Kausik, 2019).

1.2 Research focus

Conventional methods employed to determine adsorbed gas content in shales are either gravimetric and volumetric based on various adsorption isotherms (Belmabkhout et al., 2004; Wu et al., 2019; Wu et al., 2015). Those techniques, however, can only provide information relevant to adsorbed components rather than free gas content and samples employed in those methods normally need to be crushed, resulting in potentially enhanced adsorption capacity whilst potentially destroying the original pore structure (Dick et al., 2017).

Nuclear magnetic resonance (NMR) has become a powerful technique to characterize the petro-physical properties of a variety of rocks due mainly to non-invasive detection and lithology-independent porosity estimation (Kleinberg, 2001). Such NMR applications include estimation of pore size distributions (Mitchell et al., 2013), identification of pore fluids (Hürlimann, 2012; Yuan et al., 2018), determination of wettability (Odusina et al., 2011; Sulucarnain et al., 2012) and estimation of permeability (AlGhamdi et al., 2013) for example. For conventional hydrocarbon rocks such as sandstone with negligible detectable hydrogen in the 'solid' matrix, the ^1H NMR signal originates from pore space fluids, enabling rock porosity to be accurately determined. However, shales are generally very heterogeneous with both

significant organic content and nano-scale to micro-scale pores in both the organic and inorganic phases (Minh et al., 2012). The organic content is composed of both kerogen and bitumen (which are broadly defined as being insoluble and soluble in organic solvents respectively). Whilst the ^1H NMR characteristics of this organic content corresponds to comparatively very short NMR relaxation times due to their very high viscosity (Loucks et al., 2009); bitumen (which generally features a comparatively lower molecular weight) in particular will provide some admittedly attenuated ^1H NMR signal intensity which is often comparable to that of any hydrocarbon content present in the pore space (Mehana & El-monier, 2016; Tinni et al., 2015). Separation of this bitumen signal is required in order to more accurately quantify system porosity and recoverable organic content. Characterizations of methane adsorption on crushed shales have been investigated in the literature to a limited extent using low-field NMR with the assumption that the adsorbed methane can be fully detected and the shortest T_2 is representative of adsorbed methane (Liu & Wang, 2018; Zhao & Wang, 2019). However, Yao *et al.* (2014) mentioned that adsorbed methane may only be partially detectable by low-field NMR and the correlation of T_2 amplitude to adsorbed methane may not be accurate. Hence, the broad aim of the thesis is to develop robust and accurate characterization techniques for shales including estimation of free and adsorbed gas within shale rock cores using low field ^1H NMR. To this end, a range of ‘model’ shale porous media systems (carbonates and nanoporous silicas) are also characterized by various NMR techniques for the purposes of NMR methodology development.

1.3 Dissertation Outline

This thesis is constructed as a series of three peer reviewed and published journal articles and one submitted journal article, corresponding to Chapter 2, 3, 4 and 5, respectively. The assembled structure of those chapters follows the progression of research work completed during this doctoral research, as such there is a coherent narrative focused on shale characterization using NMR, however each chapter is constructed around the respective standalone published or submitted articles.

In *Chapter 2*, NMR-based experimental hardware and protocols specifically for the measurements of high-pressure methane gas within porous media were designed and developed. These were applied to quantitatively measure diffusive tortuosity in heterogeneous carbonate rock cores ranging in permeability from 2 to 5300 mD using field gradient (PFG) NMR

methodology. Carbonate rocks include smaller pores and greater heterogeneity than sandstones and as such have greater similarity with shales; as such NMR methods are applied to them as well in this thesis. The resultant ‘diffusive’ tortuosity measurements for a range of carbonates were compared against independent electrical conductivity measurements of tortuosity using a two-electrode impedance technique applied to the carbonate samples saturated with brine solution. This represents one of the first direct comparisons of independent tortuosity measurement in such complex systems.

Chapter 3 demonstrates successful characterizations of bitumen and water content in a range of shale core samples with variable moisture content (provided by variable relative humidity environments) using multiple ^1H NMR detection frequencies (20, 40 and 60 MHz), which are applicable to more widely accessible bench-top NMR spectrometers. NMR free induction decay (FID) and Carr-Purcell-Meilboom-Gill (CPMG) measurements were conducted with the spliced data (a combination of both acquisitions) interpreted using a combined Gaussian and exponential inversion method. Correlations between integrated NMR signal intensities and bitumen content or capillary trapped water content were then considered. The impact of ^1H NMR frequency used across the range of 20 to 60 MHz on the consistency and accuracy of both Gaussian and exponential component signals was also analyzed and discussed.

As a precursor to subsequent studies on gas adsorption in shales, *Chapter 4* presents the characterization of ethane dynamics within mesoporous silica materials exhibiting mean pore diameters between 6 and 50 nm using low-field ^1H NMR relaxation measurements based on some of the experimental protocols established and developed in Chapter 2 and 3. NMR T_2 and diffusion coefficient distributions for the gas phase were acquired. These were interpreted so as to distinguish the adsorbed ethane (in fast exchange with intra-pore gas) within intraparticle mesopores in the sample and bulk gas ethane within interparticle pore space (between the particles). NMR-based ethane excess adsorption capacities were then compared against independently measured *ex-situ* gravimetric ethane adsorption measurements. NMR-based ethane adsorption isotherms within the range 25-50 bar and at ambient temperature which incorporated the ethane condensation point were thus systematically studied.

Chapter 5 provides quantitative characterization of both adsorbed and ‘free’ methane in two intact shale rock cores using low-field ^1H NMR techniques as were used in Chapter 2 and Chapter 3. NMR CPMG measurements were conducted at a temperature of 24 °C with

methane pressure up to 150 bar. T_1 - T_2 maps were also collected to support the 1D T_2 relaxation distribution interpretations. Three distinct peaks were evident in the acquired T_2 spectra as (from short to long T_2 times) adsorbed methane in organic pores (peak P1), ‘free’ (not adsorbed or absorbed) gas in inorganic pores (peak P2) and bulk gas methane in fractures (peak P3), respectively. Based on the method presented in Chapter 4 to correlate NMR signal with adsorbed and gas hydrocarbon amount, NMR-based methane excess adsorption isotherms were acquired based on the combination of mass balance calculation and integrals of NMR peaks P2 and P3 respectively. These results were consequently compared against a conventional gravimetric approach. Correlations between methane adsorption capacities with clay minerals and organic contents were investigated respectively. The contributions to additional pore surface areas from clays and organic contents were discussed based on 2D images of the samples obtained from electron microscopy and energy dispersion spectroscopy (SEM EDS) as well as data acquired from nitrogen adsorption/desorption isotherms and total organic content measurements, respectively.

Chapter 6 provides a summary of the conclusions of the research work completed for this thesis as well as a consideration of potential future work based on observations and techniques developed in the current dissertation.

1.4 References

- AlGhamdi, T. M., Arns, C. H., & Eyvazzadeh, R. Y. (2013). Correlations between NMR-relaxation response and relative permeability from tomographic reservoir-rock images. *SPE Reservoir Evaluation and Engineering*, 16(4). <https://doi.org/10.2118/160870-pa>
- Aplin, A. C., & Macquaker, J. H. S. (2011). Mudstone diversity: Origin and implications for source, seal, and reservoir properties in petroleum systems. *AAPG Bulletin*, 95(12), 2031–2059. <https://doi.org/10.1306/03281110162>
- Belmabkhout, Y., Frère, M., & De Weireld, G. (2004). High-pressure adsorption measurements. A comparative study of the volumetric and gravimetric methods. *Measurement Science and Technology*, 15(5), 848–858. <https://doi.org/10.1088/0957-0233/15/5/010>
- Chen, L., Zuo, L., Jiang, Z., Jiang, S., Liu, K., Tan, J., & Zhang, L. (2019). Mechanisms of shale gas adsorption: Evidence from thermodynamics and kinetics study of methane

- adsorption on shale. *Chemical Engineering Journal*, 361, 559–570.
<https://doi.org/10.1016/j.cej.2018.11.185>
- Curtis, J. B. (2002). Fractured shale-gas systems. *AAPG Bulletin*, 86.
<https://doi.org/10.1306/61eaddbe-173e-11d7-8645000102c1865d>
- Dick, M. J., Muir, C., Veselinovic, D., & Green, D. (2017). Measuring Methane Adsorption in Shales Using NMR. *Society of Core Analysts*, 1–7.
- Hürlimann, M. D. (2012). Well Logging. *Encyclopedia of Magnetic Resonance*.
<https://doi.org/10.1002/9780470034590.emrstm0593.pub2>
- Kleinberg, R. L. (2001). NMR well logging at Schlumberger. *Concepts in Magnetic Resonance*, 13(6), 396–403. <https://doi.org/10.1002/cmr.1026>
- Liu, Y., & Wang, C. (2018). Determination of the Absolute Adsorption Isotherms of CH₄ on Shale with Low-Field Nuclear Magnetic Resonance. *Energy & Fuels*, 32(2), 1406–1415.
<https://pubs.acs.org/doi/10.1021/acs.energyfuels.7b03428>
- Loucks, R. G., Reed, R. M., Ruppel, S. C., & Jarvie, D. M. (2009). Morphology, genesis, and distribution of nanometer-scale pores in siliceous mudstones of the mississippian barnett shale. *Journal of Sedimentary Research*, 79(12), 848–861.
<https://doi.org/10.2110/jsr.2009.092>
- Mehana, M., & El-monier, I. (2016). Shale characteristics impact on Nuclear Magnetic Resonance (NMR) fluid typing methods and correlations. *Petroleum*, 2(2), 138–147.
<https://doi.org/10.1016/j.petlm.2016.02.002>
- Minh, C., Crary, S., Zielinski, L., Liu, C. B., Jones, S., & Jacobsen, S. (2012). 2D-NMR applications in unconventional reservoirs. *Society of Petroleum Engineers - SPE Canadian Unconventional Resources Conference 2012, CURC 2012*, 1, 87–103.
<https://doi.org/10.2118/161578-ms>
- Mitchell, J., Chandrasekera, T. C., Holland, D. J., Gladden, L. F., & Fordham, E. J. (2013). Magnetic resonance imaging in laboratory petrophysical core analysis. *Physics Reports*, 526(3), 165–225. <https://doi.org/10.1016/j.physrep.2013.01.003>
- Nikolaev, M. Y., & Kazak, A. V. (2019). Liquid saturation evaluation in organic-rich unconventional reservoirs: A comprehensive review. *Earth-Science Reviews*, 194, 327–349. <https://doi.org/10.1016/j.earscirev.2019.05.012>

- Odusina, E., Sondergeld, C., & Rai, C. (2011). An NMR study on shale wettability. *Society of Petroleum Engineers - Canadian Unconventional Resources Conference 2011, CURC 2011, 1*, 515–529. <https://doi.org/10.2118/147371-ms>
- Ougier-Simonin, A., Renard, F., Boehm, C., & Vidal-Gilbert, S. (2016). Microfracturing and microporosity in shales. *Earth-Science Reviews*, *162*, 198–226. <https://doi.org/10.1016/j.earscirev.2016.09.006>
- Rani, S., Prusty, B. K., & Pal, S. K. (2015). Methane adsorption and pore characterization of Indian shale samples. *Journal of Unconventional Oil and Gas Resources*, *11*, 1–10. <https://doi.org/10.1016/j.juogr.2015.03.003>
- Song, Y. Q., & Kausik, R. (2019). NMR application in unconventional shale reservoirs – A new porous media research frontier. *Progress in Nuclear Magnetic Resonance Spectroscopy*, *112–113*, 17–33. <https://doi.org/10.1016/J.PNMRS.2019.03.002>
- Sulucarnain, I., Sondergeld, C. H., & Rai, C. S. (2012). An NMR study of shale wettability and effective surface relaxivity. *Society of Petroleum Engineers - SPE Canadian Unconventional Resources Conference 2012, CURC 2012, 1*, 356–366. <https://doi.org/10.2118/162236-ms>
- Tinni, A., Odusina, E., Sulucarnain, I., Sondergeld, C., & Rai, C. S. (2015). Nuclear-magnetic-resonance response of brine, oil, and methane in organic-rich shales. *SPE Reservoir Evaluation and Engineering*, *18*(3), 400–406. <https://doi.org/10.2118/168971-PA>
- U.S. Energy Information Administration. (2021). *Annual Energy Outlook 2021 (AEO2021)*. https://www.eia.gov/outlooks/aeo/pdf/AEO_Narrative_2021.pdf
- Wang, M., Huang, K., Xie, W., & Dai, X. (2019). Current research into the use of supercritical CO₂ technology in shale gas exploitation. *International Journal of Mining Science and Technology*, *29*(5), 739–744. <https://doi.org/10.1016/j.ijmst.2018.05.017>
- Washburn, K. E. (2014). Relaxation mechanisms and shales. *Concepts in Magnetic Resonance Part A: Bridging Education and Research*, *43A*(3), 57–78. <https://doi.org/10.1002/cmr.a.21302>
- Wu, T., Zhao, H., Tesson, S., & Firoozabadi, A. (2019). Absolute adsorption of light hydrocarbons and carbon dioxide in shale rock and isolated kerogen. *Fuel*, *235*, 855–867. <https://doi.org/10.1016/J.FUEL.2018.08.023>

- Wu, Y., Fan, T., Jiang, S., Yang, X., Ding, H., Meng, M., & Wei, D. (2015). Methane adsorption capacities of the lower paleozoic marine shales in the Yangtze Platform, South China. *Energy and Fuels*, 29(7), 4160–4167. <https://doi.org/10.1021/acs.energyfuels.5b00286>
- Yao, Y., Liu, D., & Xie, S. (2014). Quantitative characterization of methane adsorption on coal using a low-field NMR relaxation method. *International Journal of Coal Geology*, 131, 32–40. <https://doi.org/10.1016/j.coal.2014.06.001>
- Yuan, Y., Rezaee, R., Verrall, M., Hu, S. Y., Zou, J., & Testmanti, N. (2018). Pore characterization and clay bound water assessment in shale with a combination of NMR and low-pressure nitrogen gas adsorption. *International Journal of Coal Geology*, 194, 11–21. <https://doi.org/10.1016/j.coal.2018.05.003>
- Zhao, G., & Wang, C. (2019). Influence of CO₂ on the adsorption of CH₄ on shale using low-field nuclear magnetic resonance technique. *Fuel*, 238, 51–58. <https://doi.org/10.1016/j.fuel.2018.10.092>

Chapter 2 Quantitative Tortuosity Measurements of Carbonate Rocks Using Pulsed Field Gradient NMR

Foreword – The contents of this chapter has been published in *Transport in Porous Media* in 2019. It has been reformatted with minor amendments to fit the style and structure of this thesis. This work mainly focused on the development and establishment of an NMR experimental protocol for measurements under high pressures. As part of the PhD research work, PFG NMR methods were applied to measure the tortuosity of four heterogeneous carbonate rock cores using methane as the probe fluid.

2.1 Abstract

Tortuosity is an important physical characteristic of porous materials; for example it is a critical parameter determining the effective diffusion coefficient dictating mixing between miscible fluids in porous rock structures as is relevant to enhanced gas recovery (EGR) processes. Accurate measurement of tortuosity remains challenging, resulting in various definitions dictated largely by the measurement protocol applied. Here we focus primarily on ‘diffusive’ tortuosity (τ_d), which is defined as the ratio of the bulk fluid diffusion coefficient to the restricted diffusion coefficient applicable to the porous media under study. Specifically we consider carbonate rock cores ranging in permeability from 2 to 5300 mD, and adapt pulsed field gradient (PFG) NMR methodology such that accurate measurements of tortuosity are obtained over a sufficiently representative length-scale of the porous media. To this end we deploy supercritical methane as a probe molecule exploiting both its high mobility and proton density. Tortuosity measurements are shown to be independent of both pressure and diffusion observation time, conclusively proving that our measurements are in the asymptotic regime in which all of the pore space is adequately sampled by the diffusing methane molecules. The resultant ‘diffusive’ tortuosity measurements (which ranged from 3.1-5.6) are then compared against independent electrical conductivity measurements of tortuosity using a two-electrode impedance technique applied to the carbonate samples saturated with brine solution. Agreement between the ‘diffusive tortuosity’, as measured by PFG NMR, and ‘electrical’

tortuosity was remarkably good (within 10%), given the very different measurements techniques used, for most of the carbonate rock samples considered.

2.2 Introduction

Mixing between miscible fluids, or effectively solutes, is a critical process in a very wide range of industrial and geological processes, ranging from chemical separation in adsorption and chromatography beds to contaminant transfer in the subsurface (e.g. Stalkup, 1983; Thomas, 2008). Generally dispersion, and associated dispersion coefficients, are required to model and simulate this mixing (e.g. Hughes et al., 2012; Perkins & Johnston, 1963). Particularly for geological scenarios (characterized by low Péclet numbers), the dispersion process is dominated by Fickian diffusion (Clennell, 1997), more specifically the effective diffusion coefficient as dictated by the restrictions imposed on molecular diffusion by the accommodating porous structure. The ratio of the bulk free diffusion coefficient to this effective diffusion coefficient is the ‘diffusive’ tortuosity; accurate measurements of this physical parameter for heterogeneous rocks, specifically carbonates, is the focus of the work presented here.

A relevant example of this mixing process, which is the specific motivation for the work conducted in this chapter, is enhanced gas recovery (EGR). In EGR, CO₂ is injected into natural gas reservoirs in order to maintain the reservoir pressure, improve sweep efficiency and safely sequester CO₂ within the formation (e.g. Honari et al., 2013; Hu et al., 2017; Hughes et al., 2012; Li et al., 2019; Oldenburg et al., 2001, 2004; Wang et al., 2012). However, excessive mixing of the injected CO₂ and the native natural gas (which are fully miscible in all proportions at typical reservoir conditions) could lead to very undesirable early breakthrough of the CO₂ at producing wells. To this end EGR reservoir simulations are required (e.g. Kim et al., 2017; Patel et al., 2016, 2017; Shi et al., 2017; Zhang et al., 2017), which in turn require tortuosity as an input parameter.

Various definitions of the tortuosity of a porous medium are in general use, these include geometrical, hydraulic, electrical and diffusive tortuosity (Clennell, 1997; Ghanbarian et al., 2013) - these are largely dictated by the experimental methodology used to measure them. Briefly, ‘geometrical’ tortuosity is defined as the mean path length through the pore space of a porous medium relative to the direct length (Adler, 1992). ‘Hydraulic’ tortuosity is determined via the relationship between permeability and porosity and is dependent on the critical path for

fluid flow (Carman, 1937; Clennell, 1997; Dullien, 1992) whilst ‘electrical’ tortuosity is determined by the formation factor of the rock sample and application of Archie’s law (Wyllie & Rose, 1950); electrical current flow in a rock saturated with brine is essentially a diffusive processes. Arguably ‘electrical’ and ‘diffusive’ tortuosity are both the most convenient to measure for a rock sample and the most robust. In the context of EGR, ‘diffusive’ tortuosity is the most relevant and hence is the focus here. Furthermore, comparison of, and potentially validation of the equivalence between, ‘diffusive’ tortuosity and ‘electrical’ tortuosity is largely absent in the literature to the best of our knowledge.

Carbonate reservoirs contain a substantial proportion of the world’s hydrocarbon resources - 60% of oil and 40% of gas reserves respectively (Schlumberger, 2019). Carbonates are generally more heterogeneous systems (Lucia, 2007; Ziauddin & Bize, 2007) than clastic (sandstone) rocks, the length scale of which renders accurate measurement of ‘diffusive’ tortuosity particularly difficult. Here we employ nuclear magnetic resonance (NMR) pulsed field gradient (PFG) techniques to measure the effective diffusion coefficient of supercritical methane in a range of carbonate core samples and hence determine the sample tortuosity. Typically such NMR diffusivity measurements in rocks are performed using brine solution as the probe fluid; however the greater heterogeneity of carbonates means that a longer diffusion length must be probed such that a sufficiently representative elementary volume (REV) of the carbonate is effectively considered. Water is unable to probe this length scale or REV in the available diffusive time scale, which is limited by its NMR T_1 relaxation rate. This limitation is addressed here via the use of supercritical methane which presents a diffusion coefficient approximately 100 times larger than that of liquid water. We proceed to compare these measurements of ‘diffusive’ tortuosity with conventional conductivity measurements of ‘electrical’ tortuosity, using the same carbonate samples.

2.3 Background

2.3.1 Dispersion and Tortuosity

A widely used equation to describe fluid dispersion in porous media is the one-dimensional advection-dispersion (AD) equation (Taylor, 1953; Taylor, 1954):

$$\frac{\partial c}{\partial t} = K_L \frac{\partial^2 c}{\partial x^2} - u_m \frac{\partial c}{\partial x}, \quad (2.1)$$

where C is the concentration of dispersing material, K_L is the longitudinal dispersion coefficient along the direction of bulk flow (x direction), u_m is the interstitial velocity in the bulk flow direction and t is time. At very low flow velocities, dispersion is dominated by diffusion and K_L is effectively equivalent to the apparent diffusion coefficient, D_{eff} . The ratio K_L/D , where D is the relevant molecular free diffusion coefficient, is consequently often expression as a function of the Péclet number, ($Pe_m = u_m \epsilon / D$) as follows (Perkins & Johnston, 1963):

$$\frac{K_L}{D} = \frac{1}{\tau} + \left(\frac{\epsilon u_m}{D}\right)^n, \quad (2.2)$$

where n is an empirical exponent, ϵ is a characteristic length-scale of the dispersive mixing process and τ is tortuosity. The relationship between K_L and τ at small velocities is schematically shown in **Figure 2.1**. The exponent n is commonly assumed to be 1 (Coats et al., 2009), although independent simulations and experimental measurements indicate a value of 1.2 for sandstones and 1.4 for carbonate rock cores (Bijeljic et al., 2011; Bijeljic & Blunt, 2006; Honari et al., 2015). τ , as appears in **Equation (2.2)**, corresponds to the ‘diffusive’ tortuosity as defined in the next section.

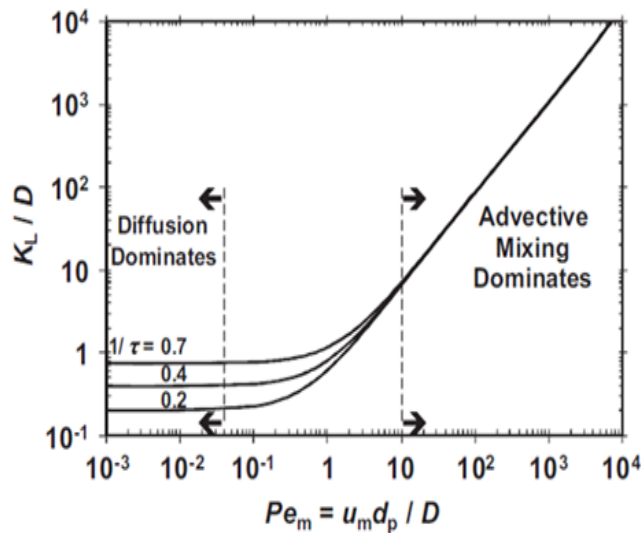


Figure 2.1. Schematic plot of normalized dispersion coefficient against Péclet number for a typical porous media with a grain size of d_p .

2.3.2 Tortuosity definitions

The concept of tortuosity was introduced by Carman (1937) to describe the sinuosity and interconnectedness of pore spaces and its influence on fluid transport processes in porous

media. Due to the geometrical complexity of the microstructure in most porous media however, various definitions of tortuosity are in use, largely dictated by the measurement method used. ‘Geometric’ tortuosity ($\tau_g \geq 1$) is simply described as the ratio of the length of a streamline (L) to the distance of a straight line (L_0) between two points in a porous media (Adler, 1992):

$$\tau_g = \frac{L}{L_0}, \quad (2.3)$$

In this case L_0 is taken as length of the sample; this has to be sufficiently long such that a representative elementary volume (REV) of the porous medium is sampled; τ_g will tend to a value of one as L_0 tends to zero. This concept of adequately sampling a REV is also relevant to the measurements of ‘diffusive’ tortuosity as discussed below. ‘Hydraulic’ Tortuosity (τ_h) is related to the system permeability via the semi-empirical Kozeny-Carman equation (Carman, 1956; Carman, 1937; Kozeny, 1927):

$$k = \frac{\phi^3}{\beta \tau_h (1-\phi)^2 \left(\frac{S}{V}\right)^2}, \quad (2.4)$$

where k is the permeability, ϕ is the porosity, S/V is the surface-to-volume ratio and β is a shape factor for the pore space.

‘Electrical’ Tortuosity (τ_e) is determined via measurement of the formation resistivity factor (F_R) which normalizes the resistivity of the porous medium (rock sample) saturated with brine solution to that of the brine solution. This can be related to the system porosity, ϕ , via Archie’s law (Archie, 1942):

$$F_R = \frac{R_o}{R_w} = \frac{\sigma_w}{\sigma_o} = \phi^{-m}, \quad (2.5)$$

where R and σ are resistivity and conductivity respectively and the subscript o and w refer to the rock fully saturated with the brine solution and the bulk brine solution respectively. m is the Archie cementation exponent indicating the degree of increment in resistivity when porosity decreases. The general value for m varies from 1, for fractured rocks, to 5 for significantly compacted rocks (Samson et al., 2018; Yildirim et al., 2011). τ_e can then then related to F_R as follows (Wyllie & Rose, 1950):

$$\tau_e = F_R \phi = \phi^{(1-m)}, \quad (2.6)$$

‘Diffusive’ tortuosity (τ_d) is the ratio of the free self-diffusion coefficient of bulk fluid, D , to the restricted effective self-diffusion coefficient of fluid in the porous media, D_{eff} (Satterfield & Sherwood, 1963):

$$\tau_d = \frac{D}{D_{eff}}, \quad (2.7)$$

One of the most mature and robust techniques to accurately measure these diffusion coefficients in porous media (and hence the ‘diffusive’ tortuosity) non-invasively is nuclear magnetic resonance pulsed field gradient (NMR PFG). This technique has been widely deployed to characterize the pore structures and pore size distributions of numerous types of porous media (e.g. Callaghan, 1991; Mantle et al., 2011; Sen, 2004). NMR PFG, as first demonstrated by Stejskal and Tanner (1965), relies on the application of two magnetic field gradients, each of absolute magnitude g (but in opposite direction) and duration δ , separated by a time interval Δ . Any diffusion of the NMR signal-bearing species during Δ will result in NMR signal, S , loss. The ratio S/S_0 is described by:

$$\frac{S}{S_0} = \exp\left(-D(\gamma g \delta)^2 \left(\Delta - \frac{\delta}{3}\right)\right), \quad (2.8)$$

where D is the self-diffusion coefficient of the relevant molecules and S_0 is the NMR signal in the absence of imposed magnetic field gradients. γ is the gyro-magnetic ratio of the nucleus being considered (in this study this is exclusively ^1H (for which $\gamma = 2.675 \times 10^8 \text{ rad s}^{-1} \text{ T}^{-1}$)). Typically S is measured as a function of g enabling determination of D . ‘Diffusive’ tortuosity is then easily calculated using **Equation (2.7)**; however as was effectively the case for ‘geometric tortuosity’ Δ has to be sufficiently long such that the diffusing molecules sample a REV of the sample under study. The practical upper bound on Δ is however limited by the T_1 value of the diffusing fluid to the order of 1-10s.

The time-dependent diffusion of fluid molecules in porous media is a strong function of the confining geometry with short- and long-time regimes clearly identifiable (as evident in **Figure 2.2**). For the short-time behavior, when the diffusion time, Δ , is only sufficient for molecules in the vicinity of pores walls to experience restricted diffusion, the following relationship is applicable (Latour et al., 1993; Mitra et al., 1992; Mitra et al., 1993):

$$\frac{D_{eff}}{D} \approx 1 - \frac{S}{V} \frac{4}{9\sqrt{\pi}} \sqrt{D\Delta}, \quad (2.9)$$

where S/V is the surface-to-volume ratio of the pore space restricting diffusion. As Δ increases eventually all diffusing molecules will diffuse through a sufficiently large volume of the pore space (equivalent to the REV discussed above) such that their effective level of restricted diffusion is consistent and invariant with increasing diffusion time – this is the long-term asymptotic regime equivalent to the inverse of ‘diffusive’ tortuosity.

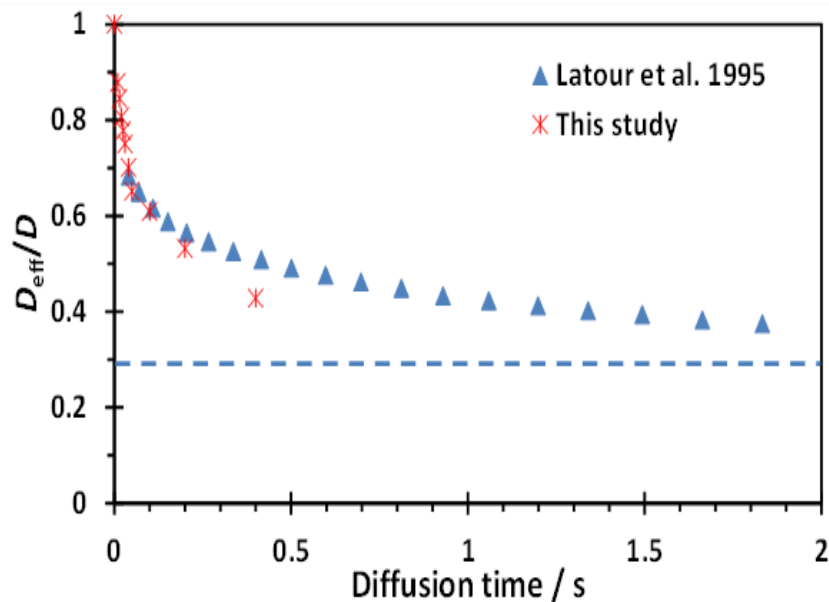


Figure 2.2. Diffusion coefficient of brine solution restricted in a Berea sandstone rock core. The blue dash line indicates the inverse tortuosity asymptote.

Due to the fact that diffusion coefficients of brine solution are orders of magnitude smaller than those of gas, when brine is used as the probe fluid, the time period over which diffusion is observed is not sufficiently long to reach this tortuosity asymptote. **Figure 2.2** shows the evolution in D_{eff}/D as a function of Δ for a Berea sandstone rock core saturated with a 2 wt% brine solution. The data of Latour et al. (1995) is shown alongside measurements performed as part of this study; agreement is excellent considering that completely different samples and different instrumentations were used. In both cases however, it is clear that as Δ increases, D_{eff}/D continues to decrease and does not reach an asymptotic long-time value which would equal $1/\tau_d$. This can only be determined via extrapolation of the measured data to longer values of Δ using a two point Padé approximation (Mitra et al., 1993) – the extrapolated value of $1/\tau_d$ is shown by the dashed blue line in **Figure 2.2**. Such a Padé approximation is often employed to estimate the tortuosity for sphere packs and sandstones (e.g. Davies et al., 2007; Frosch et al., 2000; Hürlimann et al., 1994; Latour et al., 1995; Vogt et al., 2002). Clearly

this extrapolation is a potential source of error that is avoided in the current work via the use of methane as the probe fluid. The much greater heterogeneity of carbonate rock cores and hence much larger REV means that the equivalent diffusion coefficient data acquired using brine solution is significantly further from the asymptote compared to sandstone and not of a sufficient precision to facilitate a robust extrapolation so as to determine $1/\tau_d$ reliably (Latour et al., 1995).

Oxygen (in a host fluid) diffusion in porous media has been investigated based on NMR T_2 measurements, and hence the effective diffusion coefficient determined (Shikhov & Arns, 2017). Considering the drawbacks of using brine solution as the probe fluid, an alternative is the use of hyperpolarised ^{129}Xe gas which offers the advantage of a much larger diffusion coefficient, chemical inertness and weak pore surface interaction (Mair et al., 1999; Wang et al., 2005) – this has been applied to determine the tortuosity of both sandstone and carbonate rock samples. Heteronuclear distortionless enhancement by polarization transfer (DEPT) techniques can also be used to enable a longer value of Δ and hence facilitate the measurement of ‘diffusive’ tortuosity (Akpa et al., 2007). In both cases, however specialist equipment and more complicated NMR PFG pulse sequences and sample preparations are required. Improvements to the two-point Padé approximation (Li et al., 2014; Pape et al., 2006) have also been realised via complementary numerical simulations of the diffusion process. Most recently, liquid ethane was used to probe the restricting geometry of sandstones when partially saturated with D_2O (Zecca et al., 2018). This provided an increase in the diffusion coefficient of the probe fluid by approximately an order of magnitude relative to brine solution. Here we employ supercritical methane and realise a further improvement of approximately another order of magnitude.

2.4 Experimental Details

Four carbonate rock cores (Estailades, Ketton, Portland and Indiana purchased from Kocurek Industries, USA) were investigated in this study. Standard Helium gas injection measurements at dry condition were used to determine their porosity and permeability. Further to this NMR T_2 measurements were applied to the rock cores saturated with a 2 wt% brine solution. The consequential rock sample petro-physical properties are summarized in **Table 2.1**. There is reasonably good agreement between the two independent methods of porosity determination – NMR porosity was determined by conventional CPMG measurement of the

water-saturated rock cores and system signal calibration using known volumes of water. The slightly higher NMR porosities than Helium porosities for the Portland and Indiana samples are potentially caused by residual water in substantial vuggy spaces on the rock core surface.

Table 2.1. Petro-physical properties of the carbonate rock cores.

| Sample ID | Length (mm) | Diameter (mm) | Permeability (mD) | Helium porosity (%) | NMR porosity (%) |
|------------|-------------|---------------|-------------------|---------------------|------------------|
| Estailades | 67.3 | 25.4 | 137 | 29.7 | 29.7 |
| Ketton | 67.8 | 25.4 | 5334 | 24.7 | 24.6 |
| Portland | 67.8 | 25.5 | 1.7 | 15.6 | 16.3 |
| Indiana | 66.7 | 25.2 | 54.5 | 15.7 | 16.6 |

Three-dimensional density variations were also determined for all four carbonate samples via X-ray CT images of the cores when dry. A Siemens SOMATOM AS was used with a beam of energy 140 KV and 500 mAs source intensity. The in-plane (cross-sectional) resolution was 100 μm ; 64 slices were acquired along the cores access at a resolution of 400 μm .

2.4.1 NMR diffusion measurements

A schematic of the experimental apparatus used in the NMR diffusion measurements is shown in **Figure 2.3**. Two syringe pumps (Teledyne ISCO 260D) were used for gas pressure maintenance in the rock core during all NMR PFG measurements. The rock core was contained in a PEEK TEMCO FCH NMR compatible rock core holder. Radial confining pressure and hence the rock core seal was maintained using a fluorocarbon (FluorinertTM FC-40 - hence providing no ¹H NMR signal) and a FEP heat shrink tubing and Viton sleeve at a pressure 50 bar above the operating pressure. This prevented any additional erroneous signal from methane outside of the rock core. A vacuum pump was used to initially remove air content of the rock core and associated piping, before flooding of the rock core with methane. An Oxford Instruments MARAN DRX 12.9 MHz (¹H) NMR Rock Core Analyzer coupled with a 53 mm inner diameter R.F. coil with the maximum magnetic field gradients to 0.33 T/m was used. A simple cylindrical PEEK cell (inner diameter of 15 mm and outside diameter of 25 mm) was

used instead of the rock core holder to measure the bulk self-diffusion coefficient of the probe methane fluid at the same temperature and range of pressures.

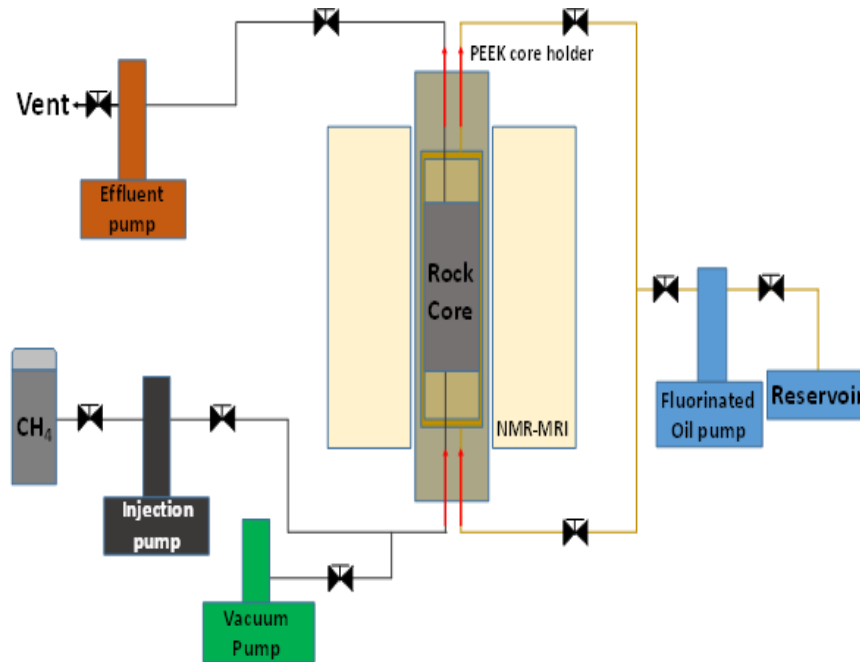


Figure 2.3. Schematic of the NMR tortuosity measurement apparatus. The red arrows indicate the direction of flow for methane and confining fluid respectively.

Methane (purchased from Coregas at a purity exceeded 99.995%) was used as the probe fluid as it presents a much larger free diffusion coefficient (approximately 100-fold) compared to brine solution as was used for the data presented in **Figure 2.2**. Consequently the asymptote limit, as shown in **Figure 2.2**, which determines tortuosity, is much more readily achieved as the methane molecules are able to sample a volume over an order of magnitude larger compared to brine solution at the same observation time, Δ . This approach is similar to our previous use of liquid ethane (Zecca et al., 2018) to measure the tortuosity of more homogeneous sandstones with variable residual water content. Prior to measurement, all rock cores in this work were stored in an oven at 120 °C for more than 7 days to remove as much residual water as possible.

The pressure of the methane during measurement is a compromise between ease of approaching the asymptotic limit defining tortuosity as a function of Δ (improves as pressure decreases and the methane self-diffusion coefficient increases) and signal-to-noise ratio (SNR) of acquired NMR signal (SNR increases as pressure increases resulting in more methane is available in the measurement volume to provide the NMR signal). Measurements of tortuosity were thus performed at pressures of 100, 75, 50 and 25 bar; bulk methane self-diffusion was

also measured at the same pressure values. Observation times (Δ) of 50, 100 and 200 ms were used for all measurements performed respectively.

In this study, in order to minimize the influence of internal magnetic field gradients in the rock cores which can distort signal attenuation, the “13-interval” alternating pulsed gradient stimulated echo (APGSTE) NMR pulse sequence was employed for all diffusion measurements in the rock cores (Cotts et al., 1989) – this is illustrated in **Figure 2.4**.

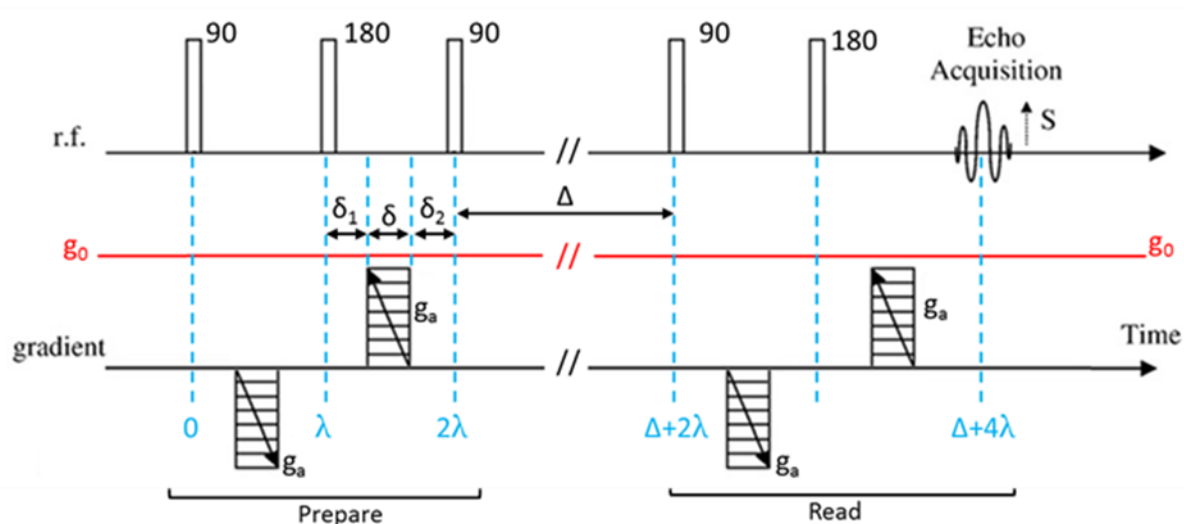


Figure 2.4. The “13-interval” APGSTE pulse sequence used for diffusion measurements in rock cores.

The signal attenuation (S/S_0) for the 13 interval APGSTE sequence is given by:

$$\frac{S}{S_0} = \exp \left\{ -D\gamma^2 \left[\delta^2 \left(4\Delta + 6\lambda - \frac{2\delta}{3} \right) g_a^2 + 2\lambda\delta(\delta_1 - \delta_2)g_a g_0 + \frac{4}{3}\lambda^3 g_0^2 \right] \right\}, \quad (2.10)$$

where δ is the duration of a single magnetic field gradient, δ_1 and δ_2 are the pre- and post- pulse time, respectively, λ is the time between the first two RF pulses, g_a is the applied magnetic field gradient and g_0 is the internal magnetic field gradient resulting from magnetic susceptibility difference inside the porous media (Stoller et al., 1991) and Δ is the observation time. By selecting the same value for the two time periods δ_1 and δ_2 and choosing observation time Δ much larger than λ , **Equation (2.10)** can be simplified to:

$$\frac{S}{S_0} = \exp \left[-D\gamma^2 \delta^2 \left(4\Delta + 6\lambda - \frac{2\delta}{3} \right) g_a^2 \right], \quad (2.11)$$

enabling D to be readily determined. **Table 2.2** is a summary of the NMR APGSTE parameters used.

Table 2.2. *NMR APGSTE experiment parameters.*

| | |
|---|---|
| Small delta, δ (ms) | 1.5 |
| Observation time, Δ (ms) | 100 (50, 200) |
| Time duration between RF pulses, λ (ms) | 2.995 |
| Number of scans, NS | 64 (100 bar), 128 (75 bar), 256 (50 and 25 bar) |
| Relaxation delay, (s) | 12 (restricted methane) 18 (bulk methane) |
| 90° pulse length (μ s) | 14.7 |
| 180° pulse length (μ s) | 29.4 |
| Maximum Gradient strength (G/cm) | 0.33 T/m |

2.4.2 Electrical Measurements

A two-electrode configuration (capacitor principle) was employed for the required measurements of electrical resistivity. The electrodes apply a voltage and measure the current flowing through the sample. Over-estimation of the impedance may occur due to the potentially high contact resistance at the sample-electrode interface and electrode polarization (ionic charge accumulation from the pore fluid at the electrodes) which occurs particularly at comparatively very low frequency (Johnson & Cole, 1951). Consequently a wet paper filter saturated with the same solution as that of the saturated plug was used to optimize the coupling between the sample surface and the electrode disks whilst measurements were performed at a frequency where no polarization effect was observed. The saturated rock core was horizontally mounted between two metal disk electrodes to avoid the influence of gravity; an end-to-end non-conductive clamp was employed to ensure that the sample-electrode coupling was in good contact to minimize contact resistance.

The electrodes were used in a potentiostatic condition where a voltage of 100 mV is applied and the resulting current measured. An Autolab electrochemical spectroscopy apparatus from Echochemie ltd. was used as an AC-impedance bridge (Bona et al., 2008) to perform electrical impedance spectroscopy in the low frequency range (< 1 MHz). The complex electrical impedance was recorded along 21 logarithmically distributed points between 10 Hz and 100 kHz. With the measured and known value of the current and voltage,

resistance among the rock core can be computed and consequently the electrical resistivity determined:

$$R = \frac{A}{L} Z \times T_c, \quad (2.12)$$

where R is the resistivity (ohm m), A is the cross-sectional area of the rock core, L is the length of the rock core mounted between the two electrodes, Z is the real component of the measured impedance and T_c is a correction factor to normalise experimental temperature to standard temperature.

A 2 wt% brine solution was prepared with sodium chloride as the solute. The electrical conductivity (inverse of resistivity) was measured with a portable Orion conductivity meter which was calibrated against standard solutions and temperature corrected to 25 °C. The carbonate rock cores were initially dried at a temperature of 120 °C for more than 7 days to ensure no or minimal water content. The rock cores were then individually placed in a high-resistance stainless steel chamber and vacuumed for more than 2 hours using an Agilent DS-102 vacuum pump. Following that, the rock core was fully saturated with the brine using a Jasco PU-980 HPLC pump, which started at a constant injection rate of 10 ml/min and then altered to a constant pressure mode to maintain the fully saturation condition at a constant pressure of 50 bar for more than 24 hours. Before each of the electrical resistivity measurement, any excess brine content on the rock core surface was removed. Using the measured resistivities and the Helium porosity data reported in **Table 2.1**, ‘electrical’ tortuosity was then calculated using **Equations (2.5)** and **(2.6)**.

2.5 Results and Discussion

2.5.1 X-ray CT Density Images

X-ray CT scans were used to investigate the meso-scale heterogeneity of the four carbonate samples considered. **Figure 2.5** presents bulk density images of the four carbonates (three transverse slices from the 3D image) – there is considerable variation in heterogeneity between them. Most striking is the Indiana sample which displays a significant number of larger pores and hence a ‘vuggy’ structure (Hidajat et al., 2004). In contrast the Ketton and Portland samples exhibit a higher degree of homogeneity than the other two samples at the length-scale dictated by the imaging resolution (400 µm in the axial direction, 100 µm in-plane).

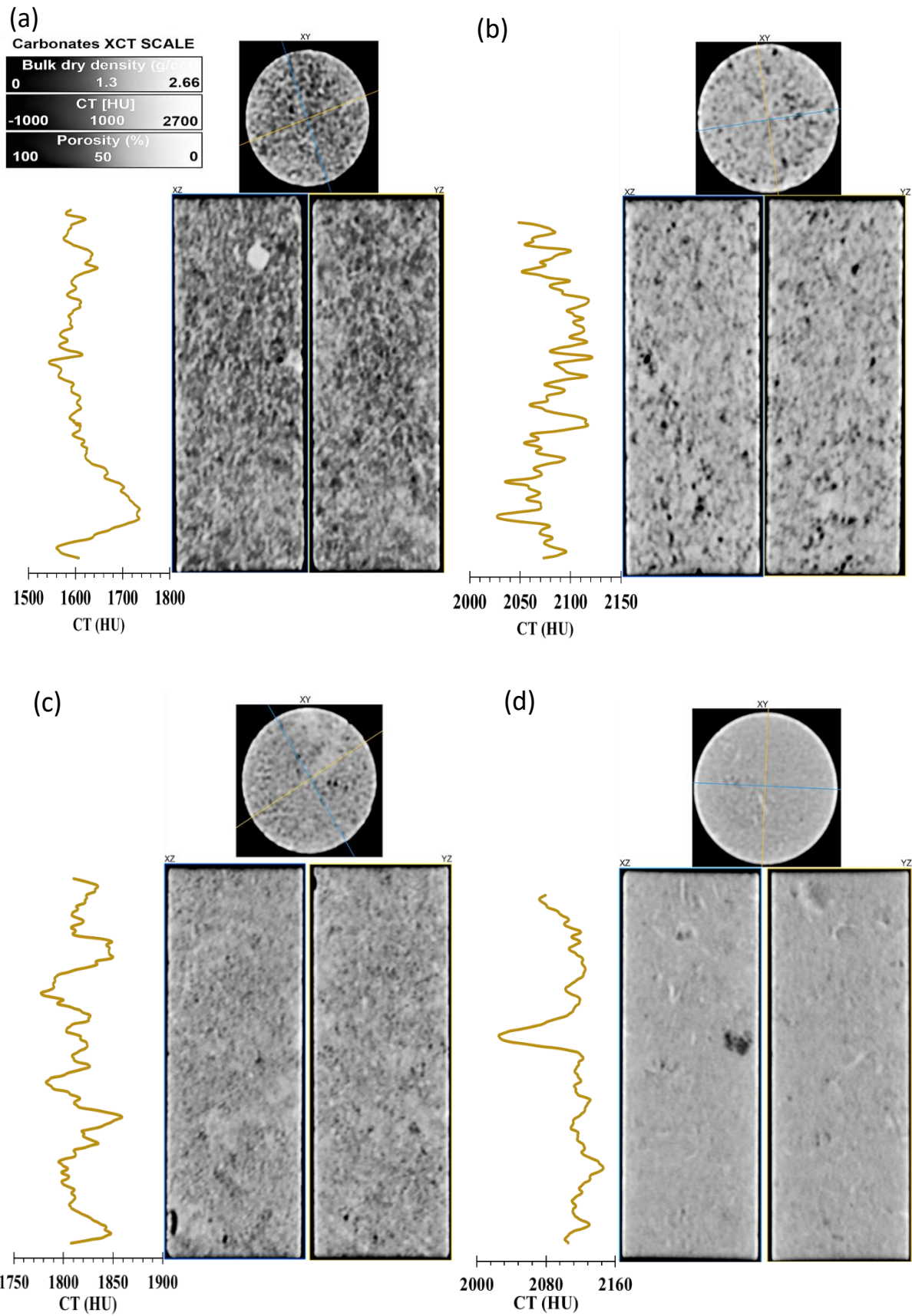


Figure 2.5. X-ray CT scan images of carbonate rock core (a) Estailades, (b) Indiana, (c) Ketton, (d) Portland. The yellow lines indicate the overall 3D bulk dry density profile.

2.5.2 Self-diffusion Coefficient Measurements

Table 2.3 reports the mean T_1 and T_2 values for the methane in bulk and in Ketton Carbonate as a function of pressure. The reduction in these parameters when restricted inside the rock core is expected and reflects the influence of surface relaxation. However mean T_1 is always significantly longer than Δ (100 ms – **Table 2.2**) and T_2 is always significantly longer than 4λ ($\lambda = 2.995$ ms (**Table 2.2**)) such that no significant relaxation editing is anticipated of the diffusion data acquired. **Figure 2.6** shows the NMR PFG signal attenuation data pertaining to bulk methane at 20 °C as a function of pressure, as acquired using the APGSTE pulse sequence shown in **Figure 2.4**. For these bulk methane diffusion measurements, the APGSTE sequence is not strictly required but was used to retain consistency with NMR PFG measurements performed in the rock cores. In all cases, the data is adequately fit using **Equation (2.11)** with the data acquired at 25 bar presenting the worst fit. This can be readily attributed to a combination of the following: (i) this sample presents the lowest gas (and hence ^1H) density meaning that these measurements suffered from the worst SNR. The critical pressure for methane at 20 °C is 45.99 bar (Setzmann & Wagner, 1991); thus whilst the measurement at 25 bar was performed with the methane in the gaseous state, all the higher pressure measurements were performed with methane in a supercritical state. (ii) The measurement at 25 bar is also more susceptible to gradient imperfections that are more evident when weaker gradients are employed (as are required for this faster diffusing system).

Table 2.3. Log-mean T_1 and T_2 relaxation times for Methane.

| | Pressure (bar) | 25 | 50 | 75 | 100 |
|---------------------|-------------------|------|------|------|------|
| Bulk methane | T_1 (s) | 0.66 | 1.17 | 1.76 | 2.33 |
| | T_2 (s) | 0.39 | 0.83 | 1.31 | 1.82 |
| Methane in | T_1 (s) | 0.37 | 0.65 | 0.85 | 1.22 |
| Ketton Carbonate | T_2 (s) | 0.10 | 0.13 | 0.16 | 0.17 |

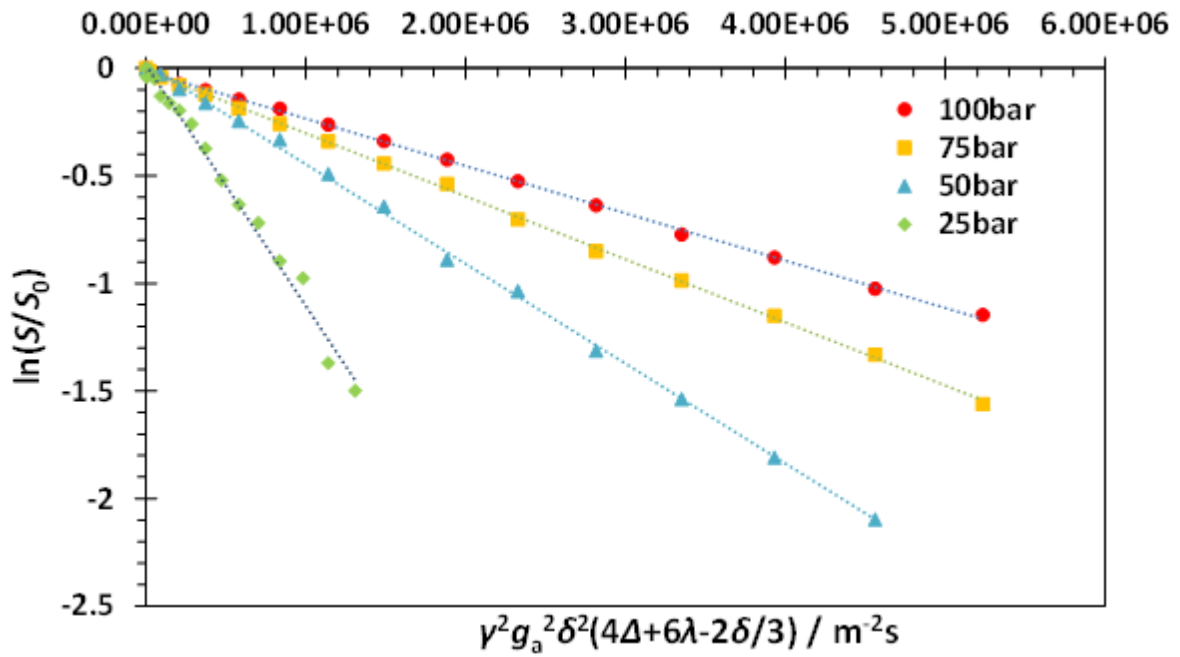


Figure 2.6. NMR signal attenuation of bulk methane at various experimental pressures. The dashed lines indicate the fit of **Equation (2.11)**.

The resultant free self-diffusion coefficient data for the bulk methane are presented in **Figure 2.7** as a function of pressure, along with experimental literature data from a number of sources (Dawson et al., 1970; Harris, 1978; Takahashi, 1972) as well as predictions using molecular dynamic simulations (Ho et al., 2016). There is good agreement between our data and the literature; the largest discrepancy occurs at 25 bar where it is possible that our measurements are up to 20% larger than those from literature. The data point at 25 bar is the most likely to be affected by convective flow induced by localized sample heating due to the application of magnetic field gradients, such an effect would erroneously increase the measured value of self-diffusion.

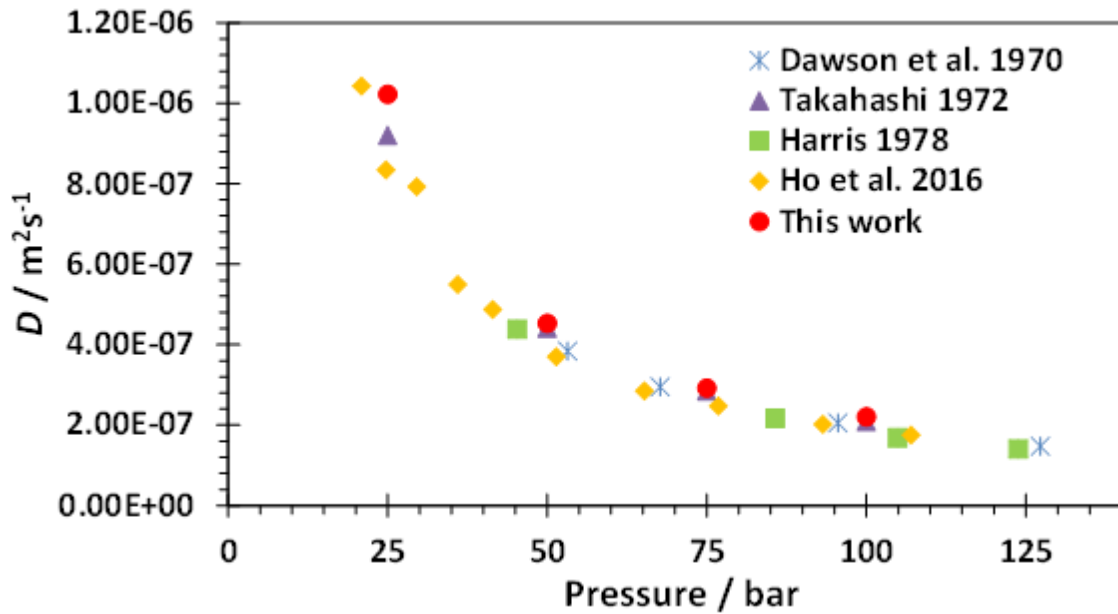


Figure 2.7. Methane free diffusion coefficient as a function of pressure, as acquired in this work and from literature data.

Example NMR PFG signal attenuation data are presented for methane in the Estailades carbonate core as a function of pressure in **Figure 2.8**. As expected, as pressure is increased, the signal attenuation is reduced resulting in a lower diffusion coefficient. We note the slight curvature in the data for all pressures. Thus, consistent with our previous work (Zecca et al., 2018) **Equation (2.11)** was applied to this data as g tends to zero in order to determine the apparent diffusion coefficient, D_{eff} (i.e. where **Equation (2.11)** is valid). The resultant values of D and D_{eff} for bulk methane and all carbonate samples are summarized in **Table 2.4** as a function of pressure. The resultant values of ‘diffusive’ tortuosity, as determined by application of **Equation (2.7)** is included in **Table 2.4**. Given the absence of clay materials from these carbonates, any effect from methane adsorption is negligible (Heller & Zoback, 2014). With respect to the data in **Table 2.4**, using Einstein’s diffusion formulae ($D = \langle r^2 \rangle / (6\Delta)$), the minimum mean free displacement is 2 mm which is significantly larger than the typical pore size of 10 μm (Alyafei & Blunt, 2016) for such carbonates.

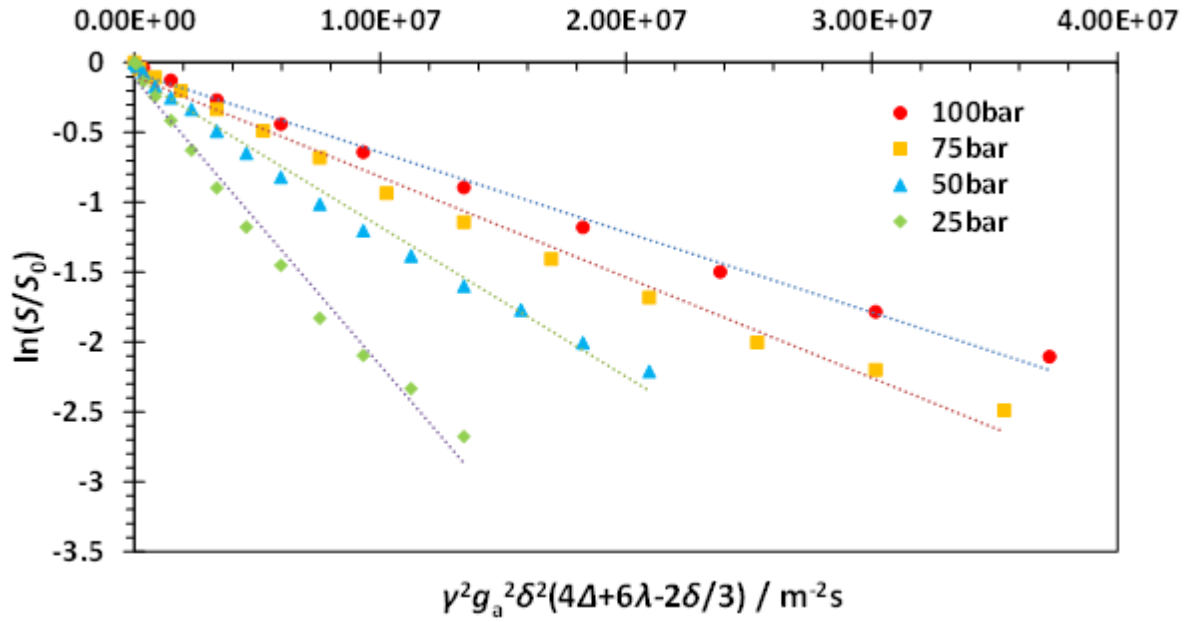


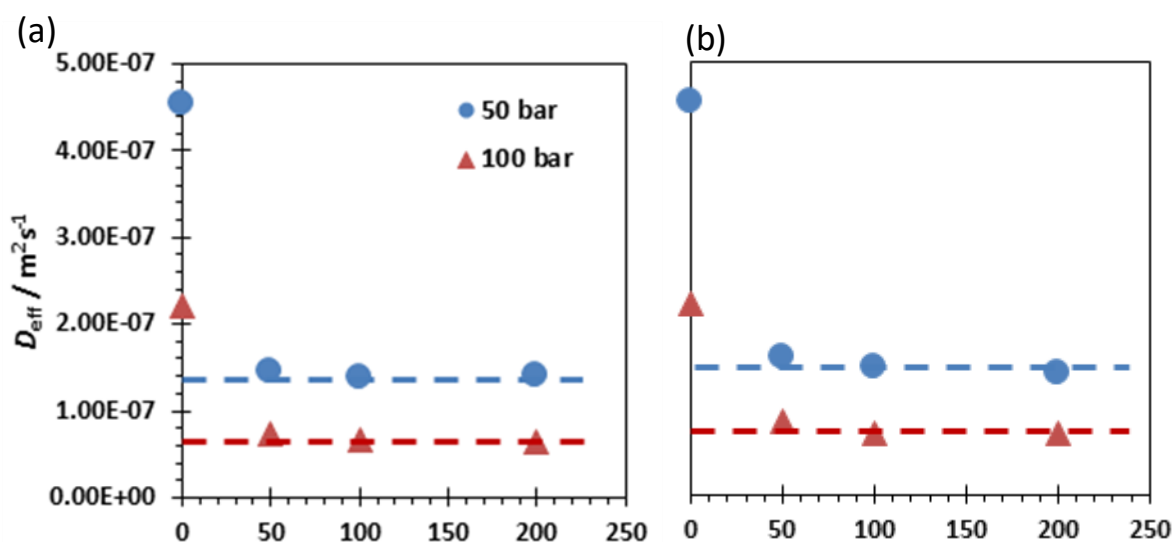
Figure 2.8. Sample NMR PFG signal attenuation data for restricted self-diffusion coefficient of methane at 20 °C in the Estailades carbonate sample as a function of pressure.

Table 2.4. Diffusion coefficient and ‘diffusive’ tortuosity for bulk methane and the four carbonate rock cores as a function of pressure

| Sample ID | Gas pressure (bar) | D_{eff} ($10^{-8} \text{ m}^2 \text{ s}^{-1}$) | NMR ‘Diffusive’ Tortuosity |
|--------------|--------------------|---|----------------------------|
| Bulk methane | 100 | 22.07 | - |
| | 75 | 29.23 | - |
| | 50 | 45.33 | - |
| | 25 | 102.30 | - |
| Estailades | 100 | 6.56 | 3.37 |
| | 75 | 8.78 | 3.33 |
| | 50 | 13.87 | 3.27 |
| | 25 | 26.64 | 3.84 |
| Ketton | 100 | 7.15 | 3.09 |
| | 75 | 9.35 | 3.12 |
| | 50 | 14.69 | 3.09 |
| | 25 | 28.39 | 3.60 |
| Portland | 100 | 3.96 | 5.58 |
| | 75 | 5.13 | 5.60 |
| | 50 | 8.06 | 5.62 |
| | 25 | 14.53 | 7.04 |
| Indiana | 100 | 5.56 | 3.97 |
| | 75 | 7.37 | 3.96 |
| | 50 | 11.28 | 4.02 |
| | 25 | 20.45 | 5.00 |

For all carbonate samples, the measured value of tortuosity is remarkably consistent for measurements performed above 25 bar. Using this data (>25 bar), the average tortuosity is 3.32 ± 0.02 for Estailades, 3.10 ± 0.04 for Ketton, 5.60 ± 0.02 for Portland and 3.98 ± 0.02 for Indiana carbonate, respectively. With respect to the measurements performed at 25 bar, the apparent error of approximately 20% in the bulk diffusion coefficient (discussed above with respect to **Figure 2.7**) is broadly consistent with the erroneous elevation in tortuosity observed. Nevertheless, when executed at pressures above 25 bar using supercritical methane, consistent data are produced. Based on this data it is suggested that 100 bar is the optimal pressure to employ given that it maximizes the NMR SNR (highest ^1H density).

As outlined above with respect to **Figure 2.2**, it is critical that the NMR measurements of ‘diffusive’ tortuosity be performed in the long-term asymptotic limit. Consequently, the measurements of ‘diffusive’ tortuosity were performed for all four carbonates as a function of observation time with Δ values of 50, 100 and 200 ms used respectively. The data corresponding to 50 and 100 bar are summarized in **Figure 2.9** for all four carbonate samples. The horizontal dashed lines are the inverse of the ‘diffusive’ tortuosity. In all cases it is clear that the data have adequately reached the asymptotic limit and hence that a Δ value of 100 ms is adequate for the measurement of tortuosity presented in this chapter.



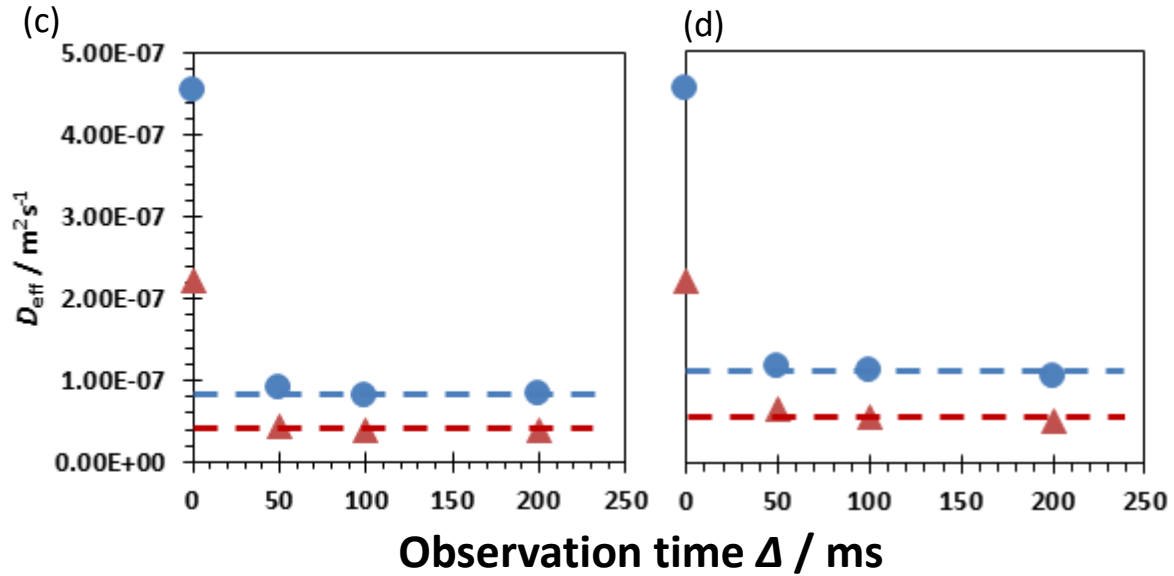


Figure 2.9. Restricted diffusion coefficient of methane as a function of observation time Δ at pressures of 50 and 100 bar for carbonate rock (a) Estailades, (b) Ketton, (c) Portland and (d) Indiana respectively. The dashed lines indicate the corresponding tortuosity asymptotes.

2.5.3 ‘Electrical’ Tortuosity

The measurements of ‘electrical’ resistivity and hence electrical tortuosity for the four carbonate samples are summarized in **Table 2.5**. This set of measurements was conducted using silver electrodes with an electrolyte of 2 wt% brine with the carbonate samples in a horizontal orientation; electrical tortuosity was determined using **Equation (2.6)**. The tortuosity measurements were found to be relatively insensitive to the actual brine concentration deployed.

Table 2.5. ‘Electrical’ resistivity and tortuosity.

| Sample ID | Resistivity (Ohm m) | Formation Factor | Electrical tortuosity |
|------------|------------------------|---------------------|--------------------------|
| Estailades | 4.09 | 13.46 | 4.00 |
| Ketton | 3.93 | 13.33 | 3.27 |
| Portland | 10.72 | 36.38 | 5.96 |
| Indiana | 13.07 | 44.33 | 7.36 |

Figure 2.10 shows the plot of ‘diffusive’ tortuosity as measured using NMR PFG correlated against ‘electrical’ tortuosity. Despite the completely different methods of measuring tortuosity, there is relatively good agreement for the case of the Ketton, Estailades and Portland carbonates; significantly better than presented in the literature to date for similar carbonate and sandstone rock cores (Latour et al. 1995 who employed brine solution as the probe fluid during NMR PFG measurements). This is not the case for the Indiana carbonate where the ‘electrical’ tortuosity is significantly larger than the ‘diffusive’ tortuosity. This effect was repeatable for a variety of Indiana samples with similar permeability. A plausible, possible explanation is that the ‘vuggy’ nature of the Indiana evident in **Figure 2.5** and visually evident in **Figure 2.11** (a photo of the Indiana carbonate sample) is the root cause. Complete flooding of these pores with the electrolyte solution was confirmed using NMR of the sample at various pressures; however it is possible that the uneven surface of the Indiana samples resulted in poor sample-electrode contact resulting in a larger erroneous value for ‘electrical’ tortuosity.

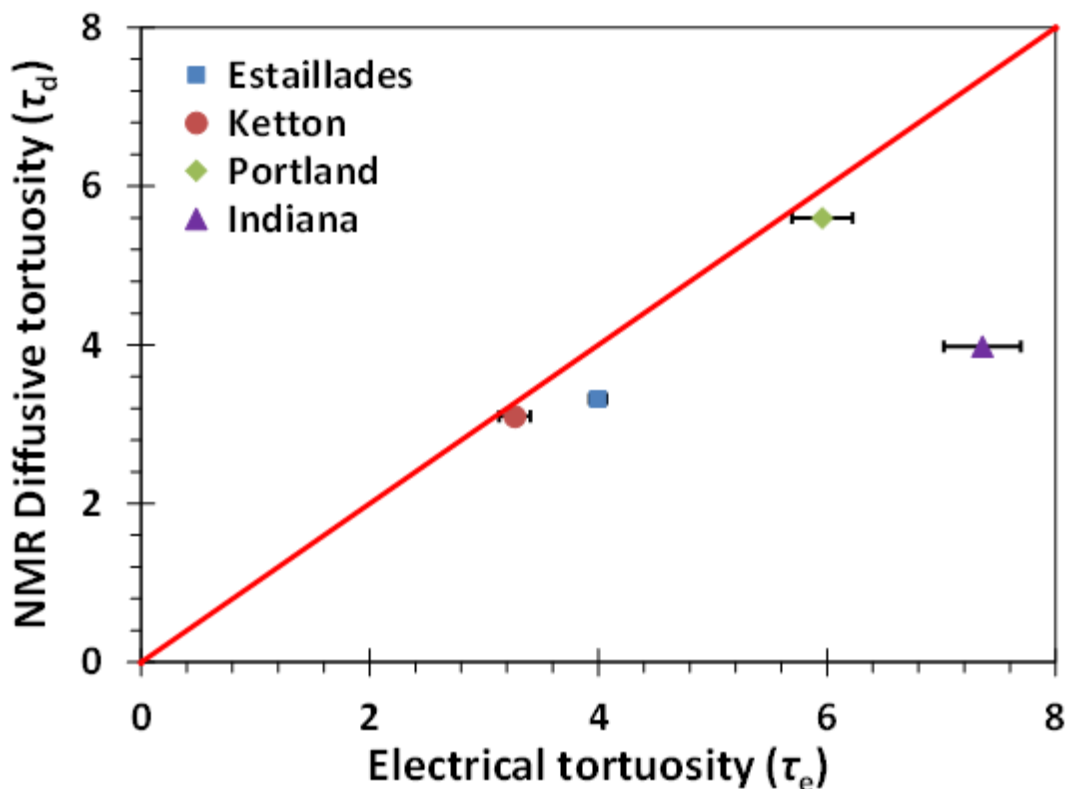


Figure 2.10. Comparison of ‘diffusive’ and ‘electrical’ tortuosity for all four carbonate samples. The solid line is the line of equivalence.



Figure 2.11. Photo of Indiana carbonate rock core; substantial pores can be observed on the core surface.

2.6 Conclusions

NMR PFG techniques were used to measure the ‘diffusive’ tortuosity of a range of carbonate samples. The use of supercritical methane provided a sufficiently large diffusion coefficient such that the required asymptotic limit of the diffusion process could be reached, allowing for accurate determination of ‘diffusive’ tortuosity. These measurements were remarkably consistent as a function of both methane pressure (above 25 bar) and observation time used, consistent with the asymptotic limit being achieved. Based on the measurements performed, the optimum pressure was 100 bar on account of the SNR attainable. For three of the samples (Ketton, Estailades and Portland carbonates) there was good agreement (within 10%) between ‘diffusive’ and ‘electrical’ tortuosity despite the very different tortuosity measurement methods used. In the case of Indiana carbonate, the measured ‘electrical’ tortuosity was significantly larger than the measured ‘diffusive’ tortuosity. This was hypothesized to be a consequence of the much larger pores present in this particular carbonate.

2.7 References

Adler, P. M. (1992). *Porous media: Geometry and Transports*. Butterworth-Heinemann Series

in Chemical Engineering. Butterworth-Heinemann, Boston.

- Akpa, B. S., Holland, D. J., Sederman, A. J., Johns, M. L., & Gladden, L. F. (2007). Enhanced ^{13}C PFG NMR for the study of hydrodynamic dispersion in porous media. *Journal of Magnetic Resonance*, 186(1), 160–165. <https://doi.org/10.1016/j.jmr.2007.02.001>
- Alyafei, N., & Blunt, M. J. (2016). The effect of wettability on capillary trapping in carbonates. *Advances in Water Resources*, 90, 36–50. <https://doi.org/10.1016/j.advwatres.2016.02.001>
- Archie, G. E. (1942). The Electrical Resistivity Log as an Aid in Determining Some Reservoir Characteristics. *Transactions of the AIME*, 146(01), 54–62. <https://doi.org/10.2118/942054-G>
- Bijeljic, B., & Blunt, M. J. (2006). Pore-scale modeling and continuous time random walk analysis of dispersion in porous media. *Water Resources Research*, 42(1). <https://doi.org/10.1029/2005WR004578>
- Bijeljic, B., Mostaghimi, P., & Blunt, M. J. (2011). Signature of non-fickian solute transport in complex heterogeneous porous media. *Physical Review Letters*, 107(20). <https://doi.org/10.1103/PhysRevLett.107.204502>
- Bona, N., Rossi, E., Capaccioli, S., & Lucchesi, M. (2008). Electrical Measurements : Considerations on the Performance of 2- and 4-Contact Systems. *Internation Symposium of the Society of Core Analysts*, 1998, 1–12.
- Callaghan, P. T. (1991). *Principles of Nuclear Magnetic Resonance Microscopy*. Clarendon Press, Oxford.
- Carman, P. C. (1937). Fluid flow through granular beds. *Chemical Engineering Research and Design*, 75(1 SUPPL.). [https://doi.org/10.1016/s0263-8762\(97\)80003-2](https://doi.org/10.1016/s0263-8762(97)80003-2)
- Carman, P. C. (1956). *Flow of Gases through Porous Media*. Butterworths Scientific Publications, London.
- Clennell, M. Ben. (1997). Tortuosity: a guide through the maze. *Geological Society Special Publication*, 122, 299–344. <https://doi.org/10.1144/GSL.SP.1997.122.01.18>
- Coats, K. H., Whitson, C. H., & Thomas, L. K. (2009). Modeling conformance as dispersion. *SPE Reservoir Evaluation and Engineering*, 12(1), 33–47. <https://doi.org/10.2118/90390->

pa

- Cotts, R. M., Hoch, M. J. R., Sun, T., & Markert, J. T. (1989). Pulsed field gradient stimulated echo methods for improved NMR diffusion measurements in heterogeneous systems. *Journal of Magnetic Resonance (1969)*, 83(2), 252–266. [https://doi.org/https://doi.org/10.1016/0022-2364\(89\)90189-3](https://doi.org/https://doi.org/10.1016/0022-2364(89)90189-3)
- Davies, C. J., Griffith, J. D., Sederman, A. J., Gladden, L. F., & Johns, M. L. (2007). Rapid surface-to-volume ratio and tortuosity measurement using Difftrain. *Journal of Magnetic Resonance*, 187(1), 170–175. <https://doi.org/10.1016/j.jmr.2007.04.006>
- Dawson, R., Khoury, F., & Kobayashi, R. (1970). Self-diffusion measurements in methane by pulsed nuclear magnetic resonance. *AICHE Journal*, 16(5), 725–729. <https://doi.org/10.1002/aic.690160507>
- Dullien, F. A. L. (1992). *Porous Media: Fluid Transport and Pore Structure (2nd ed.)*. Academic Press, San Diego.
- Frosch, G. P., Tillich, J. E., Haselmeier, R., Holz, M., & Althaus, E. (2000). Probing the pore space of geothermal reservoir sandstones by Nuclear Magnetic Resonance. *Geothermics*, 29(6), 671–687. [https://doi.org/10.1016/S0375-6505\(00\)00031-6](https://doi.org/10.1016/S0375-6505(00)00031-6)
- Ghanbarian, B., Hunt, A. G., Ewing, R. P., & Sahimi, M. (2013). Tortuosity in Porous Media: A Critical Review. *Soil Science Society of America Journal*, 77(5), 1461–1477. <https://doi.org/10.2136/sssaj2012.0435>
- Harris, K. R. (1978). The density dependence of the self-diffusion coefficient of methane at -50°, 25° and 50°C. *Physica A: Statistical Mechanics and Its Applications*, 94(3–4), 448–464. [https://doi.org/10.1016/0378-4371\(78\)90078-X](https://doi.org/10.1016/0378-4371(78)90078-X)
- Heller, R., & Zoback, M. (2014). Adsorption of methane and carbon dioxide on gas shale and pure mineral samples. *Journal of Unconventional Oil and Gas Resources*, 8(C), 14–24. <https://doi.org/10.1016/j.juogr.2014.06.001>
- Hidajat, I., Mohanty, K. K., Flaum, M., & Hirasaki, G. J. (2004). Study of vuggy carbonates using NMR and X-ray CT scanning. *SPE Reservoir Evaluation and Engineering*, 7(5), 365–377. <https://doi.org/10.2118/88995-PA>
- Ho, T. A., Criscenti, L. J., & Wang, Y. (2016). Nanostructural control of methane release in kerogen and its implications to wellbore production decline. *Scientific Reports*, 6.

<https://doi.org/10.1038/srep28053>

Honari, A., Bijeljic, B., Johns, M. L., & May, E. F. (2015). Enhanced gas recovery with CO₂ sequestration: The effect of medium heterogeneity on the dispersion of supercritical CO₂-CH₄. *International Journal of Greenhouse Gas Control*, 39, 39–50. <https://doi.org/10.1016/j.ijggc.2015.04.014>

Honari, A., Hughes, T. J., Fridjonsson, E. O., Johns, M. L., & May, E. F. (2013). Dispersion of supercritical CO₂ and CH₄ in consolidated porous media for enhanced gas recovery simulations. *International Journal of Greenhouse Gas Control*, 19, 234–242. <https://doi.org/10.1016/j.ijggc.2013.08.016>

Hu, Y., Li, M., Hou, G., Xu, S., Gong, K., Liu, X., Han, X., Pan, X., & Bao, X. (2017). The role of water in methane adsorption and diffusion within nanoporous silica investigated by hyperpolarized ¹²⁹Xe and ¹H PFG NMR spectroscopy. *Nano Research* 2018 11:1, 11(1), 360–369. <https://doi.org/10.1007/S12274-017-1638-8>

Hughes, T. J., Honari, A., Graham, B. F., Chauhan, A. S., Johns, M. L., & May, E. F. (2012). CO₂ sequestration for enhanced gas recovery: New measurements of supercritical CO₂-CH₄ dispersion in porous media and a review of recent research. *International Journal of Greenhouse Gas Control*, 9, 457–468. <https://doi.org/10.1016/j.ijggc.2012.05.011>

Hürlimann, M. D., Latour, L. L., & Sotak, C. H. (1994). Diffusion measurement in sandstone core: NMR determination of surface-to-volume ratio and surface relaxivity. *Magnetic Resonance Imaging*, 12(2), 325–327. [https://doi.org/10.1016/0730-725X\(94\)91548-2](https://doi.org/10.1016/0730-725X(94)91548-2)

Johnson, J. F., & Cole, R. H. (1951). Dielectric Polarization of Liquid and Solid Formic Acid. *Journal of the American Chemical Society*, 73(10), 4536–4540. <https://doi.org/10.1021/ja01154a012>

Kim, T. H., Cho, J., & Lee, K. S. (2017). Evaluation of CO₂ injection in shale gas reservoirs with multi-component transport and geomechanical effects. *Applied Energy*, 190, 1195–1206. <https://doi.org/10.1016/j.apenergy.2017.01.047>

Kozeny, J. (1927). Ueber kapillare Leitung des Wassers im Boden Sitzungsber Akad. *Sitzungsber Akad. Wiss.*, 136(2a), 271–306.

Latour, L. L., Kleinberg, R. L., Mitra, P. P., & Sotak, C. H. (1995). Pore-Size Distributions and Tortuosity in Heterogeneous Porous Media. *Journal of Magnetic Resonance, Series A*,

112(1), 83–91. <https://doi.org/10.1006/jmra.1995.1012>

- Latour, Lawrence L., Mitra, P. P., Kleinberg, R. L., & Sotak, C. H. (1993). Time-Dependent Diffusion Coefficient of Fluids in Porous Media as a Probe of Surface-to-Volume Ratio. *Journal of Magnetic Resonance - Series A*, 101(3), 342–346. <https://doi.org/10.1006/jmra.1993.1056>
- Li, L., Shikhov, I., Zheng, Y., & Arns, C. H. (2014). Experiment and Simulation on NMR and electrical measurements on Liege chalk. *Diffus. Fundam*, 22.
- Li, M., Vogt, S. J., May, E. F., & Johns, M. L. (2019). In Situ CH₄–CO₂ Dispersion Measurements in Rock Cores. *Transport in Porous Media*, 129(1), 75–92. <https://doi.org/10.1007/s11242-019-01278-y>
- Lucia, F. J. (2007). *Carbonate Reservoir Characterization*. Springer, Berlin.
- Mair, R. W., Wong, G. P., Hoffmann, D., Hürlimann, M. D., Patz, S., Schwartz, L. M., & Walsworth, R. L. (1999). Probing porous media with gas diffusion nmr. *Physical Review Letters*, 83(16), 3324–3327. <https://doi.org/10.1103/PhysRevLett.83.3324>
- Mantle, M. D., Enache, D. I., Nowicka, E., Davies, S. P., Edwards, J. K., Dagostino, C., Mascarenhas, D. P., Durham, L., Sankar, M., Knight, D. W., Gladden, L. F., Taylor, S. H., & Hutchings, G. J. (2011). Pulsed-field gradient NMR spectroscopic studies of alcohols in supported gold catalysts. *Journal of Physical Chemistry C*, 115(4), 1073–1079. <https://doi.org/10.1021/jp105946q>
- Mitra, P. P., Sen, P. N., & Schwartz, L. M. (1993). Short-time behavior of the diffusion coefficient as a geometrical probe of porous media. *Physical Review B*, 47(14), 8565–8574. <https://doi.org/10.1103/PhysRevB.47.8565>
- Mitra, P. P., Sen, P. N., Schwartz, L. M., & Le Doussal, P. (1992). Diffusion propagator as a probe of the structure of porous media. *Physical Review Letters*, 68(24), 3555–3558. <https://doi.org/10.1103/PhysRevLett.68.3555>
- Oldenburg, C. M., Pruess, K., & Benson, S. M. (2001). Process modeling of CO₂ injection into natural gas reservoirs for carbon sequestration and enhanced gas recovery. *Energy and Fuels*, 15(2), 293–298. <https://doi.org/10.1021/ef000247h>
- Oldenburg, C. M., Stevens, S. H., & Benson, S. M. (2004). Economic feasibility of carbon sequestration with enhanced gas recovery (CSEGR). *Energy*, 29(9–10), 1413–1422.

<https://doi.org/10.1016/j.energy.2004.03.075>

Pape, H., Tillich, J. E., & Holz, M. (2006). Pore geometry of sandstone derived from pulsed field gradient NMR. *Journal of Applied Geophysics*, 58(3), 232–252.
<https://doi.org/10.1016/j.jappgeo.2005.07.002>

Patel, M. J., May, E. F., & Johns, M. L. (2016). High-fidelity reservoir simulations of enhanced gas recovery with supercritical CO₂. *Energy*, 111, 548–559.
<https://doi.org/10.1016/j.energy.2016.04.120>

Patel, M. J., May, E. F., & Johns, M. L. (2017). Inclusion of connate water in enhanced gas recovery reservoir simulations. *Energy*, 141, 757–769.
<https://doi.org/10.1016/j.energy.2017.09.074>

Perkins, T. K., & Johnston, O. C. (1963). A Review of Diffusion and Dispersion in Porous Media. *Society of Petroleum Engineers Journal*, 3(01), 70–84.
<https://doi.org/10.2118/480-pa>

Samson, G., Deby, F., Garciaz, J. L., & Perrin, J. L. (2018). A new methodology for concrete resistivity assessment using the instantaneous polarization response of its metal reinforcement framework. *Construction and Building Materials*, 187, 531–544.
<https://doi.org/10.1016/j.conbuildmat.2018.07.158>

Satterfield, C.N., Sherwood, T. K. (1963). *The Role of Diffusion in Catalysis*. Addison-Wesley, Boston.

Schlumberger. *Carbonate Reservoirs*. Retrieved July 31, 2019, from https://www.slb.com/services/technical_challenges/carbonates.aspx

Sen, P. N. (2004). Time-dependent diffusion coefficient as a probe of geometry. *Concepts in Magnetic Resonance Part A: Bridging Education and Research*, 23(1), 1–21.
<https://doi.org/10.1002/cmr.a.20017>

Setzmann, U., & Wagner, W. (1991). A New Equation of State and Tables of Thermodynamic Properties for Methane Covering the Range from the Melting Line to 625 K at Pressures up to 100 MPa. *Journal of Physical and Chemical Reference Data*, 20(6), 1061–1155.
<https://doi.org/10.1063/1.555898>

Shi, Y., Jia, Y., Pan, W., Huang, L., Yan, J., & Zheng, R. (2017). Potential evaluation on CO₂-EGR in tight and low-permeability reservoirs. *Natural Gas Industry B*, 4(4), 311–318.

<https://doi.org/10.1016/j.ngib.2017.08.013>

- Shikhov, I., & Arns, C. H. (2017). Tortuosity estimate through paramagnetic gasdiffusion in rock saturated with two fluids using T2(z, t) low-field NMR. *Diffusion Fundamentals*, 29(5), 1–7.
- Stalkup, F. I. (1983). Status of Miscible Displacement. *JPT, Journal of Petroleum Technology*, 35(4), 815–826. <https://doi.org/10.2118/9992-PA>
- Stejskal, E. O., & Tanner, J. E. (1965). Spin diffusion measurements: Spin echoes in the presence of a time-dependent field gradient. *The Journal of Chemical Physics*, 42(1), 288–292. <https://doi.org/10.1063/1.1695690>
- Stoller, S. D., Happer, W., & Dyson, F. J. (1991). Transverse spin relaxation in inhomogeneous magnetic fields. *Physical Review A*, 44(11), 7459–7477. <https://doi.org/10.1103/PhysRevA.44.7459>
- Takahashi, S. (1972). The Diffusion of Gases at High Pressures. IV. The Diffusion of CTH 3 in the CH₄-CO₂ System. *Bulletin of the Chemical Society of Japan*, 45(7), 2074–2078. <https://doi.org/10.1246/bcsj.45.2074>
- Taylor, G. (1953). Dispersion of soluble matter in solvent flowing slowly through a tube. *Proceedings of the Royal Society of London. Series A. Mathematical and Physical Sciences*, 219(1137), 186–203. <https://doi.org/10.1098/rspa.1953.0139>
- Taylor, G. (1954). Conditions under which dispersion of a solute in a stream of solvent can be used to measure molecular diffusion. *Proceedings of the Royal Society of London. Series A. Mathematical and Physical Sciences*, 225(1163), 473–477. <https://doi.org/10.1098/rspa.1954.0216>
- Thomas, S. (2008). Enhanced oil recovery - An overview. *Oil and Gas Science and Technology*, 63(1 SPEC. ISS.), 9–19. <https://doi.org/10.2516/ogst:2007060>
- Vogt, C., Galvosas, P., Klitzsch, N., & Stallmach, F. (2002). Self-diffusion studies of pore fluids in unconsolidated sediments by PFG NMR. *Journal of Applied Geophysics*, 50(4), 455–467. [https://doi.org/10.1016/S0926-9851\(02\)00195-7](https://doi.org/10.1016/S0926-9851(02)00195-7)
- Wang, H., Li, G., & Shen, Z. (2012). A feasibility analysis on shale gas exploitation with supercritical carbon dioxide. *Energy Sources, Part A: Recovery, Utilization and Environmental Effects*, 34(15), 1426–1435.

<https://doi.org/10.1080/15567036.2010.529570>

- Wang, R., Pavlin, T., Rosen, M. S., Mair, R. W., Cory, D. G., & Walsworth, R. L. (2005). Xenon NMR measurements of permeability and tortuosity in reservoir rocks. *Magnetic Resonance Imaging*, 23(2 SPEC. ISS.), 329–331. <https://doi.org/10.1016/j.mri.2004.11.044>
- Wyllie, M. R. J., & Rose, W. D. (1950). Some Theoretical Considerations Related To The Quantitative Evaluation Of The Physical Characteristics Of Reservoir Rock From Electrical Log Data. *Journal of Petroleum Technology*, 2(04), 105–118. <https://doi.org/10.2118/950105-g>
- Yildirim, H., Ilica, T., & Sengul, O. (2011). Effect of cement type on the resistance of concrete against chloride penetration. *Construction and Building Materials*, 25(3), 1282–1288. <https://doi.org/10.1016/j.conbuildmat.2010.09.023>
- Zecca, M., Vogt, S. J., Connolly, P. R. J., May, E. F., & Johns, M. L. (2018). NMR Measurements of Tortuosity in Partially Saturated Porous Media. *Transport in Porous Media*, 125(2), 271–288. <https://doi.org/10.1007/s11242-018-1118-y>
- Zhang, L., Li, X., Zhang, Y., Cui, G., Tan, C., & Ren, S. (2017). CO₂ injection for geothermal development associated with EGR and geological storage in depleted high-temperature gas reservoirs. *Energy*, 123, 139–148. <https://doi.org/10.1016/j.energy.2017.01.135>
- Ziauddin, M. E., & Bize, E. (2007). *The Effect of Pore Scale Heterogeneities on Carbonate Stimulation Treatments*. <https://doi.org/10.2118/104627-ms>

Chapter 3 Shale Rock Core Analysis using NMR: Effect of bitumen and water content

Foreword – The contents of this chapter has been published in *Journal of Petroleum Science and Engineering* in 2020. It has been reformatted with minor amendments to fit the style and structure of this thesis. This work presents the characterization of a range of shale cores in terms of bitumen and water content using a combination of NMR FID and CPMG measurements with the required data interpretation using a spliced Gaussian and exponential inversion method.

3.1 Abstract

Hydrocarbon production from unconventional shale reservoirs has gained increasing worldwide focus, spurred largely by improvements in production techniques. Nuclear magnetic resonance (NMR) is increasingly being explored as a means of characterizing such shale rock. Compared to conventional sandstone and carbonate rocks, shales present a much lower porosity and permeability with NMR signal arising from both producible hydrocarbon fluid content as well as semi-solid organic solids and bitumen. Interpretation of the resultant NMR signal from shales is consequently comparatively more complex. To this end we apply combined NMR free induction decay (FID) and Carr-Purcell-Meilboom-Gill (CPMG) measurements and interpret the spliced data using a combined Gaussian and exponential inversion method. This was applied to a range of shale samples with variable moisture content in an attempt to assess the accuracy of such an approach to delineate the inherent predominantly bitumen signal from that of the added water. The analysis was performed at a range of ^1H NMR frequencies (20, 40 and 60 MHz), which are applicable to more widely accessible bench-top NMR spectrometers. Consistently, the Gaussian component of the resultant $T_2^*|T_2$ distribution was found to be independent of moisture content, scaling rather with the total organic content of the respective shale cores. In contrast, the exponential component of the resultant $T_2^*|T_2$ distribution was found to scale linearly with the moisture content of the cores.

3.2 Introduction

Unconventional reservoirs, predominantly gas and tight oil shales, have gained increasing importance for the world's energy supplies due primarily to reducing production costs and their potentially much greater hydrocarbon reserves relative to conventional reservoirs (Jia, 2017; Ratner & Tiemann, 2014). Natural gas production from tight rocks/shale gas now contributes in excess of 60% of total US natural gas production and is expected to increase by ~25 trillion cubic feet over the next 30 years to constitute over 90% of total US natural gas production in 2050 (U.S. Energy Information Administration, 2019). Accurate characterization of shales is, however, critical to enable more predictive estimates of both reserves and productivity (Nikolaev & Kazak, 2019; Song & Kausik, 2019; Wang et al., 2012). Unlike conventional hydrocarbon reservoirs, shales feature both comparatively low porosity and permeability, a significant solid organic content and complex nanostructures. Consequently, shale characterization is particularly challenging.

Nuclear magnetic resonance (NMR) has become a powerful technique to characterize the petro-physical properties of rock due mainly to non-invasive detection and lithology-independent porosity estimation (e.g. Coates, G., Xiao, L., Prammer, 1999; Kleinberg, 2001; Logan et al., 1998). Such NMR applications include estimation of pore size distributions (e.g. Arns, 2004; Davies et al., 1990; Davies & Packer, 1990; Mitchell et al., 2013), identification of pore fluids (e.g. Hürlimann, 2012; Yuan et al., 2018; Zhao et al., 2011), determination of wettability (e.g. Odusina et al., 2011; Sulucarnain et al., 2012; Yan et al., 2019) and estimation of permeability (e.g. AlGhamdi et al., 2013). For conventional hydrocarbon rocks such as sandstone with negligible detectable hydrogen in the 'solid' matrix, the ^1H NMR signal originates from pore space fluids, enabling rock porosity to be accurately determined. However, shales are generally very heterogeneous with both significant organic content and nano-scale to micro-scale pores in both the organic and inorganic phases (e.g. Chalmers et al., 2012; Josh et al., 2012; Minh et al., 2012). This organic content is composed of both kerogen and bitumen (which are broadly defined as being insoluble and soluble in organic solvents respectively). Whilst the ^1H NMR characteristics of this organic content corresponds to comparatively very short NMR relaxation times due to their very high viscosity (Loucks et al., 2009); bitumen (which generally features a comparatively lower molecular weight) in particular will provide a ^1H NMR signal intensity which is often comparable to that of any hydrocarbon content present in the pore space (Mehana & El-monier, 2016; Tinni et al., 2015; Washburn et al., 2015).

Separation of this bitumen signal is required in order to more accurately quantify system porosity and recoverable organic content.

The wide application of laboratory-based NMR to conventional rocks has mainly focused on ^1H frequencies of 2 MHz (Coates et al., 1999; Hürlimann, 2012), motivated mainly by calibration needs of NMR well logging tools (e.g. Odusina & Sigal, 2011; Rylander et al., 2013; Testamanti & Rezaee, 2017; Washburn & Birdwell, 2013) as well as the detrimental contributions of internal magnetic field gradients due to magnetic susceptibility contrast (Connolly et al., 2019; Mitchell et al., 2010). The more limited application of laboratory-based NMR for the characterization of shale rock samples has been arguably less restricted in terms of ^1H frequency used. This is primarily due to the order of magnitude smaller pores in shales compared to conventional reservoir rocks resulting in a transition from a short-time relaxation to a motional averaging relaxation regime where the impacts of internal gradients are less consequential (Mitchell et al., 2013; Washburn, 2014) to the observed NMR signals. In the motional averaged regime, the internal gradient field is averaged by a spin (NMR signal bearing species) restricted translational diffusion between echoes resulting in relaxation behavior, which is largely independent of echo time. The nano-pore characteristics of shale however, also mean that diffusive coupling, where spins diffuse between multiple pores over the course of relaxation measurement, results in relaxation characteristics that reflect an average of several pores (Washburn, 2014). Comparatively wide use has been made of two-dimensional NMR T_1 - T_2 maps for the less ambiguous characterization of shale fluid/soft solid composition (e.g. Fleury & Romero-Sarmiento, 2016; Kausik et al., 2014; Seymour et al., 2013; Song & Kausik, 2019; Yang & Kausik, 2016). In such 2D measurements, signal-to-noise ratio (SNR) becomes much more critical, particularly for low porosity systems such as shales. Comparison of T_1 - T_2 maps for shales at a range of frequencies have revealed overall better performance at higher ^1H frequencies (e.g. Kausik et al., 2017; Song & Kausik, 2019) which feature shorter equipment dead-times and hence which are sensitive to shorter T_2 times. Anger et al. (2016) conducted NMR T_2 measurements on shale from a ^1H Larmor frequency of 2 MHz up to 23 MHz and Min et al. (2019) investigated the results from NMR T_2 measurements on shales for ^1H frequencies between 2 and 12 MHz. Both reported consistent T_2 relaxation times between the two field strengths and that there was no apparent loss of signal due to internal gradient effects whilst SNR was greatly improved at the higher fields. Xie and Gan (2018) also recommended that a 20 MHz ^1H frequency is optimum for shale studies associated with NMR techniques.

Early work by Straley (1997) demonstrated the ability of NMR to quantify both methane and residual water in conventional reservoir rocks cores and how such partially saturated measurements can be related to producible fluid volumes. The impact of water content is similarly relevant to hydrocarbon recovery from unconventional shale reservoirs. In addition to the nascent water content in shales, only 30% of water injected during hydraulic stimulation of such systems is typically recovered (Tokunaga et al., 2017). Methane adsorption is also impacted by the presence of capillary bound water and thin water films casting doubt on the ability of dry state laboratory measurements of adsorption to properly reflect real in *situ* conditions. Furthermore, the distribution of water in partially saturated systems is a fundamental factor in the relative permeability of reservoir fluids (Chenevert, 1970; Sang et al., 2019). Hence, knowledge of the distribution of water as a function of pore occupation in partially saturated systems is critical to both predicting gas adsorption behaviour in shale and improving the understanding of relative permeability in shales. This study thus focuses on the quantification of both organic matter, mainly bitumen, and moisture content of shales. This is pursued using a novel combination of NMR free induction decay (FID) and Carr-Purcell-Meilboom-Gill (CPMG) measurements; these are individually standard techniques that are both widely available and practiced. These measurements are applied to a range of field shale samples in which moisture content is systematically varied using a range of relative humidity environments. The FID and CPMG data are spliced together and analyzed using a combined Gaussian and exponential inversion method (Washburn et al., 2015) to generate distributions of T_2^*/T_2 – these were then compared to the organic and moisture contents of the respective samples. Measurements were also performed at a range of ^1H resonance frequencies, enabling a comparison of the effect of NMR detection frequency on the ability to differentiate the bitumen signal from that of the moisture content.

3.3 Background

NMR Carr-Purcell-Meilboom-Gill (CPMG) measurements are widely used for rock characterization, both in the laboratory and in the field, to determine transverse relaxation (T_2) times (e.g. Coates et al., 1999; Hürlimann, 2012). The measured T_2 signal can be described for most rock systems approximately as follows (Kleinberg & Vinegar, 1996):

$$\frac{1}{T_2} = \frac{1}{T_{2,bulk}} + \rho_2 \frac{S}{V} + \frac{D\gamma^2 G^2 T_E^2}{12} \quad (3.1)$$

where $T_{2, \text{bulk}}$ is the T_2 relaxation time of the bulk fluid, ρ_2 is the surface relaxivity of the pore surface, S/V is the ratio of the pore surface to pore volume, D is the diffusion coefficient, γ is the gyromagnetic ratio of proton nucleus ($\gamma=2.68\times 10^8 \text{ T}^{-1}\text{s}^{-1}\text{rad}$ for ^1H), G is the average internal magnetic field gradient experienced by diffusing molecules between echoes (e.g. due to magnetic susceptibility differences between phases) and T_E is the echo time of the CPMG train employed. Given a large value for ρ_2 , sufficiently short echo spacing times (T_E) and weak G , **Equation (3.1)** is generally simplified as follows allowing for T_2 to be related to pore size (as accessible via the pore space S/V ratio):

$$\frac{1}{T_2} = \rho_2 \frac{S}{V} \quad (3.2)$$

Equation (3.2) assumes that the pores are rapidly sampled by the fluid molecules from which ^1H NMR signal is derived, this is the so called ‘fast diffusion limit’ (Brownstein & Tarr, 1979; Müller-Petke et al., 2015). However, due to the presence of ^1H populations originating from solid-like organic materials such as bitumen and the effect of extensive diffusive coupling across several nano-pores during the CPMG sequence, this conventional interpretation in **Equations (3.1)** and **(3.2)** may not be applicable for shales (Fleury, 2014; Washburn, 2014). A significant contribution to NMR relaxation times in shales occurs due to homonuclear dipolar-coupling interaction both with and within solid-like materials (Washburn et al., 2013).

NMR T_2 measurements are generally performed using a CPMG pulse sequence (e.g. Mitchell et al., 2013) which serves to minimize the effect of magnetic field inhomogeneities on the acquired NMR signal. The earliest signal detection in such measurements corresponds to the echo time (time between NMR signal excitation and the formation of a spin echo following application of a 180° r.f. pulse). In the case of shales this generally eliminates the NMR signal contribution from species that feature a very short T_2 (e.g. Kerogen and to a less extent bitumen and clay-bound water). The acquisition of signal from such species is more accessible via simple pulse-acquire NMR measurements - free induction decay (FID) measurements which measure the samples T_2^* relaxation time constant – where the dead time between signal excitation and detection is significantly shorter than the minimum echo time in CPMG measurements. The combined use of FID and CPMG NMR measurements has been widely used in NMR food studies such as food colloids (Mariette, 2009), baked cakes (Le Grand et al., 2007) and lipid-based foods (Trezza et al., 2006) due to the presence of semi-solid components which provide ^1H NMR signal.

The relationship between T_2 (CPMG) and T_2^* (FID) is as follows (Callaghan, 1991; Hahn, 1950):

$$\frac{1}{T_2^*} \approx \frac{1}{T_2} + \gamma\Delta B_0 + \gamma\Delta\chi B_0 \quad (3.3)$$

where ΔB_0 is the variation in magnetic field and $\Delta\chi$ is the magnetic susceptibility contrast between the rock matrix and pore fluid. The 2nd term on the right-hand side of **Equation (3.3)** relates to the inherent field inhomogeneity of the static magnetic field, while the 3rd term is the field inhomogeneity generated by susceptibility effects in the pore space. NMR signal produced using a CPMG acquisition is a summation of exponential decays which can be mathematically modelled using a Fredholm integral equation (Fredholm, 1903); application of Tikonov regularization allows for recovery of the probability distribution of T_2 values. In the case of semi-solid NMR signal characterized by very short T_2 values, signal decay is best described by a Gaussian function (Bloembergen et al., 1948). The molecular tumbling rate (correlation time) in such solids is much slower, resulting in much shorter relaxation times producing a broad Gaussian line width in the frequency domain (Abragam, 1961; Derbyshire et al., 2004; Pake, 1948). Thus for the NMR signal acquired from a sample containing both semi-solid and fluid contributions, such as shales, a weighted combination of Gaussian and Exponential decay functions is required to describe the NMR signal relaxation decay:

$$M(t) = \sum_i (A_i e^{-\left(\frac{t}{T_{2i}}\right)^2} + B_i e^{-\left(\frac{t}{T_{2i}}\right)}) \quad (3.4)$$

where $M(t)$ is measured signal, A_i is the signal intensity of Gaussian component i , B_i is the signal intensity of exponential component i , and t is the signal attenuation time. To allow for more accurate and stable simultaneous inversion of **Equation (3.4)**, a mixed Gaussian and exponential kernel function (Zhu et al., 2013) was proposed by Washburn (2014) with a regularisation penalty function featuring a sigmoidal contribution function as per **Equation (3.5)**:

$$R = M(t) - \hat{M}(t) + \sum_i (A_i \times Sig_{A_i} + B_i \times Sig_{B_i}) \quad (3.5)$$

where R is the minimized residual, $M(t)$ and $\hat{M}(t)$ are the measured and calculated data respectively, Sig_A and Sig_B are the sigmoid contribution functions that ramp down and up respectively as acquisition time increases. Sig_A and Sig_B are described by **Equations (3.6)** and **(3.7)** respectively:

$$Sig_A = \frac{1}{1+\exp(-Sig_{center} \times Sig_{width})} \times Sig_{weight} + \alpha \quad (3.6)$$

$$Sig_B = \left(1 - \frac{1}{1+\exp(-Sig_{center} \times Sig_{width})}\right) \times Sig_{weight} + \alpha \quad (3.7)$$

where Sig_{center} indicates the transition point from a T_2^* to a T_2 function, Sig_{width} is the width of the sigmoid and hence the breadth of the transition area of Gaussian and Exponential function, Sig_{weight} is the relative contribution of the sigmoid function and α is essentially the conventional smoothing parameter deployed in regularization. In our implementation, Sig_{center} was selected as the time point at which the acquired FID data transitioned to the CPMG data. The values of Sig_{width} and Sig_{weight} were optimized using some training data acquired for shales, their influence on the resultant T_2^* / T_2 distributions was however minimal.

An application of this simultaneous inversion of Gaussian and exponential decays (hereafter referred to as the SGE method) to shale samples was conducted by Washburn et al. (2015) with comparisons to the more conventional regularization approach provided by the Butler-Reed-Dawson (BRD) method with a non-negative least squares (NNLS) fit (Butler et al., 1981; Lawson & Hanson, 1995). The SGE method was shown to result in more reliable T_2 distributions for CPMG measurements respectively provided an adequate selection of Sig_{center} was made. The SGE method has also been successfully applied to NMR data acquired for a range of systems including solidification of drugs within porous matrices (Thrane et al., 2018), dynamic information of ionic liquid molecules combined with poly (vinyl alcohol) (Mattea et al., 2019) and hydration and porosity of cement stone (Holthausen & Raupach, 2019).

In the current chapter, the acquired FID and CPMG data for shales were spliced together and the SGE method applied directly to the combined single data set. The splicing was performed by using FID data acquired before the minimum echo time of 40 μ s whilst CPMG data were used for times longer than this minimum echo time. By selecting the signal intensities of the 1st data point from the CPMG measurements (corresponding to 40 μ s) and the 25th data points from FID measurements (corresponding to 40.04 μ s) and by multiplying a constant scale factor, the FID and CPMG data were scaled such they provided equivalent NMR signal intensity at 40 μ s, enabling continuous signal attenuation data for the regularization process.

3.4 Experimental Details

3.4.1 Shale Samples – Description and Preparation

Fourteen shale rock samples were sourced from across the US Permian basin and from various Australian sources. The shales total organic content (TOC) ranged from 2.0 to 5.7 wt. % with clay content between 9.1 and 32.4 wt. %, quartz content between 42.5 and 49.7 wt. % and carbonate content between 2.7 and 29.9 wt. %. The porosity of those rock samples is ranged from 0.4 % to 8.0 %. These were cut into cores with a diameter of 5 mm and a length of 12.5 mm (in order to fit into the NMR equipment available at a range of ^1H frequencies). Shale samples were stored in multiple desiccators containing various supersaturated salt solutions which acted as humectant providing for a range of relative humidity environments. Specifically, solutions of potassium sulfate, sodium chloride, potassium carbonate and potassium acetate (all purchased from Chem-supply Pty Ltd) maintained at 20 °C generated 99%, 75%, 45% and 24% relative humidity respectively (Greenspan, 1977). The shale samples were weighed every three days until successive measurements showed no change in mass. Typically, 15 days were required to ensure that equilibrium moisture adsorption had occurred. An additional low moisture state was prepared by vacuuming the samples at an absolute pressure of 0.1 bar and at a temperature of 70 °C for in excess of 7 days. All samples were initially treated using a relative humidity of 99%, which was then gradually reduced to ultimately the vacuum-dry state. **Figure 3.1** shows the mass change (and thus moisture adsorption) of the various shale samples. Most samples experienced overall moisture content increases of 1.2 -1.8 wt %. There were three exceptions where the moisture content was a lot less; we suspect this was possibly a consequence of visually confirmed surface deformation that occurred during sample preparation; the mass deviation is within the uncertainty of the measurement, potentially indicating an experimental error as well.

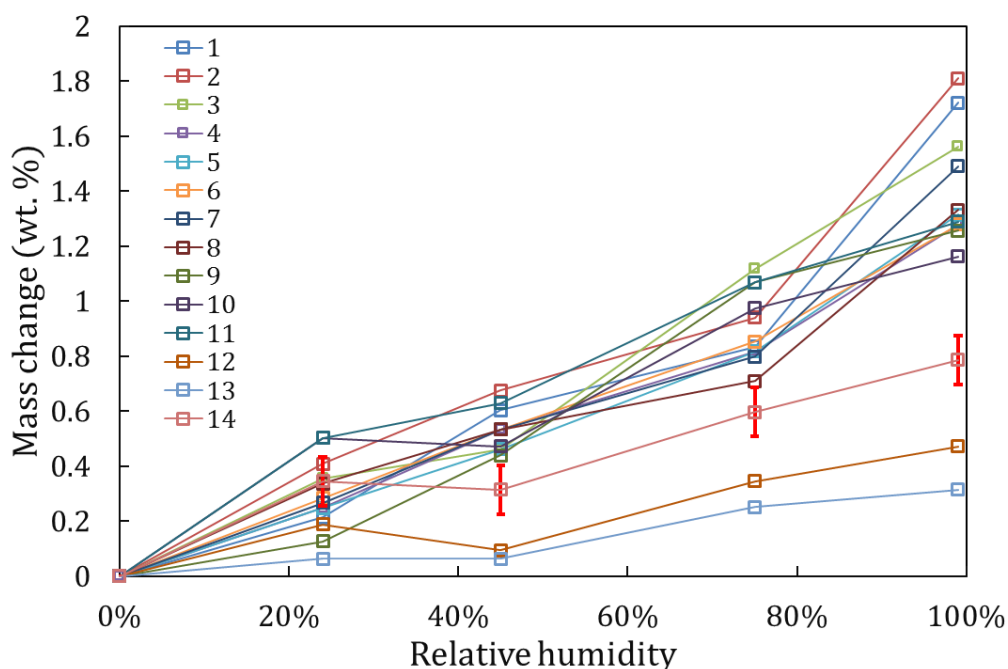


Figure 3.1. Mass changes (wt. %) of shale rock cores with relative humidity (RH) due to moisture adsorption.

A Bruker Minispec NMR spectrometer equipped with multiple magnets, corresponding to ^1H NMR frequencies of 20, 40 and 60 MHz (shown in **Figure 3.2**) was employed in this study. NMR Measurements were performed on all 14 shale samples in closed airtight sample tubes at all moisture contents considered, as summarised in **Figure 3.1**. Sample temperatures in the magnets were all controlled at 20 °C using a circulating water bath. For the CPMG measurements, the r.f. pulse length was 3.94, 8.02 and 19.2 μs for the required 180° pulse for NMR frequencies of 60, 40 and 20 MHz, respectively. A consistent echo time of 40 μs was used across all measurements (which is the minimum value possible for the instrument used) and a total of 2000 CPMG echoes were acquired. With respect to the FID acquisitions, data acquisition commenced after the minimum acquisition dead time of 17.54 μs and proceeded with a dwell time of 0.9 μs between acquisition points until a total acquisition time of 1.86 ms. The spliced data (at 40 μs) thus consisted of an initial 25 data points acquired from the FID with subsequent data points provided by the CPMG measurement. With respect to both FID and CPMG acquisitions, a total of 256 averages was used for all measurements.



Figure 3.2. Bruker Minispec NMR spectrometer with multiple magnets providing ^1H NMR frequencies of 10 (not used in this study), 20, 40 and 60 MHz, respectively.

3.5 Results and Discussion

3.5.1 Spliced FID and CPMG Data

An indicative acquired NMR data set for the spliced FID and CPMG data (the transition occurs at $40\ \mu\text{s}$ as detailed above) is presented in **Figure 3.3** for one of the shale samples at a relative humidity of 99 %. The fit of **Equation (3.4)** coupled with the SGE method is shown along with the separate component Gaussian and exponential fits respectively. The sampling rate change from the FID to the CPMG data is immediately obvious; most importantly the inability of the CPMG sequence to sample the data close to zero time would clearly mean that this contribution to the overall signal (^1H characterized by comparatively short T_2^* or T_2 values) would be lost or at least severely distorted. Equally, simply relying on the FID data would result in an inability to differentiate the more mobile (longer T_2) components of the NMR signal.

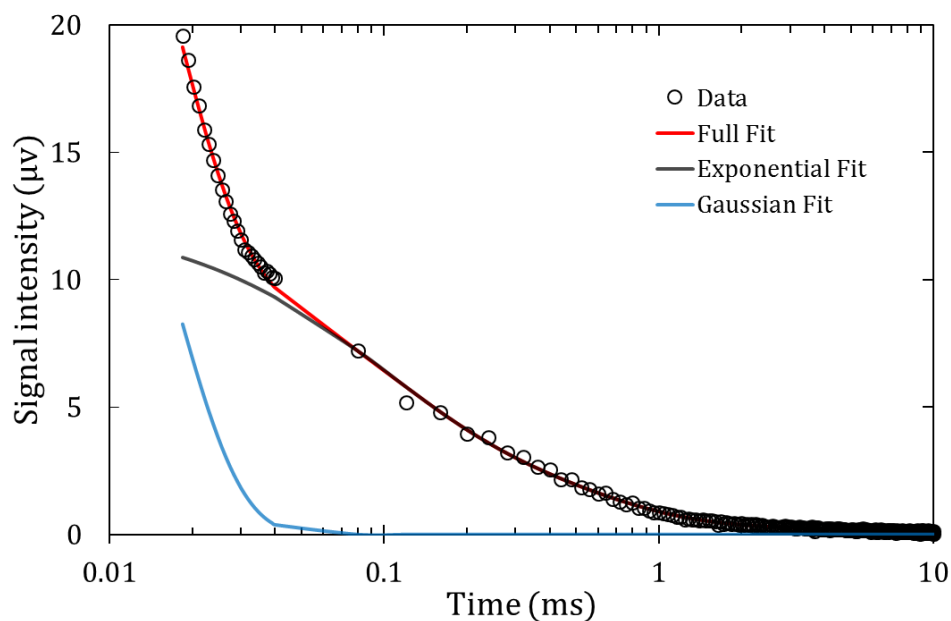


Figure 3.3. Signal attenuation fitted with the simultaneous Gaussian and Exponential (SGE) method (**Equation (3.4)** – the full fit) for a shale sample at an NMR frequency of 40 MHz and at a relative humidity of 99 %.

The resultant combined T_2^* and T_2 spectra generated from the application of **Equation (3.4)** and the SGE method (distributions of A_i and B_i from **Equation (3.4)**) are presented in **Figure 3.4(a)** for all relative humidity values considered (as well as vacuum dried) for this particular shale sample. A number of distinct peaks are evident – this was consistent across all shale samples. **Figure 3.4(b)** shows the relative change in these 3 peaks as a function of relative humidity.

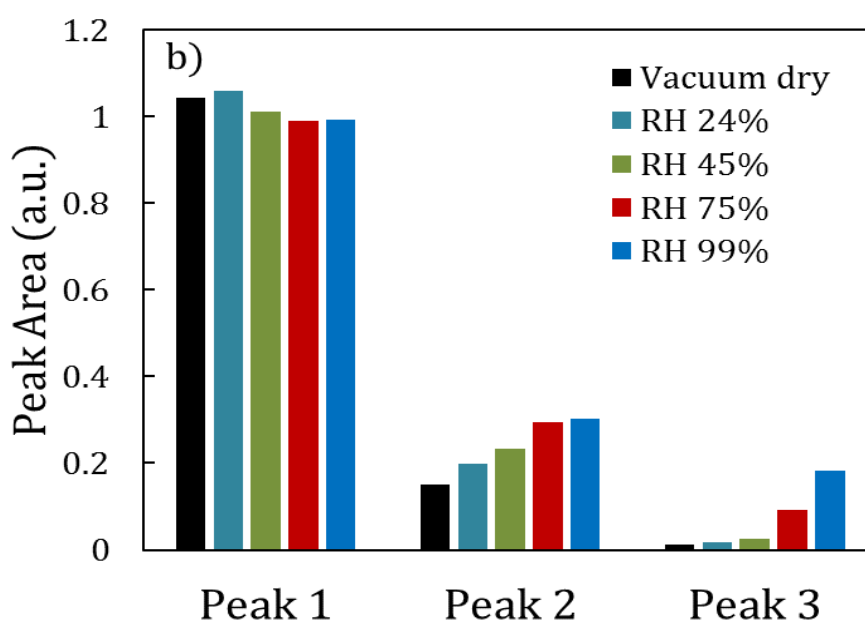
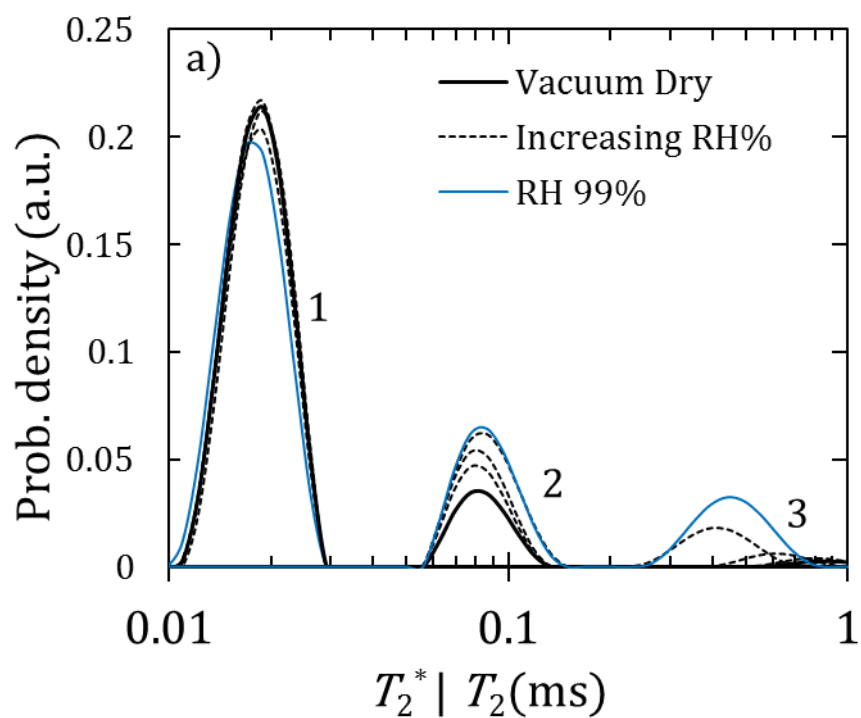


Figure 3.4. (a) Relaxation time distribution of spliced FID and CPMG method for a shale rock core sample measured at 40 MHz as a function of relative humidity. (b) Area of each of the three peaks as a function of relative humidity.

In **Figure 3.4**, the Gaussian (T_2^*) peak (Peak 1) is consistent at around a mean T_2^* of 20 μ s. It does not change significantly as relative humidity decreases and moisture is desorbed from the sample – this is consistent across all 14 shale samples. This is consistent with it

originating from the bitumen content of the sample and possibly some minor composition of clay-bound water (although we were expecting that this would be partially reduced under vacuum dried conditions – however in this particular sample, the relevant signal has increased slightly overall). Two distinct peaks are evident for the exponential component of the signal (consistently positioned at mean T_2 values of approximately 80 μs and 500 μs respectively) – these both decrease as relative humidity is reduced and thus are strongly related to the moisture content of the shale sample. Based on the results from reported 2D T_1 - T_2 maps in unconventional shales; kerogen, bitumen, clay-bound water and capillary trapped water in inorganic pores represent an ascending order of T_2 relaxation times (e.g. Kausik et al., 2017; Kausik et al., 2016; Li et al., 2018; Rylander et al., 2013). Using this extensive literature data (although the rock properties may vary from different shale samples, these data still follow the ascending trend of T_2 relaxation times), the exponential Peak 2 and Peak 3 in the work reported here are associated predominately with water adsorbed and occupying the organic and inorganic composition of the shale samples, representing the majority of the clay-bound water composition and capillary trapped water in inorganic pores respectively. What is most interesting is that as relative humidity is reduced, moisture is clearly preferentially lost from the inorganic nano-pores first (Peak 3) before being lost from the organic nano-pores (Peak 2). This behaviour, as summarised in **Figure 3.4**, was observed across all 14 shale samples analyzed.

3.5.2 Moisture Content Correlation

Figure 3.5 shows the sample results of calibrated NMR (40MHz) equivalent volumes of H_2O plotted against gravimetrically determined water uptake for all samples. The signal contribution of the dry state shale matrix has been subtracted from these data, which contributed to 60-70% of the total saturated shale sample NMR signal for the samples under study. Adequately good 1:1 correlation was observed between the two experimental methods (R^2 is 0.96) with 97% of samples falling within $\pm 1 \mu\text{L}$ bounds. This demonstrates the sensitivity of NMR measurements to reasonably determine μL increments of moisture and that no signal loss was incurred from diffusion through localized internal gradient field for measurements made at 40 MHz for these samples.

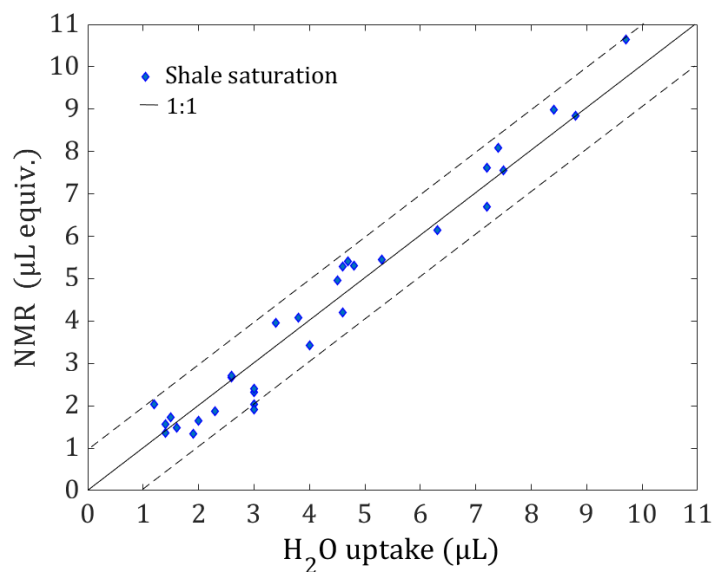


Figure 3.5. Calibrated NMR equivalent H_2O volume vs. gravimetrically measured H_2O uptake. Results are from data measured at 40 MHz.

Figure 3.6 shows the integrated area of the Gaussian and Exponential peaks as a function of sample mass for the shale sample as analyzed in **Figures 3.3** and **3.4** (where sample mass increase occurs as a consequence of moisture adsorption/absorption by the shale sample - total mass was used as opposed to total moisture content as we were unable to non-destructively determine the mass of completely moisture-free shale samples). Consistent with **Figure 3.4**, no dependency upon sample mass is evident with respect to the Gaussian peak. The integrated exponential peaks show a good linear correlation with sample mass (and hence total moisture content). Extrapolation of this data to zero NMR signal suggests that the bone-dry sample mass of this particular shale core is 0.521 g – with this assumption, the maximum moisture adsorption by this shale sample is ~1% of the total sample mass and serves to highlight the sensitivity of the analysis employed. This linear relationship between moisture content and integrated NMR exponential signal was replicated across all 14 shale samples with R^2 values greater than 0.96.

In **Figure 3.6(b)** we show the change in the individual exponential peaks (Peak 2 and 3 as introduced in **Figures 3.3** and **3.4**) as a function of total sample mass (and hence moisture content). This clearly highlights the preferential removal of moisture from Peak 3 as indicated in **Figure 3.4(b)**, which we attribute to moisture adsorbed into inorganic nano-pores in preference to the Peak 2, which we attribute to moisture adsorption into organic nano-pores, as

discussed above (Pham et al., 2007). **Figure 3.6(c)** and **(d)** show equivalent and consistent results for an alternative shale sample as proof of reproducibility – this was the case for all fourteen shale samples considered. This behavior was not observed to have any dependency on clay content of the shale samples studied.

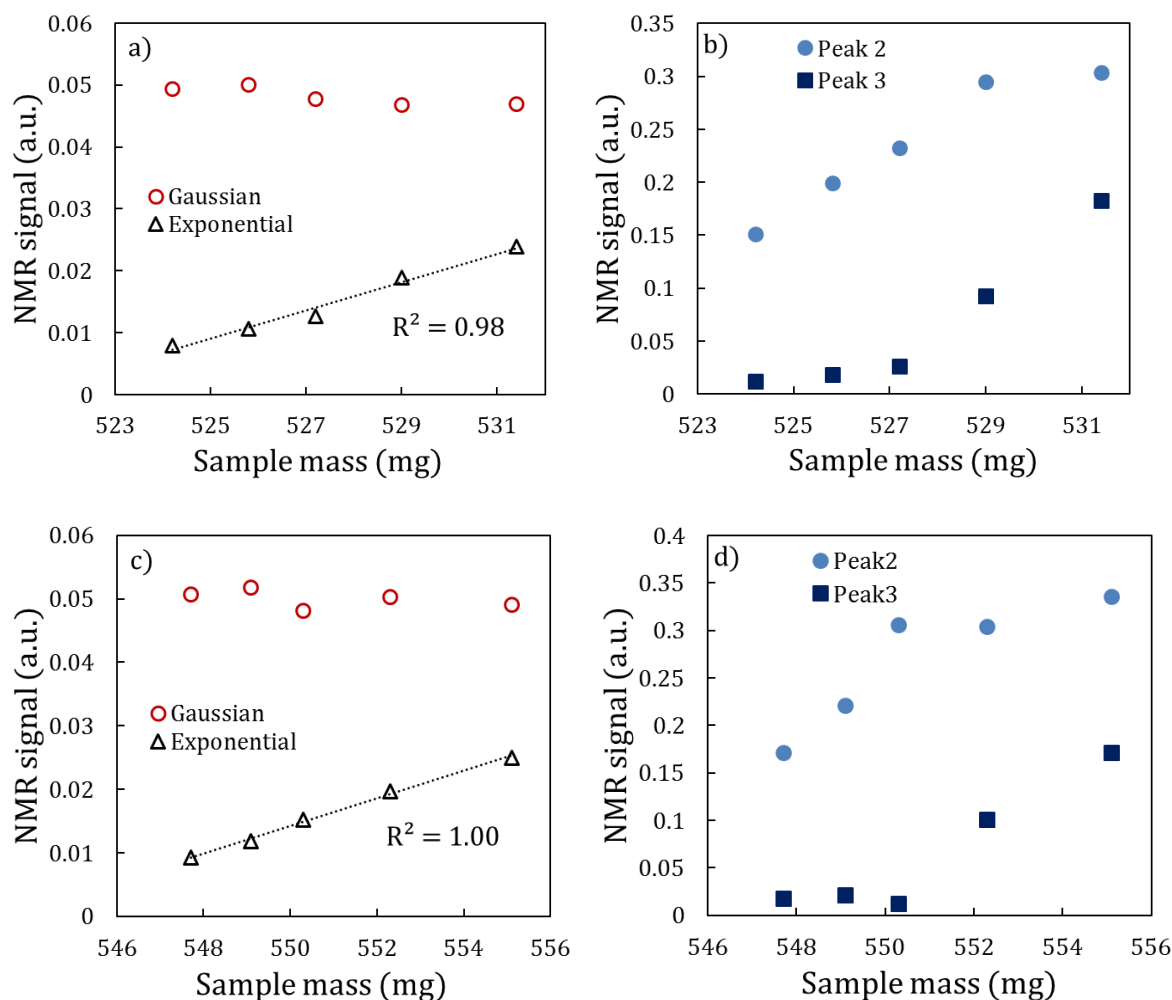


Figure 3.6. (a) Integrated Gaussian and exponential component area changes from spliced signal decays as a function of sample mass for shale rock core sample at a measured NMR frequency of 40 MHz. (b) Variation in the respective exponential peak areas as a function of sample mass (and hence moisture content). (c) and (d) Data for another shale sample showing very consistent results.

3.5.3 Organic Matter Correlation

Given the near constant Gaussian peak area evident in **Figure 3.6** for the two shale samples as a function of moisture content, we attribute this NMR signal to the semi-solid organic content of the shale samples. To test this allocation, we determined the total organic matter of adjacent shales cores (i.e. shale cores sampled immediately adjacent to the cores

studied in the current chapter cores) via standard pyrolysis methods. **Figure 3.7** presents the total Gaussian area plotted against the total organic matter content of the cores (wt. %). A reasonably good correlation is evident ($R^2= 0.91$) – the discrepancies can be attributed to the use of adjacent cores, potential contributions to the Gaussian peak by clay-bound water and finally a contribution to the organic content by the shale kerogen content. In addition, the linear fit is consistent with a minimal Gaussian peak at zero organic matter. This Gaussian peak signal was also found to have no relationship with the clay content of the shales.

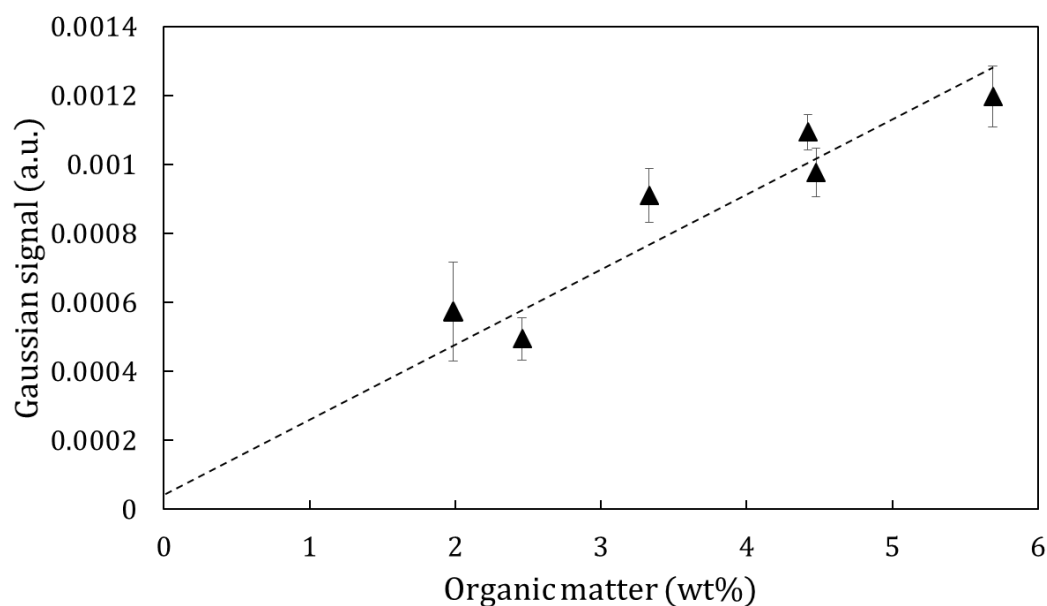


Figure 3.7. Correlation of Gaussian peak signal (area) with independently measured organic matter content of shale rock cores.

3.5.4 Influence of ^1H NMR Measurements Frequency

The NMR analysis as presented in **Figures 3.3-3.6** was repeated at NMR frequencies of 20, 40 and 60 MHz respectively. For each sample the standard deviation in the area of the Gaussian peak (across the measurements at variable relative humidity) is shown in **Figure 3.8** as a function of frequency. Essentially a standard deviation of zero would be completely consistent with our assumption that this signal originated from bitumen content and thus is invariant with total moisture content – for reference the shale sample presented in **Figure 3.4** and 3.6 corresponds to Sample #6 at 40 MHz. Two distinct trends emerged. For shale samples which featured the largest moisture adsorption amounts (shale samples labeled 1-8), the lowest standard deviations occurred at 40 and 60 MHz (these data are plotted in **Figure 3.8**) a marked

deterioration occurred at 20 MHz. However for the data for shale samples numbered from 9 to 14 (which featured the smallest moisture adsorption amounts) no systematic trend is evident, the standard deviations obtained from 20 and 60 MHz are comparable. We suspect the greater standard deviation for measurements at 40 MHz is an instrument artefact. This consistent variation in behavior dependent on moisture content adsorption is subject to further study.

NMR frequencies (ranging over 2, 12 and 23 MHz respectively) has been suggested in the literature to have limited impact on the performance of 1D NMR relaxometry characterization on shales with no appreciable shift in the T_2 values of various component phases. In addition, by applying higher NMR frequencies, both an inherently better SNR and access to short T_2 components is further increased by a reduction in instrument dead-time (Anger et al., 2016; Min et al., 2019). In this study, there is no evidence to suggest a dramatic deterioration in the quality of the NMR data (as assessed via this criterion of consistent quantitative bitumen detection) as NMR frequency is increased and there is some evidence that a larger frequency is preferential for these SNR challenged shale systems. In all the samples the standard deviation of the Gaussian peaks was lower for the spliced data when compared to simply acquiring and analyzing the FID data. Furthermore the linearity of the exponential peak with moisture adsorption (as shown in **Figure 3.5** and **3.6**) was found to be independent of frequency employed across all fourteen samples ($R^2 > 0.97$).

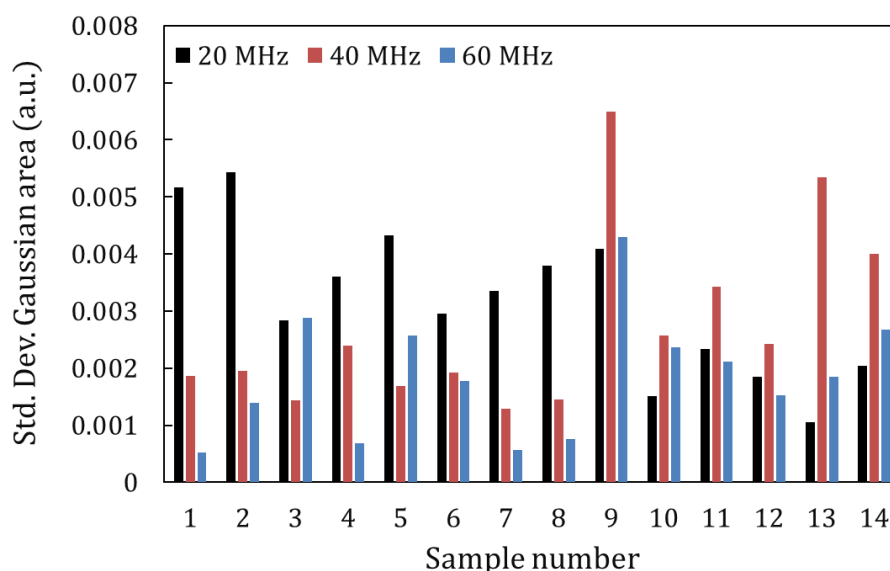


Figure 3.8. Standard deviation of the Gaussian component area (as determined across the different relative humidities applied) for different NMR frequencies.

3.6 Conclusions

NMR FID and CPMG measurements were conducted at ^1H NMR frequencies of 20, 40 and 60 MHz on shales to characterize their complex compositions in terms of viscous semi-solid bitumen and capillary trapped water in organic/inorganic pores by varying the relative humidity of the saturation environment. This featured the novel application of a simultaneous Gaussian and exponential (SGE) data inversion to spliced FID and CPMG NMR attenuation data to interpret proton populations originated from different components in the shale. Gaussian peak areas of the shales were consistently independent of decreasing relative humidity, suggesting that this signal was due to solid-like bitumen content in the shale. The magnitude of this Gaussian peak was shown to scale with organic content, as destructively measured on adjacent shale samples. The exponential peaks areas showed excellent and consistent linear correlation with the increase in sample mass due to moisture addition – as relative humidity was reduced, moisture was observed to be removed first from larger inorganic pores featuring longer T_2 values. The standard deviation of the Gaussian component signal total was broadly consistent across the range of ^1H frequencies (20 to 60 MHz) and shale samples analyzed, indicating no systematic deterioration in NMR data quality as frequency was increased.

3.7 References

- Abragam, A. (1961). *The Principles of Nuclear Magnetic Resonance*. Clarendon, Oxford.
- AlGhamdi, T. M., Arns, C. H., & Eyvazzadeh, R. Y. (2013). Correlations between NMR-relaxation response and relative permeability from tomographic reservoir-rock images. *SPE Reservoir Evaluation and Engineering*, 16(4). <https://doi.org/10.2118/160870-pa>
- Anger, B., Rydzy, M., Ramskill, N., Hertel, S., Sederman, A., Gladden, L., & Appel, M. (2016). Multi-Frequency NMR and TGA Characterization of TOC in Shales. *International Symposium of the Society of Core Analysts*, 1–12. <http://www.jgmaas.com/SCA/2016/SCA2016-025.pdf>
- Arns, C. H. (2004). A comparison of pore size distributions derived by NMR and X-ray-CT techniques. *Physica A: Statistical Mechanics and Its Applications*, 339(1–2), 159–165. <https://doi.org/10.1016/j.physa.2004.03.033>

- Bloembergen, N., Purcell, E. M., & Pound, R. V. (1948). Relaxation effects in nuclear magnetic resonance absorption. *Physical Review*, 73(7), 679–712. <https://doi.org/10.1103/PhysRev.73.679>
- Brownstein, K. R., & Tarr, C. E. (1979). Importance of classical diffusion in NMR studies of water in biological cells. *Physical Review A*, 19(6), 2446–2453. <https://doi.org/10.1103/PhysRevA.19.2446>
- Butler, J. P., Reeds, J. A., & Dawson, S. V. (1981). Estimating Solutions of First Kind Integral Equations with Nonnegative Constraints and Optimal Smoothing. *SIAM Journal on Numerical Analysis*, 18(3), 381–397. <https://doi.org/10.1137/0718025>
- Callaghan, P. T. (1991). *Principles of Nuclear Magnetic Resonance Microscopy*. Clarendon Press, Oxford.
- Chalmers, G. R., Bustin, R. M., & Power, I. M. (2012). Characterization of gas shale pore systems by porosimetry, pycnometry, surface area, and field emission scanning electron microscopy/ transmission electron microscopy image analyses: Examples from the Barnett, Woodford, Haynesville, Marcellus, and Doig units. *AAPG Bulletin*, 96(6), 1099–1119. <https://doi.org/10.1306/10171111052>
- Chenevert, M. (1970). Shale Alteration By Water Adsorption. *JPT, Journal of Petroleum Technology*, 22(9), 1141–1148. <https://doi.org/10.2118/2401-pa>
- Coates, G., Xiao, L., & Prammer, M. (1999). *NMR logging: Principles and applications*. Halliburton Energy Services.
- Connolly, P. R. J., Yan, W., Zhang, D., Mahmoud, M., Verrall, M., Lebedev, M., Iglauer, S., Metaxas, P. J., May, E. F., & Johns, M. L. (2019). Simulation and experimental measurements of internal magnetic field gradients and NMR transverse relaxation times (T₂) in sandstone rocks. *Journal of Petroleum Science and Engineering*, 175, 985–997. <https://doi.org/10.1016/j.petrol.2019.01.036>
- Davies, S., Kalam, M. Z., Packer, K. J., & Zelaya, F. O. (1990). Pore-size distributions from nuclear magnetic resonance spin-lattice relaxation measurements of fluid-saturated porous solids. II. Applications to reservoir core samples. *Journal of Applied Physics*, 67(6), 3171–3176. <https://doi.org/10.1063/1.345396>
- Davies, S., & Packer, K. J. (1990). Pore-size distributions from nuclear magnetic resonance

- spin-lattice relaxation measurements of fluid-saturated porous solids. I. Theory and simulation. *Journal of Applied Physics*, 67(6), 3163–3170. <https://doi.org/10.1063/1.345395>
- Derbyshire, W., Van Den Bosch, M., Van Dusschoten, D., MacNaughtan, W., Farhat, I. A., Hemminga, M. A., & Mitchell, J. R. (2004). Fitting of the beat pattern observed in NMR free-induction decay signals of concentrated carbohydrate-water solutions. *Journal of Magnetic Resonance*, 168(2), 278–283. <https://doi.org/10.1016/j.jmr.2004.03.013>
- Fleury, M. (2014). Characterization of Shales With Low Field Nmr. *Sca*, 1–12.
- Fleury, Marc, & Romero-Sarmiento, M. (2016). Characterization of shales using T1-T2 NMR maps. *Journal of Petroleum Science and Engineering*, 137, 55–62. <https://doi.org/10.1016/j.petrol.2015.11.006>
- Fredholm, I. (1903). Sur une classe d'équations fonctionnelles. *Acta Mathematica*, 27(1), 365–390. <https://doi.org/10.1007/BF02421317>
- Greenspan, L. (1977). Humidity Fixed Points of Binary Saturated Aqueous Solutions. *J Res Natl Bur Stand Sect A Phys Chem*, 81 A(1), 89–96. <https://doi.org/10.6028/jres.081A.011>
- Hahn, E. L. (1950). Nuclear induction due to free larmor precession [18]. *Physical Review*, 77(2), 297–298. <https://doi.org/10.1103/PhysRev.77.297.2>
- Holthausen, R., & Raupach, M. (2019). A phenomenological approach on the influence of paramagnetic iron in cement stone on 2D T 1 -T 2 relaxation in single-sided 1 H nuclear magnetic resonance. *Cement and Concrete Research*, 120, 279–293. <https://doi.org/10.1016/j.cemconres.2019.03.027>
- Hürlimann, M. D. (2012). Well Logging. *Encyclopedia of Magnetic Resonance*. <https://doi.org/10.1002/9780470034590.emrstm0593.pub2>
- Jia, C. (2017). Breakthrough and significance of unconventional oil and gas to classical petroleum geology theory. *Petroleum Exploration and Development*, 44(1), 1–10. [https://doi.org/10.1016/S1876-3804\(17\)30002-2](https://doi.org/10.1016/S1876-3804(17)30002-2)
- Josh, M., Esteban, L., Delle Piane, C., Sarout, J., Dewhurst, D. N., & Clennell, M. B. (2012). Laboratory characterisation of shale properties. *Journal of Petroleum Science and Engineering*, 88–89, 107–124. <https://doi.org/10.1016/j.petrol.2012.01.023>

- Kausik, R., Fellah, K., Feng, L., & Simpson, G. (2017). High- and low- field NMR relaxometry and diffusometry of the Bakken petroleum system. *Petrophysics*, 58(04), 341–351.
- Kausik, Ravinath, Fellah, K., Rylander, E., Singer, P. M., Lewis, R. E., & Sinclair, S. M. (2014). Nmr Petrophysics for Tight Oil Shale Enabled By Core Resaturation. *Nternational Symposium of the Society of Core Analysts*, 1–6.
- Kausik, Ravinath, Fellah, K., Rylander, E., Singer, P. M., Lewis, R. E., & Sinclair, S. M. (2016). NMR relaxometry in shale and implications for logging. *SPWLA 56th Annual Logging Symposium 2015*.
- Kleinberg, R. L., & Vinegar, H. J. (1996). NMR properties of reservoir fluids. *Log Analyst*, 37(6), 20–32.
- Kleinberg, Robert L. (2001). NMR well logging at Schlumberger. *Concepts in Magnetic Resonance*, 13(6), 396–403. <https://doi.org/10.1002/cmr.1026>
- Lawson, C., & Hanson, R. (1995). *Solving Least Squares Problems*. Houston, Texas.
- Le Grand, F., Cambert, M., & Mariette, F. (2007). NMR signal analysis to characterize solid, aqueous, and lipid phases in baked cakes. *Journal of Agricultural and Food Chemistry*, 55(26), 10947–10952. <https://doi.org/10.1021/jf071735r>
- Li, Z., Das, S., Hongmanorom, P., Dewangan, N., Wai, M. H., & Kawi, S. (2018). Silica-based micro- and mesoporous catalysts for dry reforming of methane. *Catalysis Science and Technology*, 8(11), 2763–2778. <https://doi.org/10.1039/c8cy00622a>
- Logan, W. D., Horkowitz, J. P., Laronga, R., & Cromwell, D. W. (1998). Practical Application of NMR Logging in Carbonate Reservoirs. *SPE Reservoir Engineering (Society of Petroleum Engineers)*, 1(5), 438–448. <https://doi.org/10.2118/51329-pa>
- Loucks, R. G., Reed, R. M., Ruppel, S. C., & Jarvie, D. M. (2009). Morphology, genesis, and distribution of nanometer-scale pores in siliceous mudstones of the mississippian barnett shale. *Journal of Sedimentary Research*, 79(12), 848–861. <https://doi.org/10.2110/jsr.2009.092>
- Mariette, F. (2009). Investigations of food colloids by NMR and MRI. *Current Opinion in Colloid and Interface Science*, 14(3), 203–211. <https://doi.org/10.1016/j.cocis.2008.10.006>

- Mattea, C., Gizatullin, B., & Stapf, S. (2019). Dynamics of ionic liquids in poly(vinyl alcohol) porous scaffold. Low field NMR study. *Magnetic Resonance Imaging*, *56*, 126–130. <https://doi.org/10.1016/j.mri.2018.09.032>
- Mehana, M., & El-monier, I. (2016). Shale characteristics impact on Nuclear Magnetic Resonance (NMR) fluid typing methods and correlations. *Petroleum*, *2*(2), 138–147. <https://doi.org/10.1016/j.petlm.2016.02.002>
- Min, B., Sondergeld, C. H., & Rai, C. S. (2019). Investigation of high frequency 1D NMR to characterize reservoir rocks. *Journal of Petroleum Science and Engineering*, *176*, 653–660. <https://doi.org/10.1016/j.petrol.2019.01.093>
- Minh, C., Crary, S., Zielinski, L., Liu, C. B., Jones, S., & Jacobsen, S. (2012). 2D-NMR applications in unconventional reservoirs. *Society of Petroleum Engineers - SPE Canadian Unconventional Resources Conference 2012, CURC 2012*, *1*, 87–103. <https://doi.org/10.2118/161578-ms>
- Mitchell, J., Chandrasekera, T. C., Holland, D. J., Gladden, L. F., & Fordham, E. J. (2013). Magnetic resonance imaging in laboratory petrophysical core analysis. *Physics Reports*, *526*(3), 165–225. <https://doi.org/10.1016/j.physrep.2013.01.003>
- Mitchell, J., Chandrasekera, T. C., Johns, M. L., Gladden, L. F., & Fordham, E. J. (2010). Nuclear magnetic resonance relaxation and diffusion in the presence of internal gradients: The effect of magnetic field strength. *Physical Review E - Statistical, Nonlinear, and Soft Matter Physics*, *81*(2). <https://doi.org/10.1103/PhysRevE.81.026101>
- Müller-Petke, M., Dlugosch, R., Lehmann-Horn, J., & Ronczka, M. (2015). Nuclear magnetic resonance average pore-size estimations outside the fast-diffusion regime. *Geophysics*, *80*(3), D195–D206. <https://doi.org/10.1190/GEO2014-0167.1>
- Nikolaev, M. Y., & Kazak, A. V. (2019). Liquid saturation evaluation in organic-rich unconventional reservoirs: A comprehensive review. *Earth-Science Reviews*, *194*, 327–349. <https://doi.org/10.1016/j.earscirev.2019.05.012>
- Oduşina, E., & Sigal, R. F. (2011). Laboratory NMR measurements on methane saturated barnett shale samples. *Petrophysics*, *52*(1), 32–49.
- Oduşina, E., Sondergeld, C., & Rai, C. (2011). An NMR study on shale wettability. *Society of Petroleum Engineers - Canadian Unconventional Resources Conference 2011, CURC*

2011, 1, 515–529. <https://doi.org/10.2118/147371-ms>

- Pake, G. E. (1948). Nuclear resonance absorption in hydrated crystals: Fine structure of the proton line. *The Journal of Chemical Physics*, 16(4), 327–336. <https://doi.org/10.1063/1.1746878>
- Pham, Q. T., Vales, F., Malinsky, L., Nguyen Minh, D., & Gharbi, H. (2007). Effects of desaturation-resaturation on mudstone. *Physics and Chemistry of the Earth*, 32(8–14), 646–655. <https://doi.org/10.1016/j.pce.2006.03.012>
- Ratner, M., & Tiemann, M. (2014). An overview of unconventional oil and natural gas: Resources and federal actions. In *Energy Diversity for Economic Progress: Strategy and Issues*.
- Rylander, E., Singer, P. M., Jiang, T., Lewis, R., McLin, R., & Sinclair, S. (2013). NMR T2 distributions in the Eagle Ford shale: Reflections on pore size. *Society of Petroleum Engineers - SPE USA Unconventional Resources Conference 2013*, 426–440. <https://doi.org/10.2118/164554-ms>
- Sang, G., Liu, S., & Elsworth, D. (2019). Water Vapor Sorption Properties of Illinois Shales Under Dynamic Water Vapor Conditions: Experimentation and Modeling. *Water Resources Research*, 55(8), 7212–7228. <https://doi.org/10.1029/2019WR024992>
- Seymour, J., Washburn, K., Kirkland, C., Vogt, S., Birdwell, J., & Codd, S. (2013). NMR measurement of oil shale magnetic relaxation at high magnetic field. *International Symposium of the Society of Core Analysts*.
- Song, Y., & Kausik, R. (2019). NMR application in unconventional shale reservoirs – A new porous media research frontier. *Progress in Nuclear Magnetic Resonance Spectroscopy*, 112–113, 17–33. <https://doi.org/10.1016/J.PNMRS.2019.03.002>
- Straley, C. (1997). An experimental investigation of methane in rock materials. *SPWLA 38th Annual Logging Symposium 1997*.
- Sulucarnain, I., Sondergeld, C. H., & Rai, C. S. (2012). An NMR study of shale wettability and effective surface relaxivity. *Society of Petroleum Engineers - SPE Canadian Unconventional Resources Conference 2012, CURC 2012*, 1, 356–366. <https://doi.org/10.2118/162236-ms>
- Testamanti, M. N., & Rezaee, R. (2017). Determination of NMR T2 cut-off for clay bound

- water in shales: A case study of Carynginia Formation, Perth Basin, Western Australia. *Journal of Petroleum Science and Engineering*, 149, 497–503. <https://doi.org/10.1016/j.petrol.2016.10.066>
- Thrane, L. W., Berglund, E. A., Wilking, J. N., Vodak, D., & Seymour, J. D. (2018). Nmr relaxometry to characterize the drug structural phase in a porous construct. *Molecular Pharmaceutics*, 15(7), 2614–2620. <https://doi.org/10.1021/acs.molpharmaceut.8b00144>
- Tinni, A., Odusina, E., Sulucarnain, I., Sondergeld, C., & Rai, C. S. (2015). Nuclear-magnetic-resonance response of brine, oil, and methane in organic-rich shales. *SPE Reservoir Evaluation and Engineering*, 18(3), 400–406. <https://doi.org/10.2118/168971-PA>
- Tokunaga, T. K., Shen, W., Wan, J., Kim, Y., Cihan, A., Zhang, Y., & Finsterle, S. (2017). Water Saturation Relations and Their Diffusion-Limited Equilibration in Gas Shale: Implications for Gas Flow in Unconventional Reservoirs. *Water Resources Research*, 53(11), 9757–9770. <https://doi.org/10.1002/2017WR021153>
- Trezza, E., Haiduc, A. M., Goudappel, G. J. W., & Van Duynhoven, J. P. M. (2006). Rapid phase-compositional assessment of lipid-based food products by time domain NMR. *Magnetic Resonance in Chemistry*, 44(11), 1023–1030. <https://doi.org/10.1002/mrc.1893>
- U.S. Energy Information Administration. (2019). *Annual Energy Outlook 2019*. Outlook. https://www.eia.gov/outlooks/aeo/case_descriptions.php
- Wang, H., Li, G., & Shen, Z. (2012). A feasibility analysis on shale gas exploitation with supercritical carbon dioxide. *Energy Sources, Part A: Recovery, Utilization and Environmental Effects*, 34(15), 1426–1435. <https://doi.org/10.1080/15567036.2010.529570>
- Washburn, K., Birdwell, J., Seymour, J., Kirkland, C., & Vogt, S. (2013). Low-Field Nuclear Magnetic Resonance Characterization of Organic Content in Shales. *Scaweb.Org*, 1–12. http://www.scaweb.org/assets/papers/2013_papers/SCA2013-002.pdf
- Washburn, K. E. (2014). Relaxation mechanisms and shales. *Concepts in Magnetic Resonance Part A: Bridging Education and Research*, 43A(3), 57–78. <https://doi.org/10.1002/cmr.a.21302>
- Washburn, K. E., Anderssen, E., Vogt, S. J., Seymour, J. D., Birdwell, J. E., Kirkland, C. M., & Codd, S. L. (2015). Simultaneous Gaussian and exponential inversion for improved

- analysis of shales by NMR relaxometry. *Journal of Magnetic Resonance*, 250, 7–16.
<https://doi.org/10.1016/j.jmr.2014.10.015>
- Washburn, K. E., & Birdwell, J. E. (2013). Updated methodology for nuclear magnetic resonance characterization of shales. *Journal of Magnetic Resonance*, 233, 17–28.
<https://doi.org/10.1016/j.jmr.2013.04.014>
- Xie, Z., Gan, Z. (2018). Value of 20 MHz NMR core analysis for unconventional mudstones. *Proceedings of the SPWLA 59th Annual Logging Symposium*.
- Yan, W., Sun, J., Golsanami, N., Li, M., Cui, L., Dong, H., & Sun, Y. (2019). Evaluation of wettabilities and pores in tight oil reservoirs by a new experimental design. *Fuel*, 252, 272–280. <https://doi.org/10.1016/j.fuel.2019.04.130>
- Yang, D., & Kausik, R. (2016). ²³Na and ¹H NMR Relaxometry of Shale at High Magnetic Field. *Energy and Fuels*, 30(6), 4509–4519.
<https://doi.org/10.1021/acs.energyfuels.6b00130>
- Yuan, Y., Rezaee, R., Verrall, M., Hu, S. Y., Zou, J., & Testmanti, N. (2018). Pore characterization and clay bound water assessment in shale with a combination of NMR and low-pressure nitrogen gas adsorption. *International Journal of Coal Geology*, 194, 11–21. <https://doi.org/10.1016/j.coal.2018.05.003>
- Zhao, Y., Song, Y., Liu, Y., Jiang, L., & Zhu, N. (2011). Visualization of CO₂ and oil immiscible and miscible flow processes in porous media using NMR micro-imaging. *Petroleum Science*, 8(2), 183–193. <https://doi.org/10.1007/s12182-011-0133-1>
- Zhu, H., Huinink, H. P., Magusin, P. C. M. M., Adan, O. C. G., & Kopinga, K. (2013). T2 distribution spectra obtained by continuum fitting method using a mixed Gaussian and exponential kernel function. *Journal of Magnetic Resonance*, 235, 109–114.
<https://doi.org/10.1016/j.jmr.2013.08.002>

Chapter 4 Low-field NMR Relaxation Analysis of Ethane

Adsorption in Mesoporous Silicas

Foreword – The contents of this chapter has been published in *ChemPhysChem* in 2022. It has been reformatted with minor amendments to fit the style and structure of this thesis. As a precursor to the adsorption of short-chain hydrocarbons in shales, this chapter presents the dynamics of ethane confined in model mesoporous silica materials with mean pore diameters between 6 and 50 nm within a pressure range from 25 to 50 bar and at ambient temperature, which incorporates the ethane condensation point. The application of T_2 and diffusion coefficient distributions is demonstrated as a means to decouple bulk and mesopore-dominated excess adsorption phenomena.

4.1 Abstract

Understanding the behaviour of short-chain hydrocarbons confined to porous solids informs the targeted extraction of natural resources from geological features, and underpins rational developments in separation, storage and catalytic conversion processes. Here we report the application of low-field (12.7 MHz) ^1H nuclear magnetic resonance (NMR) relaxation measurements to characterize ethane dynamics within mesoporous silica materials exhibiting mean pore diameters between 6 and 50 nm. Our measurements provide NMR-based adsorption isotherms within the range 25-50 bar and at ambient temperature, incorporating the ethane condensation point (40.7 bar at our experimental temperature of 23.6 °C). The quantitative nature of the acquired data is validated via a direct comparison of NMR-derived excess adsorption capacities with ex situ gravimetric ethane adsorption measurements, which are demonstrated to agree to within 0.2 mmol/g of the observed ethane capacity. NMR T_2 relaxation time distributions are further demonstrated as a means to decouple interparticle and mesopore dominated adsorption phenomena, with unexpectedly rapid relaxation rates associated with interparticle ethane gas confirmed via a direct comparison with NMR self-diffusion analysis.

4.2 Introduction

Mesoporous materials (exhibiting pore structures 2-50 nm in diameter) find widespread applications across separation, storage and catalytic processes, wherein their efficacy is conferred by inherently large surface-to-volume ratios and high degrees of pore surface accessibility (Rouquerol et al., 2013). Understanding the adsorption and uptake of gaseous hydrocarbons within such materials underpins their rational design for the upgrading of chemical feedstocks (Li et al., 2018; Oschatz et al., 2017), and provides well-defined model systems with which to inform the extraction of resources from natural hydrocarbon reserves, such as shale formations (Chiang et al., 2016). Oxide-based materials, including silicas (SiO_2), aluminas (Al_2O_3) and titanias (TiO_2), offer ubiquitous and tuneable mesoporous frameworks for such applications (Ren et al., 2012). For instance, metal oxides are known to provide a range of active pore surface properties including photoactive centres (Cybula et al., 2015) and catalytic acid and base sites (Haneda et al., 2001; Saito et al., 2021), while silica-based materials, including gels and colloidally-templated frameworks, provide inert substrates with highly controllable pore topologies (Berggren et al., 2005; Dutta et al., 2005; Hyde et al., 2016).

Traditional approaches to characterize gas uptake phenomena within mesoporous materials are based on gravimetric or volumetric measurements. Such methods are established across a range of pressure and temperature conditions (Watson et al., 2011; Wu et al., 2019; Yun et al., 2002), providing quantitative routes to molecular uptake data, and via the application of well-established models facilitate the characterization of material properties including pore size distributions and accessible surface areas (Thommes et al., 2015). However, drawbacks of such analyses include long experimental time scales (hours-to-days) and the requirement for access to specialist sorption hardware. Here we explore alternative routes to hydrocarbon gas uptake data via the application of time-domain nuclear magnetic resonance (NMR) measurements. NMR spectroscopy is a universally applied characterization technique for establishing molecular and solid-state structures; however, in the case of fluids confined to mesoporous materials the insight available from such frequency-domain chemical shift data is usually limited by significant line-broadening effects (Terenzi et al., 2019), which occur as a result of local magnetic field distortions due to magnetic susceptibility differences across the solid-fluid interface (Mitchell et al., 2010). Time-domain NMR measurements instead probe the decay rates of observable NMR signals as a result of molecular dynamics, and are broadly immune to such magnetic field distortions. NMR relaxation measurements probe the longitudinal and/or transverse relaxation behaviour of the spin system under investigation, as

characterized by the time constants T_1 and T_2 , respectively. These time constants exhibit well-defined relationships with molecular rotational and translational dynamics within the unrestricted bulk liquid phase (Kowalewski & Mäler, 2017). For fluids confined to porous solids, however, the correspondence between time constants and molecular dynamics is perturbed by the attendant pore structure (Kinn et al., 2019; Korb, 2018), facilitating characterization of a range of material and interfacial properties including pore sizes (Davies & Packer, 1990; Silletta et al., 2018) and connectivity (Isaacs et al., 2020; Mitchell et al., 2007; Washburn & Callaghan, 2006), surface areas (Chen et al., 2013, 2015), confinement effects (Korb et al., 1993; Korb et al., 1994; Witherspoon et al., 2017) and adsorption interactions (D'Agostino et al., 2014; Robinson et al., 2018, 2021; Ward-Williams et al., 2018; Ward-Williams & Gladden, 2019; Ward-Williams et al., 2021; Weber et al., 2009). Papaioannou *et al.* (Papaioannou & Kausik, 2015) recently employed a range of high-field NMR relaxation measurements to investigate methane storage within mesoporous (5.7 nm diameter pores) Vycor glass (silica) at 7 – 897 bar, demonstrating the sensitivity of such measurements to both monolayer and multilayer adsorption phenomena. Alternatively, pulsed field gradient (PFG) NMR diffusion measurements apply a series of short magnetic field gradient pulses to track the diffusive displacement of NMR-active species across a set observation period (Price, 1997). PFG NMR diffusion measurements have been applied to a wide range of fluids confined within mesoporous solids, facilitating the elucidation of restricted mass transport phenomena (Kärger et al., 2021) and surface dynamics (Dvoyashkin et al., 2009; Robinson & D'Agostino, 2020; Weber et al., 2010), together with material characteristics including pore structure tortuosity values (D'Agostino et al., 2012; Isaacs et al., 2019; Rottreau et al., 2017) and pore isotropies (Kondrashova et al., 2017; Naumov et al., 2008; Stallmach et al., 2000). High-field PFG NMR measurements have been reported for the characterization of short-chain hydrocarbon gas dynamics within a range of templated mesoporous silica materials (Hu et al., 2016; Hu et al., 2017; Hu et al., 2017).

In the present work we demonstrate the utility of low magnetic field NMR relaxation and diffusion measurements for the characterization of hydrocarbon gas dynamics within mesoporous silica materials. Low-field NMR experiments utilise benchtop instruments equipped with permanent magnet-based hardware (Blümich, 2019; Johns et al., 2015; Mitchell et al., 2014), and provide a number of advantages over classical high-field superconducting NMR equipment, including increased portability, reduced safety considerations and negligible maintenance requirements; such characteristics lend low-field NMR equipment to

straightforward integration with high-pressure apparatus (Duchowny et al., 2021; Kerr et al., 2019; Tang et al., 2019). Low-field experimentation is further advantageous in the characterization of T_2 transverse relaxation processes, wherein reduced magnetic field strengths limit undesirable magnetic susceptibility contrast effects at the solid/fluid interfaces, which result in enhanced rates of transverse relaxation (Mitchell et al., 2010). Low-field relaxation and diffusion measurements have been reported for methane within a variety of microporous solids including carbons (Horch et al., 2014; Thern et al., 2018), zeolites (Robinson et al., 2020), MOFs (Horch et al., 2014), while direct integration with volumetric sorption hardware has also been demonstrated in the case of vapour phase alcohols (Marreiros et al., 2021). Here, we extend this field through the investigation of ethane sorption within a range of mesoporous silicas exhibiting a well-defined range of mean pore diameters (6, 15 and 50 nm). Our measurements are performed across the pressure range 25-50 bar, which at room temperature incorporates the condensation point of bulk ethane, and detail direct comparisons between time-domain NMR measurements and conventional gravimetric sorption analysis.

4.3 Theoretical Background

4.3.1 Adsorption and Capillary Condensation

Adsorption processes involve the thermodynamically favourable adhesion of chemical species to solid surfaces (Kolasinski, 2020). For hydrocarbon gases in the vicinity of oxide surfaces such interactions occur via a non-dissociative physisorption mechanism (Thommes et al., 2015), which increases the molecular density of the adsorbed surface layer to near that of the condensed phase. Capillary condensation then describes the phenomenon whereby the multilayer adsorption of confined gas leads to condensation at pressures below the bulk saturation pressure of the imbibed fluid (Fisher & Israelachvili, 1979). This process is traditionally described by way of the Kelvin equation (Thomson, 1872), which takes the form (Mitropoulos, 2008):

$$P_{vap} = P_{sat} \exp\left(\frac{-2\gamma_l V_l \cos \theta}{rRT}\right). \quad (4.1)$$

Here P_{vap} is the vapour pressure at which capillary condensation emerges, P_{sat} is the bulk saturation pressure, γ_l are V_l are the surface tension and molar volume of the adsorbed

liquid, respectively, θ is the contact angle, r is the mean pore radius, R is the gas constant and T is the absolute temperature.

4.3.2 NMR Relaxation and Diffusion in Porous Media

In this work we focus on the transverse ^1H (proton) relaxation behaviour of free and confined ethane, as characterised by the time constant T_2 . Nuclear spin relaxation processes exhibit well-defined relationships with the translational and rotational dynamics of spin-bearing molecules. For unrestricted (bulk) gases such relaxation processes are dominated by the so-called spin-rotation relaxation mechanism (Hubbard, 1963; Singer et al., 2018; Zhang et al., 2002), while dipolar relaxation processes dominate within the condensed phase (Kowalewski & Mäler, 2017), including molecular layers formed upon adsorption (Song & Kausik, 2019). For short-chain hydrocarbon fluids confined to mesoporous materials, the observed relaxation characteristics are dominated by rapid exchange across the pore structure, described as a weighted averaged of contributions from both adsorbed species at the solid/fluid interface and bulk-like fluid towards the centre of the pores. The resulting relaxation rates may be expressed as (Song, 2013)

$$\frac{1}{T_2} = \frac{1-P}{T_{2,bulk}} + \frac{P}{T_{2,ads}}. \quad (4.2)$$

Here, T_2 is the observed relaxation time constant, $T_{2,bulk}$ is the time constant for the unrestricted fluid, while $T_{2,ads}$ is the time constant for species adsorbed at the pore surface. The term P describes the fraction of spins within the adsorbed surface layer, with $1-P$ spins occupying the bulk-like centre of the pore. This term may be further expanded as $P=\lambda S/V$, where S/V describes the accessible surface-to-volume ratio of the confining pore structures, while λ defines the thickness of the adsorbed surface layer. As this length scale is typically small relative to the pore radius, **Equation (4.2)** may be further expressed as (Song & Kausik, 2019)

$$\frac{1}{T_2} \approx \frac{1}{T_{2,bulk}} + \rho_2 \frac{S}{V}, \quad (4.3)$$

where $\rho_2=\lambda/T_{2,surf}$ defines the transverse surface relaxivity; given the general case that $T_{2,bulk}>T_{2,ads}$, this term then provides an approximate scaling factor between observed relaxation characteristics and pore size.

The self-diffusion characteristics of confined hydrocarbons are also perturbed through repeated interactions with the pore walls of the adsorbing solid, reducing the bulk self-diffusion coefficient D_0 to an effective self-diffusion coefficient D_{eff} . The relationship between D_0 and D_{eff} is strongly dependent on both the structure of the confining pore network and the observation period employed, with differing degrees of observed diffusive restriction characterized by the parameter (Price, 1997)

$$\xi = \frac{D_0 \Delta}{r^2}, \quad (4.4)$$

where Δ is the observation period and r is the pore radius. Short-, intermediate- and long-time diffusion limits are characterized by ξ values $\ll 1$, ~ 1 and $\gg 1$, respectively, and are described in detail elsewhere (for example Price, 1997). Here we focus on diffusive characteristics which obey the long-time diffusion limit, where the effective self-diffusion coefficient D_{eff} is reduced from that of the unrestricted fluid according to (Price, 2009)

$$D_{\text{eff}} = \frac{D_0}{\tau}, \quad (4.5)$$

with τ representing the pore network tortuosity.

4.4 Experimental section

4.4.1 Materials

Mesoporous CARiACT Q-series silica gel materials were obtained from Fuji Silysia Chemical Ltd (Japan). The silicas comprised spherical particles ranging in diameter between approximately 2 μm and 5 μm and exhibited nominal mean pore diameters of 6, 15 and 50 nm; these materials are referred to as Q6, Q15 and Q50, respectively. Ethane (purity > 99.99 %) was obtained from Coregas (Australia).

4.4.2 Material Characterization

Silica pore size distributions, together with specific surface area and cumulation pore volume values, were measured via the acquisition of nitrogen isotherm data at 77 K using a Micromeritics ASAP 2020 adsorption analyser. Prior to each measurement approximately 0.5

g of each material was heated for 10 hours at 200 °C under vacuum to remove any physisorbed water. Barrett-Joyner-Halenda (BJH) pore size distributions were obtained from the desorption branch of each isotherm and are detailed in **Figure 4.1**, while Brunauer-Emmett-Teller (BET) surface areas were calculated from each adsorption branch within the relative pressure range 0.05 – 0.35. **Table 4.1** provides a summary of the textural properties of the Q-series silica gels.

Table 4.1. Material textural properties of mesoporous CARiACT Q6, Q15 and Q50 silicas.

| | Q6 | Q15 | Q50 |
|--|--------------------|--------------------|--------------------|
| Modal pore diameter / nm | 6.0 | 14.9 | 52.6 |
| Specific surface area / m ² g ⁻¹ | 386 | 206 | 72 |
| Cumulative mesopore volume / cm ³ g ⁻¹ | 0.54 | 0.90 | 0.91 |
| Surface are-to-volume ratio / m ⁻¹ | 7.15×10^8 | 2.29×10^8 | 7.91×10^7 |

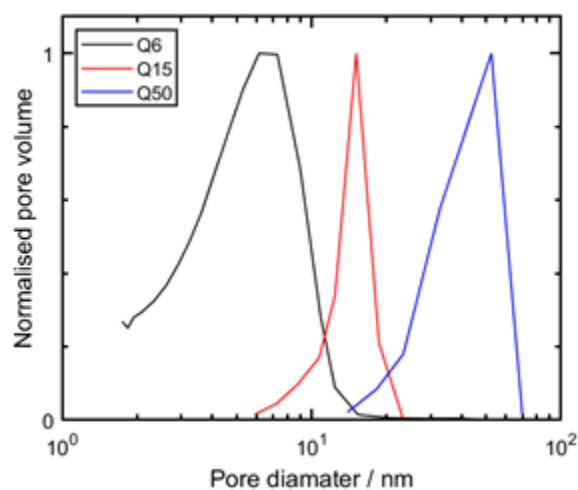


Figure 4.1. BJH pore size distributions of mesoporous CARiACT Q6, Q15 and Q50 silicas.

4.4.3 NMR measurements

Ethane NMR measurements were performed using an Oxford Instruments Geospec spectrometer equipped with a 0.3 T parallel plate magnet array (corresponding to a ¹H NMR frequency of $\nu_0 = 12.7$ MHz) and high pressure P5 overburden cell (Green Imagine Technologies). A schematic of the experimental setup used here is shown in **Figure 4.2**. A cylindrical PEEK (polyether ether ketone) cell (inner diameter = 18 mm, outer diameter = 25 mm, length = 45 mm) was used to hold the silica particles and was wrapped with a FEP heat

shrink tubing to secure the holder between two PEEK gas distribution plugs. Two syringe pumps (Teledyne ISCO 260D) were employed in constant pressure mode to apply both ethane and a ^1H NMR-silent fluorinated confining oil (Fluorinert FC-40) to the system; the latter was set to provide a 50 bar differential pressure above the sample pressure so as to seal the sample cell in place. A vacuum pump (Agilent Technologies DS-102) was used to degas the silica materials and associated experimental apparatus for at least 12 hours before pressurisation with ethane. Pressures were then monitored and recorded using two pressure transducers (Swagelok S model), while pump volume and flow rate data were monitored using LabView (National Instruments Cooperation, USA). Fluid temperatures within the magnet bore were maintained at 23.6 ± 0.2 °C via integration of the syringe pumps with a heated water bath, with the system temperature monitored and recorded via a calibrated temperature sensor.

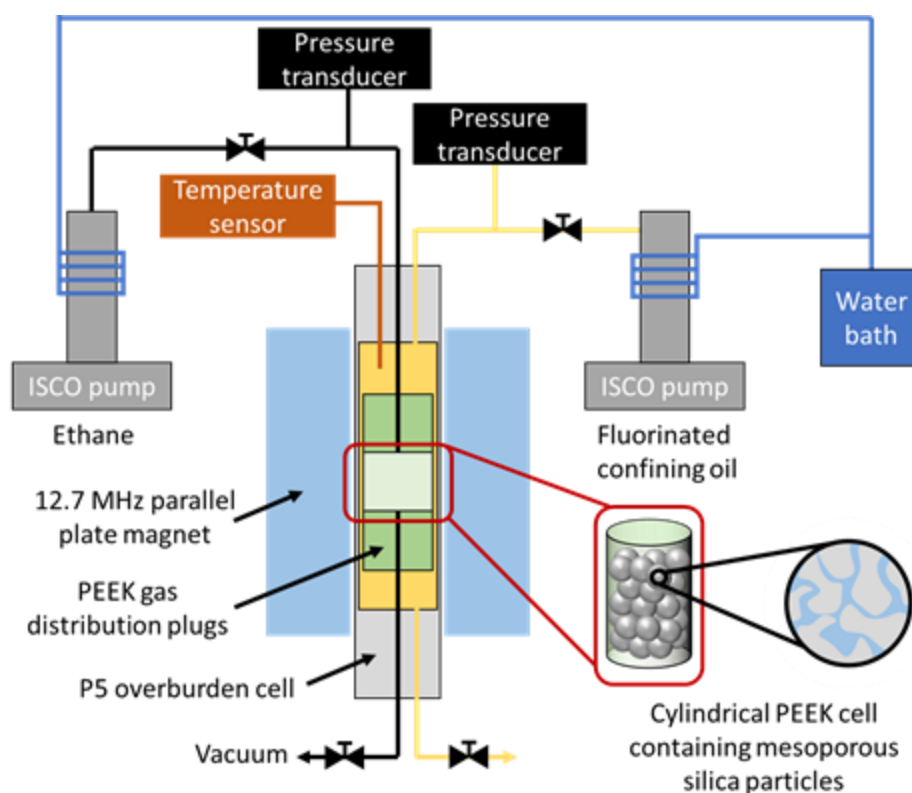


Figure 4.2. Schematic of the experimental apparatus employed to perform NMR measurements.

Prior to our NMR analysis each silica material was dried in air at 120 °C for at least eight hours. Transverse relaxation data were acquired by applying the standard CPMG (Carr-Purcell-Meiboom-Gill) pulse sequence shown in **Figure 4.3(a)** (Carr & Purcell, 1954; Meiboom & Gill, 1958). Following initial polarisation along the direction of the static magnetic

field (conventionally the z -direction) a 90° radio frequency (RF) pulse excites the spin system into the xy -plane, where it undergoes transverse relaxation. A series of n 180° refocussing RF pulses are then applied to counter dephasing due to inhomogeneities within the static field, inducing a train of n spin echoes which decay according to T_2 . Each spin echo magnitude $S(nT_E)$ was recorded as a single data point (white data point within **Figure 4.3(a)**). In this work the echo time was set to $T_E=250$ μs while up to $n=40,000$ echoes were acquired to ensure the CPMG data decayed to the noise floor.

Diffusion data were acquired by applying the pulsed gradient stimulated echo (PGSTE) sequence shown in **Figure 4.3(b)** (Stejskal & Tanner, 1965a; Tanner, 1970). Here, once excited in the xy -plane by a 90° RF pulse, a magnetic field gradient pulse of strength g and length δ imparts a spatially dependent phase across the spin system, encoding the initial positions of the nuclear spin ensemble. A second 90° pulse returns the spin system to the longitudinal axis for a storage time of length T , during which a homospoil gradient is applied to remove any remaining coherent transverse magnetisation. A third 90° pulse returns the system to the xy -plane; here, a second gradient pulse of equal area $g\delta$ is applied to decode the positions of the nuclear spin ensemble, inducing a stimulated echo of magnitude $S(g)$ which attenuates as a function of increasing molecular displacement during the observation period (inter-gradient spacing) $\Delta=T+\tau$. Our PGSTE measurements were performed holding the gradient pulse length $\delta=1.5$ ms and inter-gradient pulse duration $\Delta=30$ ms constant while varying the gradient strength across 16 linearly spaced values up to a maximum of $g = 0.25$ T m^{-1} . The inter-90 spacing was $\tau=5$ ms, while the homospoil gradient was set to 7.65×10^{-4} T m^{-1} and was applied for 1 ms. A total of 4 repeat scans were employed for both CPMG and PGSTE measurements and were separated by a recycle delay of 60 s, providing signal-to-noise ratios >200 .

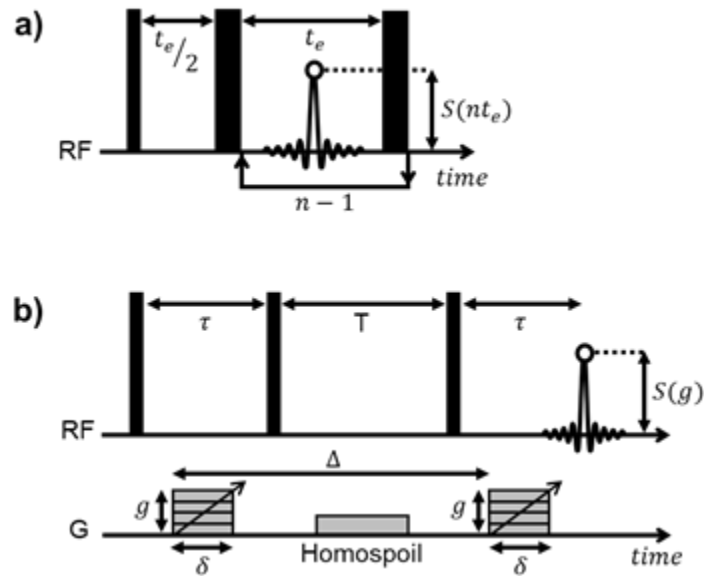


Figure 4.3. NMR radio frequency (RF) pulse sequence diagram for (a) CPMG measurements and (b) PGSTE measurements. Thick and thin bars represent 180° and 90° RF pulses, respectively, while white data points indicate the recorded echo magnitudes. In (b) gradient pulse timings (G axis) are given according to the notation of Tanner (Tanner, 1970).

Approximately 5 g of each silica material was employed, with background T_2 measurements performed under vacuum and subtracted from the subsequently acquired ethane data during processing; such background relaxation signals are primarily associated with O-rings within the high-pressure P5 overburden cell. To minimise the influence of gas/liquid phase changes on the acquired data, all experiments were conducted after suitably long equilibration times (approximately 120 minutes) following pressure alterations, such that a constant zero ethane pump flow rate, together with constant NMR signal magnitudes, were recorded.

Supplementary NMR relaxation measurements were also performed on water saturated silica samples. Each silica material was again dried in air at 120°C for at least eight hours, then saturated with deionised water (obtained onsite at the Australian Resources Research Centre, Perth, Australia) for at least 48 hours before use. Measurements were again performed using a 12.7 MHz Oxford Geospec spectrometer, in this case equipped with a 53 mm Q-sense probe. Saturated silica materials were placed within a 7 ml glass vial at the centre of the magnet bore, with the height of the interparticle water set to cover the top-most silica spheres within the sample.

4.4.4 NMR Data Processing

Acquired T_2 data may be described by the Fredholm integral equation (Wilson, 1992)

$$\frac{S(nT_E)}{S(0)} = \int \exp\left(\frac{-nT_E}{T_2}\right) F(T_2) d \log_{10}(T_2) + \varepsilon(nT_E). \quad (4.6)$$

Here $S(nT_E)/S(0)$ is the normalised NMR spin echo signal intensity and $\varepsilon(nT_E)$ represents the experimental noise, assumed Gaussian with zero mean; $F(T_2)$ is the targeted distribution of T_2 relaxation times and was acquired via numerical inversion of the acquired CPMG data according to **Equation (4.6)**. Acquired diffusion data is similarly described by the expression (Stejskal & Tanner, 1965; Wilson, 1992)

$$\frac{S(g)}{S(0)} = \int \exp\left(-\gamma^2 g^2 \delta^2 \left\{\Delta - \frac{\delta}{3}\right\} D\right) F(D) d \log_{10}(D) + \varepsilon(g). \quad (4.7)$$

Here $S(g)/S(0)$ is the normalised NMR stimulated echo signal intensity, γ is the gyromagnetic ratio of the ^1H nucleus, and $\varepsilon(g)$ is the experimental noise; $F(D)$ is the targeted distribution of diffusion coefficient values and was acquired via numerical inversion of the acquired PGSTE data according to **Equation (4.7)**. Stability of the inverted relaxation and diffusion distributions was enforced via the application of Tikhonov regularisation (Tikhonov & Arsenin, 1977), with the magnitude of the smoothing parameter chosen according to the generalised cross-validation method (Golub et al., 1979). The inversion algorithm was written in MATLAB (MathWorks Inc.) and first used by Griffith *et al.* (Griffith et al., 2007) and Hollingsworth *et al.* (Hollingsworth & Johns, 2003) for relaxation and diffusion analysis, respectively.

4.4.5 Gravimetric Adsorption Measurements

Ethane adsorption measurements were performed under identical pressure and temperature conditions as the above NMR measurements using a gravimetric sorption analyser (Rubotherm, Germany; now TA instruments, USA). A schematic of the experimental setup is shown in **Figure 4.4**. The measurement cell temperature was detected using a calibrated 100 Ω platinum resistance thermometer, with the thermometer resistance measured using a digital multimeter (Millik Precision Thermometer, Isotech, UK). The cell pressure was measured with

a vibrating quartz-crystal-type transmitter (Paroscientific, USA) with a range up to 41.3 MPa. The mass of the porous samples was conducted using an analytical balance via a magnetic suspension coupling; the net adsorbed mass m_{net} on the adsorbent sample is given as (Kleinrahm et al., 2019; Yang et al., 2020)

$$m_{net} = m_{fluid}^* - m_{vac}^* + \rho_{fluid}V_c. \quad (4.8)$$

Here, $m_{fluid}^* = (W_1 - W_0)_{fluid} / \alpha$ and, $m_{vac}^* = (W_1 - W_0)_{vac} / \alpha$ where W_0 and W_1 are the readings of the magnetic suspension balance at the zero position and measurement position, respectively, $\alpha = (1 - \rho_{air} / \rho_{calib})^{-1} \approx 1.000150$ is the balance calibration factor, with ρ_{air} and ρ_{calib} representing the densities of air in the laboratory and the calibration mass, respectively, while the subscripts “vac” and “fluid” denote that the measurements are conducted with the measurement cell both evacuated and filled with ethane, respectively. In **Equation (4.8)**, ρ_{fluid} is the density of the fluid, which is calculated using reference equations of state using the measured temperature and pressure, while V_c is the volume of the sample container. For a non-adsorbing fluid (e.g. helium) the volume of the sample skeleton V_s may be calculated according to

$$V_s = -m_{net} / \rho_{fluid}. \quad (4.9)$$

In practice, however, V_s is regressed as the slope of multiple (ρ_{fluid}, m_{net}) measurements along an isotherm. The excess adsorbed mass m_{ex} is then calculated according to

$$m_{ex} = m_{net} + \rho_{fluid}V_s, \quad (4.10)$$

with the corresponding adsorption capacity expressed as

$$q_{ex} = \frac{(m_{ex} / M_{fluid})}{m_s}, \quad (4.11)$$

where M_{fluid} and m_s are the molar mass of the adsorbate investigated and the mass of the adsorbent, respectively.

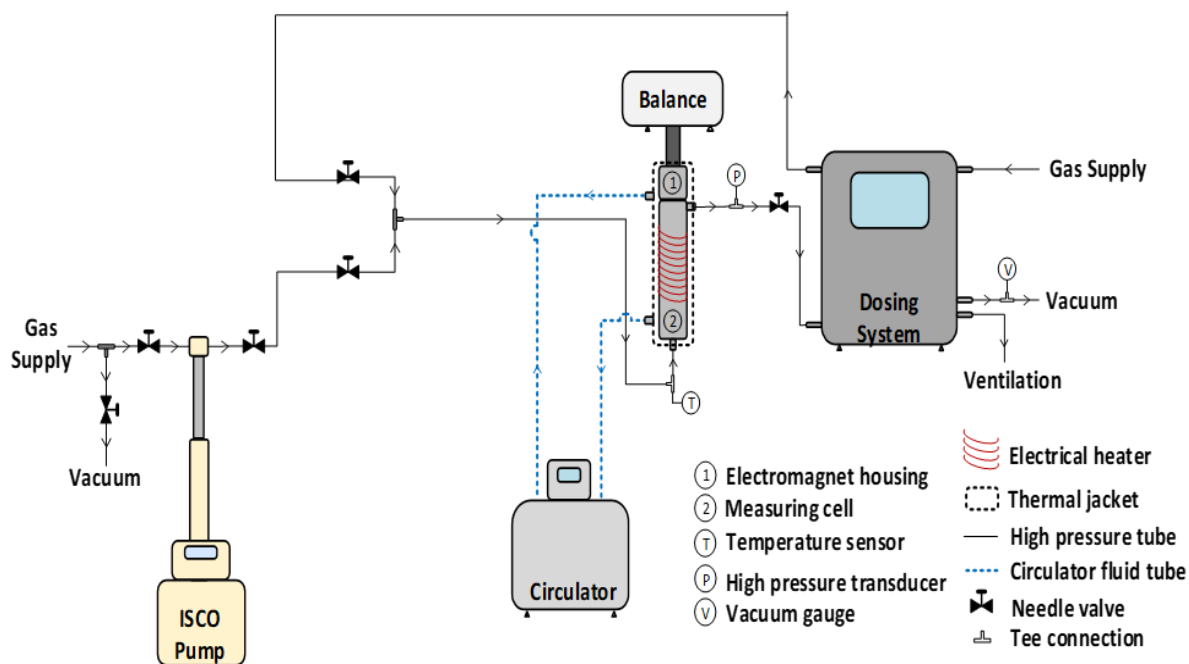


Figure 4.4. Schematic of the experimental apparatus used for gravimetric adsorption measurements.

4.5 Results and Discussion

4.5.1 Bulk Ethane Measurements

NMR relaxation measurements were first conducted on bulk ethane in the absence of any adsorbents. The signal acquired from the first echo of the acquired CPMG echo train was acquired as a close approximation to NMR signal in the absence of relaxation, and is considered here to represent the total ^1H density (and hence ethane density) within the NMR measurement system. **Figure 4.5(a)** shows a direct correlation between the evolution of this acquired signal magnitude across the range 30 – 45 bar with bulk ethane saturation pressure data from the National Institute of Standards and Technology (NIST) Chemistry Web book (Lemmon et al., 2018). A strong linear correlation is apparent, demonstrating the sensitivity of our NMR analysis to increasing ethane density; a simple linear fit (dashed line within **Figure 4.5(a)**; $R^2 > 0.999$) then provides a scaling factor between acquired NMR signal magnitudes and the ethane content of our measurement system. **Figure 4.5(b)** further illustrates the evolution of ethane density as a function of pressure as provided by NIST (Lemmon et al., 2018) and by our calibrated NMR signal data. Excellent agreement in observed data behaviour is readily apparent, providing validation of our experimental NMR method. Our acquired NMR signal

increases gradually for ethane pressures up to 40.8 bar due to increasing molecular density within the gas phase. A steep signal increase between 40.1 bar and 40.8 bar then indicates the onset of bulk ethane condensation, which occurs in close agreement with the expected bulk saturation pressure of 40.68 bar at 23.6 °C (as obtained from the NIST database) (Lemmon et al., 2018).

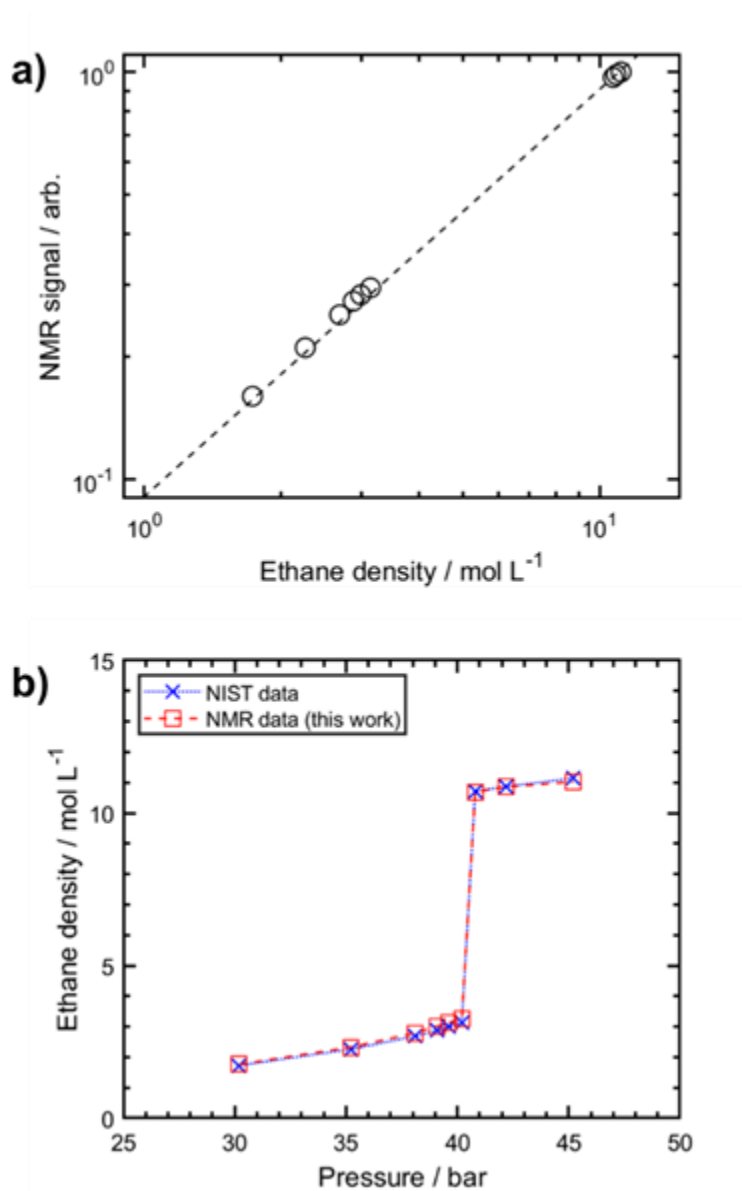


Figure 4.5. (a) Direct correlation of bulk ethane saturation pressure data (obtained from NIST) with measured NMR signal magnitudes. (b) Ethane density evolution as a function of pressure.

4.5.2 Initial Material Characterization

Preliminary T_2 relaxation measurements were performed on water saturated packed beds of each silica material; water provides a ubiquitous and easy to handle high proton density probe fluid which facilitates robust low-field NMR porosity and relaxation analysis under ambient conditions. **Figure 4.6** shows the resultant T_2 distributions, with each data set clearly exhibiting two separated T_2 populations. Following **Equation (4.3)** we may readily assign the populations at short T_2 to water confined within the silica mesopores, while the population at $T_2 \approx 2$ s is indicative of unrestricted water in the interparticle spaces; the small peak located at $T_2 \approx 0.9$ s is assigned to a small water population which exchanges between these environments on the time scale of the T_2 measurement.

Taking the Q6 material, wherein the very large S/V ratio (**Table 4.1**) of the silica makes the assumption $1-P/T_{2,\text{bulk}} \ll P/T_{2,\text{surf}}$ most valid, a simple rearrangement of **Equation (4.3)** into the form

$$\rho_2 \approx \frac{V}{S} \frac{1}{T_2}, \quad (4.12)$$

combined with the assumption of spherical pores of diameter $d = 6V/S$, gives $\rho_2 \approx 0.125 \mu\text{m s}^{-1}$. This value is consistent with transverse surface relaxivity values obtained from high-purity colloiddally-templated silicas in the absence of appreciable paramagnetic surface impurities ($\rho_2 = 0.122 - 0.203 \mu\text{m s}^{-1}$) (Krzyżak & Habina, 2016), in turn implying that surface-enhanced nuclear spin relaxation occurs within these materials as a result of reduced molecular mobility upon adsorption rather than via interactions within surface-bound paramagnetic species (Gladden & Mitchell, 2011).

Total porosity values for these packed beds were obtained by comparing the acquired NMR signal magnitude to that from a known volume of water; these values are given in **Table 4.2** and are assumed relevant to the packed silica beds employed in our ethane measurements. **Table 4.2** further provides the percentage intra-porosity found within the silica mesopores and the inter-porosity within the interparticle spaces; these values are obtained by integrating the two T_2 populations shown in **Figure 4.6**, where we assume the contribution of the exchange peak is negligible.

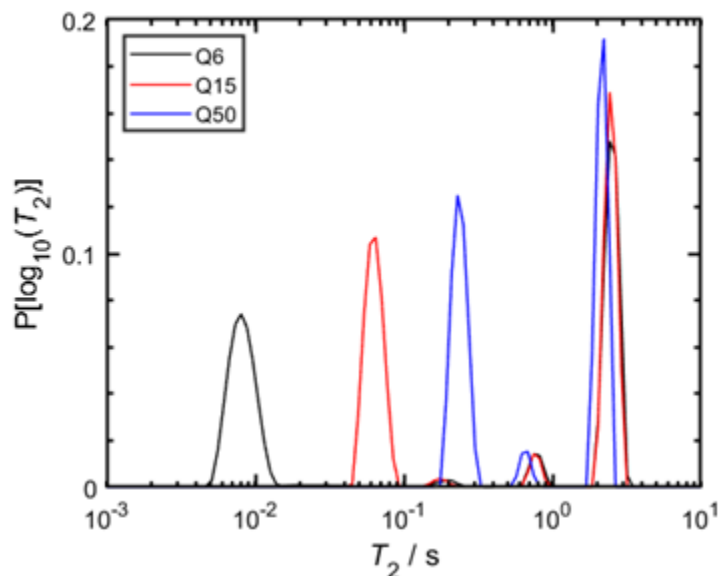


Figure 4.6. T_2 relaxation distributions obtained from water saturated packed beds of mesoporous Q -silicas.

Table 4.2. Silica bed porosity data obtained from NMR measurements of water saturated samples. Intraparticle and interparticle porosity values represent the percentage of the total porosity found within the intraparticle mesopores and interparticle spaces, respectively.

| | Total porosity (ϕ) | Intra-porosity / % | Inter-porosity / % |
|-----|---------------------------|--------------------|--------------------|
| Q6 | 0.73 | 47 | 53 |
| Q15 | 0.82 | 48 | 52 |
| Q50 | 0.82 | 46 | 54 |

4.5.3 NMR Ethane Adsorption Measurements

In analogy to our measurements of bulk ethane, the NMR signal associated with ethane in the presence of mesoporous silicas was approximated from the magnitude of the first echo of each acquired CPMG echo train. **Figure 4.7** reports the NMR-observed ethane content of our systems as a function of pressure, providing a comparison between bulk ethane and the ethane density in the cell when in the presence of our three mesoporous adsorbates. A clear step-change in ethane density is observed for all systems, again indicating ethane condensation at increased pressures. In systems containing the three mesoporous silicas this increase is observed within the pressure range 39 – 40 bar; these pressures are marginally lower than the

condensation pressure observed for bulk ethane (40.1 – 40.8 bar), initially suggesting that capillary condensation processes may occur within the mesoporous structures of the silica particles, while bulk-like condensation is expected within the interparticle voids. However, fully reversible isotherms are observed across all three silica materials, which are not expected in the case of capillary condensation (Barsotti et al., 2020); a possible explanation for the lack of observed hysteresis is as follows. Capillary condensation processes are expected to occur first within the smallest pore spaces present (pore throats) during the adsorption process. During desorption, these regions remain blocked as the liquid within these regions is the last to evaporate, leading to delayed desorption and hence hysteresis. However, the width of the resultant hysteresis loop is known to shrink with increasing temperature (and hence decreasing fluid surface tension) until the overlap of adsorption and desorption branches occurs at a critical temperature (Barsotti et al., 2018). In the present work the experimental temperature employed (23.6 °C) is close to the critical temperature of ethane (32.18 °C) due to the limited working environment of our NMR equipment. Simple calculations utilising the Kelvin equation shown in **Equation (4.1)** reveal estimates of the anticipated ethane capillary condensation pressures in this study to be in the range 40.34 – 41.32 bar, 40.54 – 40.93 bar and 40.64 – 40.75 bar for the Q6, Q15 and Q50 materials, respectively, which take into account a spectrum of surface wetting behaviours. These narrow ranges incorporate the bulk saturated pressure of 40.68 bar at our experimental temperature, indicating that the detection of capillary condensation processes within our system is unlikely.

Figure 4.7 illustrates that at conditions where the bulk liquid is stable, the ethane density is greater than at the corresponding conditions in the systems containing porous silica; this observation is consistent with the occupation of cell space by the solid silica matrix. The near identical ethane density values observed within the Q15 and Q50 beds under liquid ethane conditions are consistent with the NMR porosity values detailed within **Table 4.2**, wherein the two beds are characterized by porosities of approximately 82 %. The clear decrease in ethane density within the Q6 bed, relative to the Q15 and Q50 systems, is further consistent with the porosity data in **Table 4.2**, which shows that the Q6 system exhibits a reduced porosity of 73 %. Under gas phase conditions the ethane density within the Q6 and Q15 systems is noticeably larger than is measured for the Q50 or bulk ethane systems, which we attribute to a consequence of significant adsorption within these high surface area-to-volume ratio materials. As adsorption will also occur within the Q50 system we propose that the overlap of Q50 and bulk

ethane density data at low pressures results from the cancellation of adsorption phenomena by the excluded volume of the solid matrix.

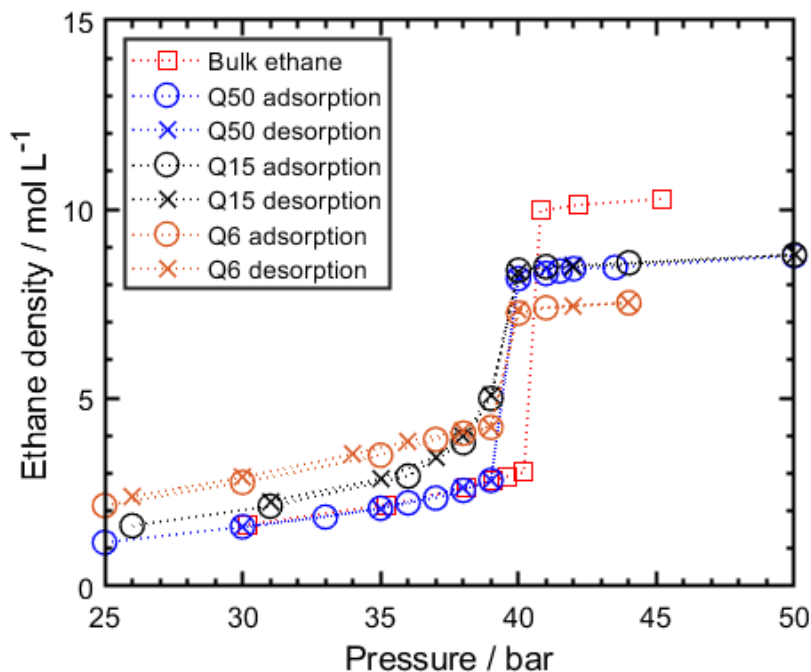


Figure 4.7. Calibrated NMR isotherms of ethane in the mesoporous silicas Q6, Q15 and Q50, as compared to the bulk. Fully reversible isotherms are seen across all silica materials.

To further probe the capacity of our NMR measurements to probe ethane adsorption phenomena, we show in **Figure 4.8** a direct comparison of our NMR data with gravimetric adsorption measurements, performed under identical conditions; these data are limited to the pressure range of (25 to 39) bar to avoid the liquefaction phenomena demonstrated in **Figure 4.7**. For each data set shown in **Figure 4.8**, the excess NMR signal attributed to adsorption S_{ads} was calculated according to

$$S_{ads} = S_{exp} - S_{calc}. \quad (4.13)$$

Here S_{exp} is the experimentally measured NMR signal acquired for each mesoporous silica system at each pressure, while S_{calc} is the anticipated signal arising from the contribution of purely bulk ethane at each of these pressures, calculated according to

$$S_{calc} = \frac{\rho V \phi}{\alpha}. \quad (4.14)$$

Here ρ is the pressure-dependent bulk ethane density obtained from the NIST database (Lemmon et al., 2018), V is the volume of the PEEK cell employed in the NMR measurements, ϕ is the total porosity of each silica packed bed given in **Table 4.2**, and α is the scaling factor between ethane quantity and NMR signal established in **Figure 4.5(a)**. The adsorption excess is then calculated as

$$q_{ex} = \frac{\alpha S_{ads}}{m_s}, \quad (4.15)$$

where m_s is the mass of mesoporous silica employed in each measurement.

Excellent agreement is apparent between our NMR and gravimetric adsorption data across both the Q6 and Q50 silica materials, with a maximum deviation of less than 0.2 mmol g^{-1} (approximately 5% of the observed ethane capacity) between the two measurements. Comparable agreement is also observed in the case of Q15 up to pressures of approximately 36 bar, beyond which the two data series diverge. While the source of this discrepancy is the subject of further investigation, the data within **Figure 4.8** provide a clear demonstration that low-field NMR analysis may be exploited to obtain quantitative hydrocarbon adsorption data from the interaction of mesoporous sorbents and gas phase hydrocarbons. The general trend of increasing adsorption capacity in the order Q6 > Q15 > Q50 is readily rationalised based on the surface-to-volume ratios of these materials (**Table 4.1**), with the largest such ratio corresponding to the greatest mass-based adsorption capacity in the presence of gaseous ethane.

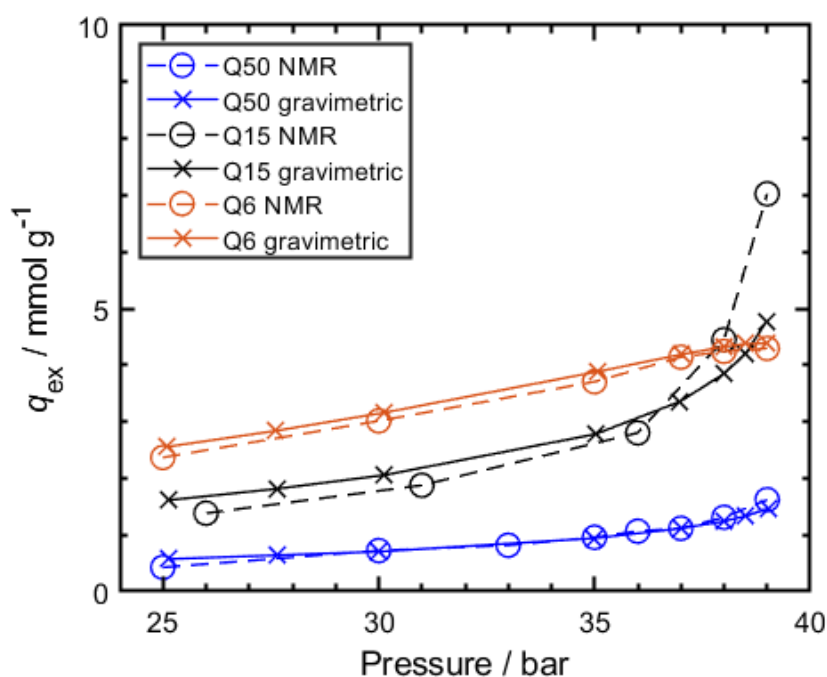


Figure 4.8. Direct comparison of the excess gas phase ethane adsorption capacities q_{ex} obtained via NMR and gravimetric measurements at pressures between 25 bar and 39 bar.

To demonstrate the capacity of NMR relaxation measurements for probing ethane adsorption phenomena, we show in **Figure 4.9(a)** an example series of T_2 distributions, characterizing the pressure dependent relaxation behaviour of ethane within the Q15 silica bed. Two relaxation populations are clearly apparent at each pressure. For the distribution data obtained at pressures in excess of 40 bar these populations are readily assigned to liquid ethane within the intrapore and interpore spaces of the packed bed; in analogy to our preliminary water saturated measurements this assignment is based on the magnitude of the measured T_2 values, with the population exhibiting shorter T_2 values attributed to ethane confined within the intraparticle mesopores of the silica material. Further consistency with our saturated water data is also obtained when considering the integrated signal intensities of each population. For both the 41 bar and 44 bar data sets shown in **Figure 4.9(a)** such integration suggests 56 % of the ethane lies in the interparticle space, while 43 % is confined within the intraparticle mesopores; these values are in good agreement with porosity data shown in **Table 4.2**, which suggest these values to be 53 % and 47 %, respectively.

Assignment of the observed relaxation behaviour below the bulk condensation pressure is more complex. **Figure 4.9(b)** demonstrates the integrated signal intensities of the two observed T_2 populations as a function of pressure; for completeness, we note that this data is sensitive to both ethane within the adsorbed surface layer, as well as ethane away from the pore walls, and is therefore characteristic of the absolute adsorption capacity q_{abs} , rather than the excess quantities discussed above in relation to **Figure 4.7**. While we might expect the associated gas phase T_2 populations to follow the trend exhibited by the liquid phase, with shortened T_2 values indicating more confined species, this is not reciprocated by the integrated signal intensities of these populations. Rather, **Figure 4.9(b)** shows that the integrated population at short T_2 (~ 1 s or below) remains essentially constant as a function of increasing pressure, while the population at longer T_2 shows a clear increase in intensity; we interpret this behaviour as an indication of adsorption. Given the vast majority of ethane adsorption is anticipated to occur with the high surface area-to-volume ratio mesopores of the Q15 silica material, we therefore assign the population at increased T_2 to ethane within the intraparticle Q15 mesopores.

Our unconventional T_2 population assignment is supported via supplementary diffusion data presented in **Figure 4.9(c)**, which illustrates distributions of the observed ethane diffusion coefficients. Two separate diffusive populations are apparent at pressures below the bulk ethane condensation pressure; a rapidly diffusing population characterized by an essentially pressure invariant diffusion coefficient of $D \approx 2 \times 10^{-7} \text{ m}^2 \text{ s}^{-1}$, together with a slower diffusing population with $D < 1 \times 10^{-7} \text{ m}^2 \text{ s}^{-1}$. Following **Equation (4.5)** we may readily assign the signal population with the slowest diffusion coefficient to ethane within the intraparticle mesopore network, wherein repeated encounters with the pore walls facilitate the observation of effective self-diffusion, the rate of which is reduced from that of the unrestricted bulk fluid by the tortuosity of the mesopore network. In contrast, the more rapid diffusion coefficient is in fair agreement with the diffusive behaviour of bulk ethane (observed to be between $2.5 \times 10^{-7} \text{ m}^2 \text{ s}^{-1}$ and $1.5 \times 10^{-7} \text{ m}^2 \text{ s}^{-1}$ at 23.6 °C and pressures between 30 bar and 39 bar) and is therefore assigned to ethane within the large interparticle spaces. The integrated populations of these two components are shown in **Figure 4.9(d)**, where a clear and significant increase in the population of the slower diffusing environment is evident with increasing pressure; we again interpret this increase as an indication of adsorption phenomena. A direct correlation between the relaxation and diffusion populations attributed to ethane within the intraparticle mesopores is provided in **Figure 4.9(e)**, revealing clear consistency between the two data sets, and providing validation for our peak assignments within **Figure 4.9(a)**.

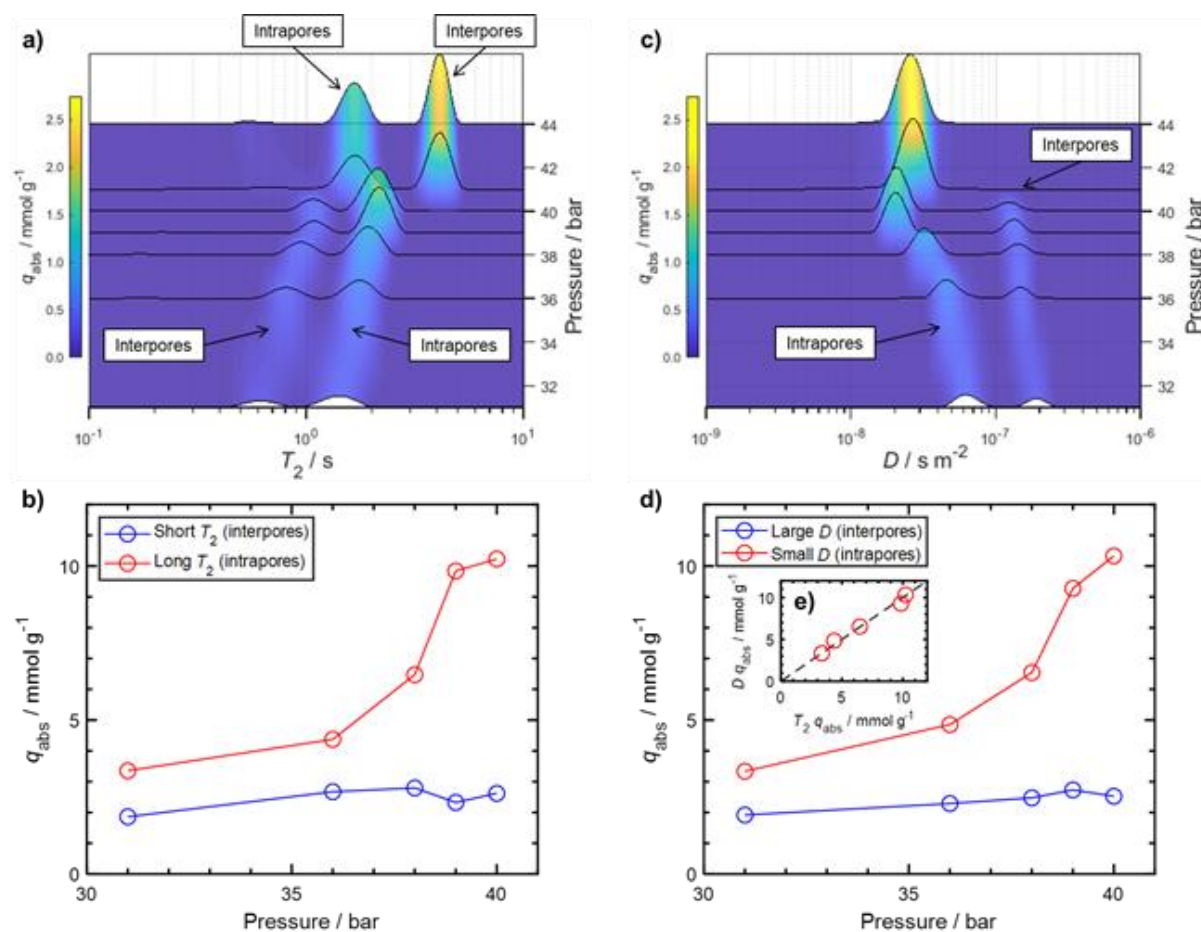


Figure 4.9. (a) T_2 distributions acquired from ethane in a packed bed of Q15 silica as a function of pressure between 31 bar and 44 bar. (b) Integrated NMR signal intensities for the two T_2 populations present within the gas phase (pressure < 40 bar). (c) Diffusion distributions for ethane in Q15 silica within the same pressure range. (d) Integrated NMR signal intensities for components in diffusion distributions. (e) Direct comparison between relaxation and diffusion derived absolute intraparticle gas phase ethane capacities, demonstrating excellent agreement.

The observation of rapid T_2 relaxation phenomena within the interparticle spaces of the Q15 packed bed may be rationalised based on the large diffusive distances that bulk-like ethane will cover during our NMR relaxation measurements. Detailed modelling has elucidated the occurrence of multiple magnetisation environments within the large interparticle pores prevalent to packed beds of spherical particles (Mitchell & Fordham, 2019). The somewhat exotic local magnetisation behaviour of such interparticle pore systems is attributed to differences in magnetic susceptibility between the solid and fluid materials under investigation (Mitchell et al., 2010). Even under the conditions of the low static magnetic field strength employed here, extensive diffusion of proton bearing species through such varying fields is expected to facilitate an additional source of transverse nuclear spin relaxation, leading to a

reduction in observed T_2 times below that expected from surface interactions alone. The realisation that such phenomena can potentially invert the expected T_2 magnitudes observed from pore structures of substantially different size is significant regarding future materials characterization using hydrocarbon gas relaxation, and highlights the care needed to avoid of erroneous relaxation population assignment within hierarchically porous systems.

4.6 Conclusions

In this work we have explored a series of low-field NMR measurements to examine ethane behaviour within packed beds of mesoporous silica materials exhibiting pore sizes between 6 and 50 nm. This investigation has demonstrated the clear utility of such measurements in obtaining quantitative ethane uptake data at pressures up to the bulk condensation point. Excellent agreement is observed through a direct comparison of NMR calculated excess adsorption capacities and gravimetric adsorption measurements. NMR T_2 relaxation distribution data has further been demonstrated as a facile approach with which to quantify and contrast the absolute adsorption capacities of intraparticle mesopores against interparticle voids, with the assignment of differing relaxation phenomena to ethane within distinctly different pore structures validated through the acquisition and PFG NMR diffusion data. Overall, our results highlight benchtop NMR as a potentially useful tool in the screening of short chain hydrocarbon adsorption phenomena within porous materials of relevance to gas processing and catalytic transformations without the need for specialist sorption hardware.

4.7 References

- Barsotti, E., Tan, S. P., Piri, M., & Chen, J. H. (2018). Phenomenological Study of Confined Criticality: Insights from the Capillary Condensation of Propane, n -Butane, and n -Pentane in Nanopores. *Langmuir*, *34*(15), 4473–4483. <https://doi.org/10.1021/acs.langmuir.8b00125>
- Barsotti, E., Tan, S. P., Piri, M., & Chen, J. H. (2020). Capillary-condensation hysteresis in naturally-occurring nanoporous media. *Fuel*, *263*, 116441. <https://doi.org/10.1016/j.fuel.2019.116441>
- Berggren, A., Palmqvist, A. E. C., & Holmberg, K. (2005). Surfactant-templated mesostructured materials from inorganic silica. *Soft Matter*, *1*(3), 219–226. <https://doi.org/10.1039/B507551N>
- Blümich, B. (2019). Low-field and benchtop NMR. *Journal of Magnetic Resonance*, *306*, 27–35. <https://doi.org/10.1016/j.jmr.2019.07.030>

- Bücker, D., & Wagner, W. (2006). A Reference Equation of State for the Thermodynamic Properties of Ethane for Temperatures from the Melting Line to 675 K and Pressures up to 900 MPa. *Journal of Physical and Chemical Reference Data*, 35(1), 205. <https://doi.org/10.1063/1.1859286>
- Carr, H. Y., & Purcell, E. M. (1954). Effects of Diffusion on Free Precession in Nuclear Magnetic Resonance Experiments. *Physical Review*, 94(3), 630–638. <https://doi.org/10.1103/PhysRev.94.630>
- Chen, J. J., Kong, X., Sumida, K., Manumpil, M. A., Long, J. R., & Reimer, J. A. (2013). ExSitu NMR relaxometry of metal-organic frameworks for rapid surface-area screening. *Angewandte Chemie - International Edition*, 52(46), 12043–12046. <https://doi.org/10.1002/anie.201305247>
- Chen, J. J., Mason, J. A., Bloch, E. D., Gygi, D., Long, J. R., & Reimer, J. A. (2015). NMR relaxation and exchange in metal–organic frameworks for surface area screening. *Microporous and Mesoporous Materials*, 205, 65–69. <https://doi.org/10.1016/J.MICROMESO.2014.07.037>
- Chiang, W. S., Fratini, E., Baglioni, P., Chen, J. H., & Liu, Y. (2016). Pore Size Effect on Methane Adsorption in Mesoporous Silica Materials Studied by Small-Angle Neutron Scattering. *Langmuir*, 32(35), 8849–8857. <https://doi.org/10.1021/ACS.LANGMUIR.6B02291>
- Cybula, A., Klein, M., & Zaleska, A. (2015). Methane formation over TiO₂-based photocatalysts: Reaction pathways. *Applied Catalysis B: Environmental*, 164, 433–442. <https://doi.org/10.1016/J.APCATB.2014.09.038>
- D'Agostino, C., Mitchell, J., Gladden, L. F., & Mantle, M. D. (2012). Hydrogen Bonding Network Disruption in Mesoporous Catalyst Supports Probed by PFG-NMR Diffusometry and NMR Relaxometry. *The Journal of Physical Chemistry C*, 116(16), 8975–8982. <https://doi.org/10.1021/jp2123295>
- D'Agostino, C., Mitchell, J., Mantle, M. D., & Gladden, L. F. (2014). Interpretation of NMR Relaxation as a Tool for Characterising the Adsorption Strength of Liquids inside Porous Materials. *Chemistry - A European Journal*, 20(40), 13009–13015. <https://doi.org/10.1002/chem.201403139>
- Davies, S., & Packer, K. J. (1990). Pore-size distributions from nuclear magnetic resonance spin-lattice relaxation measurements of fluid-saturated porous solids. I. Theory and simulation. *Journal of Applied Physics*, 67(6), 3163–3170. <https://doi.org/10.1063/1.345395>
- Duchowny, A., Dupuy, P. M., Widerøe, H. C., Berg, O. J., Faanes, A., Paulsen, A., Thern, H., Mohnke, O., Küppers, M., Blümich, B., & Adams, A. (2021). Versatile high-pressure gas apparatus for benchtop NMR: Design and selected applications. *Journal of Magnetic Resonance*, 329, 107025. <https://doi.org/10.1016/j.jmr.2021.107025>
- Dutta, D., Chatterjee, S., Pillai, K. T., Pujari, P. K., & Ganguly, B. N. (2005). Pore structure of silica gel: a comparative study through BET and PALS. *Chemical Physics*, 312(1–3), 319–324. <https://doi.org/10.1016/J.CHEMPHYS.2004.12.008>
- Dvoyashkin, M., Khokhlov, A., Naumov, S., & Valiullin, R. (2009). Pulsed field gradient NMR study of surface diffusion in mesoporous adsorbents. *Microporous and Mesoporous Materials*, 125(1–2), 58–62. <https://doi.org/10.1016/J.MICROMESO.2008.12.005>

- Fisher, L. R., & Israelachvili, J. N. (1979). Direct experimental verification of the Kelvin equation for capillary condensation. *Nature*, 277(5697), 548–549. <https://doi.org/10.1038/277548a0>
- Gladden, L. F., & Mitchell, J. (2011). Measuring adsorption, diffusion and flow in chemical engineering: applications of magnetic resonance to porous media. *New Journal of Physics*, 13(3), 035001. <https://doi.org/10.1088/1367-2630/13/3/035001>
- Golub, G. H., Heath, M., & Wahba, G. (1979). Generalized cross-validation as a method for choosing a good ridge parameter. *Technometrics*, 21(2), 215–223. <https://doi.org/10.1080/00401706.1979.10489751>
- Griffith, J. D., Bayly, A. E., & Johns, M. L. (2007). Evolving micro-structures in drying detergent pastes quantified using NMR. *Journal of Colloid and Interface Science*, 315(1), 223–229. <https://doi.org/10.1016/j.jcis.2007.06.050>
- Haneda, M., Joubert, E., Me´ne´zo, J.-C., Duprez, D., Barbier, J., Bion, N., Daturi, M., Saussey, J., Lavalley, J.-C., & Hamada, H. (2001). Surface characterization of alumina-supported catalysts prepared by sol–gel method. Part I. Acid–base properties. *Physical Chemistry Chemical Physics*, 3(7), 1366–1370. <https://doi.org/10.1039/b009945g>
- Hollingsworth, K. G., & Johns, M. L. (2003). Measurement of emulsion droplet sizes using PFG NMR and regularization methods. *Journal of Colloid and Interface Science*, 258(2), 383–389. [https://doi.org/10.1016/S0021-9797\(02\)00131-5](https://doi.org/10.1016/S0021-9797(02)00131-5)
- Horch, C., Schlayer, S., & Stallmach, F. (2014). High-pressure low-field ¹H NMR relaxometry in nanoporous materials. *Journal of Magnetic Resonance*, 240, 24–33. <https://doi.org/10.1016/J.JMR.2014.01.002>
- Hu, Y., Li, M., Hou, G., Xu, S., Gong, K., Liu, X., Han, X., Pan, X., & Bao, X. (2017). The role of water in methane adsorption and diffusion within nanoporous silica investigated by hyperpolarized ¹²⁹Xe and ¹H PFG NMR spectroscopy. *Nano Research* 2018 11:1, 11(1), 360–369. <https://doi.org/10.1007/S12274-017-1638-8>
- Hu, Y., Pan, X., Han, X., & Bao, X. (2017). Displacement and Diffusion of Methane and Carbon Dioxide in SBA-15 Studied by NMR. *Journal of Physical Chemistry C*, 121(4), 2481–2486. <https://doi.org/10.1021/ACS.JPCC.6B12250>
- Hu, Y., Zhang, Q., Li, M., Pan, X., Fang, B., Zhuang, W., Han, X., & Bao, X. (2016). Facilitated Diffusion of Methane in Pores with a Higher Aromaticity. *Journal of Physical Chemistry C*, 120(35), 19885–19889. <https://doi.org/10.1021/ACS.JPCC.6B07500>
- Hubbard, P. S. (1963). Theory of Nuclear Magnetic Relaxation by Spin-Rotational Interactions in Liquids. *Physical Review*, 131(3), 1155–1165. <https://doi.org/10.1103/PhysRev.131.1155>
- Hyde, E. D. E. R., Seyfaee, A., Neville, F., & Moreno-Atanasio, R. (2016). Colloidal Silica Particle Synthesis and Future Industrial Manufacturing Pathways: A Review. In *Industrial and Engineering Chemistry Research* (Vol. 55, Issue 33, pp. 8891–8913). American Chemical Society. <https://doi.org/10.1021/acs.iecr.6b01839>
- Isaacs, M. A., Parlett, C. M. A., Robinson, N., Durdell, L. J., Manayil, J. C., Beaumont, S. K., Jiang, S., Hondow, N. S., Lamb, A. C., Jampaiah, D., Johns, M. L., Wilson, K., & Lee, A. F. (2020). A spatially orthogonal hierarchically porous acid–base catalyst for cascade and antagonistic reactions. *Nature Catalysis*, 3(11), 921–931. <https://doi.org/10.1038/s41929->

- Isaacs, M. A., Robinson, N., Barbero, B., Durdell, L. J., Manayil, J. C., Parlett, C. M. A., D'Agostino, C., Wilson, K., & Lee, A. F. (2019). Unravelling mass transport in hierarchically porous catalysts. *Journal of Materials Chemistry A*, 7(19), 11814–11825. <https://doi.org/10.1039/C9TA01867K>
- Johns, M. L., Fridjonsson, E. O., Vogt, S. J., & Haber, A. (2015). *Mobile NMR and MRI: Developments and Applications*. Royal Society of Chemistry.
- Kärger, J., Avramovska, M., Freude, D., Haase, J., Hwang, S., & Valiullin, R. (2021). Pulsed field gradient NMR diffusion measurement in nanoporous materials. *Adsorption*, 27(3), 453–484. <https://doi.org/10.1007/s10450-020-00290-9>
- Kerr, J. D., Balcom, B. J., McCarthy, M. J., & Augustine, M. P. (2019). A low cost, portable NMR probe for high pressure, MR relaxometry. *Journal of Magnetic Resonance*, 304, 35–41. <https://doi.org/10.1016/J.JMR.2019.05.001>
- Kinn, B. E., Myers, T. R., & Allgeier, A. M. (2019). Surface enhanced nuclear magnetic resonance relaxation mechanisms and their significance in chemical engineering applications. *Current Opinion in Chemical Engineering*, 24, 115–121. <https://doi.org/10.1016/J.COCH.2019.03.010>
- Kleinrahm, R., Yang, X., McLinden, M. O., & Richter, M. (2019). Analysis of the systematic force-transmission error of the magnetic-suspension coupling in single-sinker densimeters and commercial gravimetric sorption analyzers. *Adsorption* 25:4, 25(4), 717–735. <https://doi.org/10.1007/S10450-019-00071-Z>
- Kolasinski, K. W. (2020). *Surface Science: Foundations of Catalysis and Nanoscience* (4th ed.). Wiley.
- Kondrashova, D., Lauerer, A., Mehlhorn, D., Jobic, H., Feldhoff, A., Thommes, M., Chakraborty, D., Gommers, C., Zecevic, J., de Jongh, P., Bunde, A., Kärger, J., & Valiullin, R. (2017). Scale-dependent diffusion anisotropy in nanoporous silicon. *Scientific Reports* 2017 7:1, 7(1), 1–10. <https://doi.org/10.1038/srep40207>
- Korb, J. P. (2018). Multiscale nuclear magnetic relaxation dispersion of complex liquids in bulk and confinement. *Progress in Nuclear Magnetic Resonance Spectroscopy*, 104, 12–55. <https://doi.org/10.1016/J.PNMRS.2017.11.001>
- Korb, J. P., Delville, A., Xu, S., Demeulenaere, G., Costa, P., & Jonas, J. (1994). Relative role of surface interactions and topological effects in nuclear magnetic resonance of confined liquids. *The Journal of Chemical Physics*, 101(8), 7074–7081. <https://doi.org/10.1063/1.468333>
- Korb, J. P., Xu, S., & Jonas, J. (1993). Confinement effects on dipolar relaxation by translational dynamics of liquids in porous silica glasses. *The Journal of Chemical Physics*, 98(3), 2411–2422. <https://doi.org/10.1063/1.464169>
- Kowalewski, J., & Mäler, L. (2017). *Nuclear spin relaxation in liquids: theory, experiments, and applications* (2nd ed.). CRC Press.
- Krzyżak, A. T., & Habina, I. (2016). Low field ¹H NMR characterization of mesoporous silica MCM-41 and SBA-15 filled with different amount of water. *Microporous and Mesoporous Materials*, 231, 230–239. <https://doi.org/10.1016/J.MICROMESO.2016.05.032>

- Lemmon, E., McLinden, M., & Friend, D. (2018). *Thermophysical properties of fluid systems*. In P.J. Linstrom, & W.G. Mallard (Eds.), *NIST Chemistry WebBook, NIST Standard Reference Database Number 69*. National Institute of Standards and Technology, Gaithersburg MD, 20899. <https://doi.org/10.18434/T4D303>
- Li, Z., Das, S., Hongmanorom, P., Dewangan, N., Wai, M. H., & Kawi, S. (2018). Silica-based micro- and mesoporous catalysts for dry reforming of methane. *Catalysis Science and Technology*, 8(11), 2763–2778. <https://doi.org/10.1039/c8cy00622a>
- Marreiros, J., de Oliveira-Silva, R., Iacomi, P., Llewellyn, P. L., Ameloot, R., & Sakellariou, D. (2021). Benchtop In Situ Measurement of Full Adsorption Isotherms by NMR. *Journal of the American Chemical Society*, 143(22), 8249–8254. <https://doi.org/10.1021/JACS.1C03716>
- Meiboom, S., & Gill, D. (1958). Modified spin-echo method for measuring nuclear relaxation times. *Review of Scientific Instruments*, 29(8), 688–691. <https://doi.org/10.1063/1.1716296>
- Mitchell, J., Chandrasekera, T. C., Johns, M. L., Gladden, L. F., & Fordham, E. J. (2010). Nuclear magnetic resonance relaxation and diffusion in the presence of internal gradients: The effect of magnetic field strength. *Physical Review E - Statistical, Nonlinear, and Soft Matter Physics*, 81(2). <https://doi.org/10.1103/PhysRevE.81.026101>
- Mitchell, J., & Fordham, E. (2019). Magnetization exchange in a single pore due to diffusion in internal fields: Simulation and experiment. *Physical Review Materials*, 3(5), 055604. <https://doi.org/10.1103/PhysRevMaterials.3.055604>
- Mitchell, J., Gladden, L. F., Chandrasekera, T. C., & Fordham, E. J. (2014). Low-field permanent magnets for industrial process and quality control. *Progress in Nuclear Magnetic Resonance Spectroscopy*, 76, 1–60. <https://doi.org/10.1016/J.PNMRS.2013.09.001>
- Mitchell, J., Griffith, J. D., Collins, J. H. P., Sederman, A. J., Gladden, L. F., & Johns, M. L. (2007). Validation of NMR relaxation exchange time measurements in porous media. *The Journal of Chemical Physics*, 127(23), 234701. <https://doi.org/10.1063/1.2806178>
- Mitropoulos, A. C. (2008). The Kelvin equation. *Journal of Colloid and Interface Science*, 317(2), 643–648. <https://doi.org/10.1016/J.JCIS.2007.10.001>
- Naumov, S., Valiullin, R., Kärger, J., Pitchumani, R., & Coppens, M. O. (2008). Tracing pore connectivity and architecture in nanostructured silica SBA-15. *Microporous and Mesoporous Materials*, 110(1), 37–40. <https://doi.org/10.1016/j.micromeso.2007.08.014>
- Oschatz, M., Hofmann, J. P., van Deelen, T. W., Lamme, W. S., Krans, N. A., Hensen, E. J. M., & de Jong, K. P. (2017). Effects of the Functionalization of the Ordered Mesoporous Carbon Support Surface on Iron Catalysts for the Fischer–Tropsch Synthesis of Lower Olefins. *ChemCatChem*, 9(4), 620–628. <https://doi.org/10.1002/CCTC.201601228>
- Papaoannou, A., & Kausik, R. (2015). Methane Storage in Nanoporous Media as Observed via High-Field NMR Relaxometry. *Physical Review Applied*, 4(2), 024018. <https://doi.org/10.1103/PhysRevApplied.4.024018>
- Price, W. S. (1997). Pulsed-field gradient nuclear magnetic resonance as a tool for studying translational diffusion: Part 1. Basic theory. *Concepts in Magnetic Resonance*, 9(5), 299–336. [https://doi.org/10.1002/\(SICI\)1099-0534\(1997\)9:5<299::AID-CMR2>3.0.CO;2-U](https://doi.org/10.1002/(SICI)1099-0534(1997)9:5<299::AID-CMR2>3.0.CO;2-U)

- Price, W. S. (2009). NMR studies of translational motion. In *NMR Studies of Translational Motion*. Cambridge University Press. <https://doi.org/10.1017/CBO9780511770487>
- Ren, Y., Ma, Z., & Bruce, P. G. (2012). Ordered mesoporous metal oxides: synthesis and applications. *Chemical Society Reviews*, 41(14), 4909–4927. <https://doi.org/10.1039/C2CS35086F>
- Robinson, N., Bräuer, P., York, A., & D’Agostino, C. (2021). Nuclear spin relaxation as a probe of zeolite acidity: a combined NMR and TPD investigation of pyridine in HZSM-5. *Physical Chemistry Chemical Physics*. <https://doi.org/10.1039/d1cp01515j>
- Robinson, N., & D’Agostino, C. (2020). NMR Investigation into the Influence of Surface Interactions on Liquid Diffusion in a Mesoporous Catalyst Support. *Topics in Catalysis*, 63(3–4), 319–327. <https://doi.org/10.1007/s11244-019-01209-7>
- Robinson, N., Robertson, C., Gladden, L. F., Jenkins, S. J., & D’Agostino, C. (2018). Direct Correlation between Adsorption Energetics and Nuclear Spin Relaxation in a Liquid-saturated Catalyst Material. *ChemPhysChem*, 19(19), 2472–2479. <https://doi.org/10.1002/cphc.201800513>
- Robinson, N., Xiao, G., Connolly, P. R. J., Ling, N. N. A., Fridjonsson, E. O., May, E. F., & Johns, M. L. (2020). Low-field NMR relaxation-exchange measurements for the study of gas admission in microporous solids. *Physical Chemistry Chemical Physics*, 22(24), 13689–13697. <https://doi.org/10.1039/d0cp02002h>
- Rottreau, T. J., Parlett, C. M. A., Lee, A. F., & Evans, R. (2017). Diffusion NMR Characterization of Catalytic Silica Supports: A Tortuous Path. *Journal of Physical Chemistry C*, 121(30), 16250–16256. <https://doi.org/10.1021/acs.jpcc.7b02929>
- Rouquerol, J., Rouquerol, F., Llewellyn, P., Maurin, G., & Sing, K. S. W. (2013). Adsorption by Powders and Porous Solids: Principles, Methodology and Applications: Second Edition. In *Adsorption by Powders and Porous Solids: Principles, Methodology and Applications: Second Edition*. Elsevier Inc.
- Saito, M., Aihara, T., Miura, H., & Shishido, T. (2021). Brønsted acid property of alumina-based mixed-oxides-supported tungsten oxide. *Catalysis Today*, 375, 64–69. <https://doi.org/10.1016/J.CATTOD.2020.02.009>
- Silletta, E. V., Franzoni, M. B., Monti, G. A., & Acosta, R. H. (2018). Influence of exchange in NMR pore size/relaxation correlation experiments. *Microporous and Mesoporous Materials*, 269, 17–20. <https://doi.org/10.1016/j.micromeso.2017.10.025>
- Singer, P. M., Asthagiri, D., Chapman, W. G., & Hirasaki, G. J. (2018). NMR spin-rotation relaxation and diffusion of methane. *The Journal of Chemical Physics*, 148(20), 204504. <https://doi.org/10.1063/1.5027097>
- Song, Y. Q. (2013). Magnetic resonance of porous media (MRPM): A perspective. *Journal of Magnetic Resonance*, 229, 12–24. <https://doi.org/10.1016/j.jmr.2012.11.010>
- Song, Y. Q., & Kausik, R. (2019). NMR application in unconventional shale reservoirs – A new porous media research frontier. *Progress in Nuclear Magnetic Resonance Spectroscopy*, 112–113, 17–33. <https://doi.org/10.1016/j.pnmrs.2019.03.002>
- Stallmach, F., Kärger, J., Krause, C., Jeschke, M., & Oberhagemann, U. (2000). Evidence of Anisotropic Self-Diffusion of Guest Molecules in Nanoporous Materials of MCM-41 Type. *Journal of the American Chemical Society*, 122(38), 9237–9242.

<https://doi.org/10.1021/ja001106x>

- Stejskal, E. O., & Tanner, J. E. (1965). Spin diffusion measurements: Spin echoes in the presence of a time-dependent field gradient. *The Journal of Chemical Physics*, *42*(1), 288–292. <https://doi.org/10.1063/1.1695690>
- Tang, Y., McCowan, D., & Song, Y. Q. (2019). A miniaturized spectrometer for NMR relaxometry under extreme conditions. *Scientific Reports*, *9*(1), 11174. <https://doi.org/10.1038/s41598-019-47634-2>
- Tanner, J. E. (1970). Use of the Stimulated Echo in NMR Diffusion Studies. *The Journal of Chemical Physics*, *52*(5), 2523–2526. <https://doi.org/10.1063/1.1673336>
- Terenzi, C., Sederman, A. J., Mantle, M. D., & Gladden, L. F. (2019). Enabling High Spectral Resolution of Liquid Mixtures in Porous Media by Antidiagonal Projections of Two-Dimensional ^1H NMR COSY Spectra. *The Journal of Physical Chemistry Letters*, *10*(19), 5781–5785. <https://doi.org/10.1021/acs.jpcclett.9b02334>
- Thern, H., Horch, C., Stallmach, F., Li, B., Mezzatesta, A., Zhang, H., & Arro, R. (2018). Low-field NMR laboratory measurements of hydrocarbons confined in organic nanoporous media at various pressures. *Microporous and Mesoporous Materials*, *269*, 21–25. <https://doi.org/10.1016/j.micromeso.2017.11.047>
- Thommes, M., Kaneko, K., Neimark, A. V., Olivier, J. P., Rodriguez-Reinoso, F., Rouquerol, J., & Sing, K. S. W. (2015). Physisorption of gases, with special reference to the evaluation of surface area and pore size distribution (IUPAC Technical Report). *Pure and Applied Chemistry*, *87*(9–10), 1051–1069. <https://doi.org/10.1515/pac-2014-1117>
- Thomson, W. (1872). On the Equilibrium of Vapour at a Curved Surface of Liquid. *Proceedings of the Royal Society of Edinburgh*, *7*, 63–68. <https://doi.org/10.1017/S0370164600041729>
- Tikhonov, A. N., & Arsenin, V. I. A. (1977). *Solutions of ill-posed problems*. SIAM.
- Ward-Williams, J., & Gladden, L. F. (2019). Insights into adsorption behaviour of binary liquid mixtures in porous media using fast field cycling NMR. *Magnetic Resonance Imaging*, *56*, 57–62. <https://doi.org/10.1016/j.mri.2018.08.007>
- Ward-Williams, J., Korb, J. P., & Gladden, L. F. (2018). Insights into Functionality-Specific Adsorption Dynamics and Stable Reaction Intermediates Using Fast Field Cycling NMR. *Journal of Physical Chemistry C*, *122*(35), 20271–20278. <https://doi.org/10.1021/acs.jpcc.8b04531>
- Ward-Williams, Jordan, Korb, J.-P., Rozing, L., Sederman, A. J., Mantle, M. D., & Gladden, L. F. (2021). Characterizing Solid–Liquid Interactions in a Mesoporous Catalyst Support Using Variable-Temperature Fast Field Cycling NMR. *The Journal of Physical Chemistry C*, *125*(16), 8767–8778. <https://doi.org/10.1021/acs.jpcc.1c00218>
- Washburn, K. E., & Callaghan, P. T. (2006). Tracking Pore to Pore Exchange Using Relaxation Exchange Spectroscopy. *Physical Review Letters*, *97*(17), 175502. <https://doi.org/10.1103/PhysRevLett.97.175502>
- Watson, G. C., Jensen, N. K., Rufford, T. E., Chan, K. I., & May, E. F. (2011). Volumetric Adsorption Measurements of N_2 , CO_2 , CH_4 , and a $\text{CO}_2 + \text{CH}_4$ Mixture on a Natural Chabazite from (5 to 3000) kPa. *Journal of Chemical and Engineering Data*, *57*(1), 93–101. <https://doi.org/10.1021/IE200812Y>

- Weber, D., Mitchell, J., McGregor, J., & Gladden, L. F. (2009). Comparing strengths of surface interactions for reactants and solvents in porous catalysts using Two-dimensional NMR relaxation correlations. *Journal of Physical Chemistry C*, *113*(16), 6610–6615. <https://doi.org/10.1021/jp811246j>
- Weber, D., Sederman, A. J., Mantle, M. D., Mitchell, J., & Gladden, L. F. (2010). Surface diffusion in porous catalysts. *Physical Chemistry Chemical Physics*, *12*(11), 2619–2624. <https://doi.org/10.1039/b921210h>
- Wilson, J. D. (1992). Statistical approach to the solution of first-kind integral equations arising in the study of materials and their properties. *Journal of Materials Science*, *27*(14), 3911–3924. <https://doi.org/10.1007/BF00545476>
- Witherspoon, V. J., Yu, L. M., Jawahery, S., Braun, E., Moosavi, S. M., Schnell, S. K., Smit, B., & Reimer, J. A. (2017). Translational and Rotational Motion of C8 Aromatics Adsorbed in Isotropic Porous Media (MOF-5): NMR Studies and MD Simulations. *Journal of Physical Chemistry C*, *121*(28), 15456–15462. <https://doi.org/10.1021/acs.jpcc.7b03181>
- Wu, T., Zhao, H., Tesson, S., & Firoozabadi, A. (2019). Absolute adsorption of light hydrocarbons and carbon dioxide in shale rock and isolated kerogen. *Fuel*, *235*, 855–867. <https://doi.org/10.1016/j.fuel.2018.08.023>
- Yang, X., Kleinrahm, R., McLinden, M. O., & Richter, M. (2020). Uncertainty analysis of adsorption measurements using commercial gravimetric sorption analyzers with simultaneous density measurement based on a magnetic-suspension balance. *Adsorption* *2020* *26:4*, *26*(4), 645–659. <https://doi.org/10.1007/S10450-020-00236-1>
- Yun, J.-H., Düren, T., Keil, F. J., & Seaton, N. A. (2002). Adsorption of Methane, Ethane, and Their Binary Mixtures on MCM-41: Experimental Evaluation of Methods for the Prediction of Adsorption Equilibrium. *Langmuir*, *18*(7), 2693–2701. <https://doi.org/10.1021/la0155855>
- Zhang, Y., Hirasaki, G. J., House, W. V., & Kobayashi, R. (2002). Oil And Gas Nmr Properties: The Light And Heavy Ends. *SPWLA Annual Logging Symposium*, SPWLA-2002-HHH.

Chapter 5 Quantitative Characterization of Methane Adsorption in Shale Using Low-field NMR

Foreword – The contents of this chapter is in preparation to be submitted to *Fuel* in 2022. It has been reformatted with minor amendments to fit the style and structure of this thesis. In this chapter we quantitatively estimate methane excess adsorption isotherms in two intact shale rocks within a range of pressures from 30 to 100 bar and at ambient temperature using low-field NMR techniques. The combination of mass balance calculation and integrated signal intensities of gas methane acquired from NMR measurements provides a potential approach to accurately detect the adsorbed and free gas compositions within shales at various pressures, and hence the prediction of potential production of shale gas reservoirs. The impact of organic matter and clay content on methane adsorption capacity in shales is also briefly considered. In future the characterization method will be extended to more shale samples with a wider range of total organic contents (TOC) and clay contents to determine their correlation with gas adsorption capacity in shales.

5.1 Abstract

Knowledge of adsorbed and free methane in shales is a critical requirement for the estimation of shale gas production and storage in shale gas reservoirs since the majority of shale gas production is sourced from those two components. Traditional gravimetric method evaluating sample mass change only provides information related to adsorbed methane whilst samples are destroyed after measurement are performed. Non-invasive low-field nuclear magnetic resonance (LF-NMR) is applied in this study to investigate excess methane adsorption capacity in two intact shale rock cores at a temperature of 24 °C and pressures up to 150 bar, with results compared to those from the gravimetric method. The resultant transverse relaxation time (T_2) spectra indicate three distinct population peaks with P1 ($T_2 < 1\text{ms}$) representing adsorbed methane in organic pores, P2 ($T_2=1\text{--}10\text{ms}$ and $10\text{--}100\text{ms}$ for the

two different shale rock samples) indicating gas methane constrained in inorganic pores and P3 (with the longest T_2 characteristic) corresponding to bulk gas methane in fractures and larger pore spaces. The amplitude of P1 initially increases rapidly with increasing pressures and approaches a plateau at approximately 100 bar whereas P2 and P3 increase linearly with pressure, consistent with this peak allocation. Excessive adsorption isotherms are acquired using a combination of mass balance calculation based on pump recording volume and pressure data and the determination of the P2 and P3 integrals from the NMR measurements. Results are in excellent agreement with those determined independently using gravimetric methods. The shale sample featuring low TOC but high-clay minerals shows a greater adsorption capacity compared to the organic-rich shale sample, suggesting that clay mineral rather than TOC contributes additional surface area and enhances the adsorption capacity of shales; this is consistent with the observations from scanning electron microscopy (SEM) but of course needs greater scrutiny in future with more samples being studied. Excessive adsorption isotherms obtained based on the integrated amplitude of P1 display a nearly identical curve trend but are reduced by a factor of 2-4 relative to that from gravimetric method for both samples; this is due to the pressure-independent NMR signal loss of the adsorbed methane component with short T_2 relaxation times. It is thus suggested that the LF-NMR and mass balance methodology is an accurate approach to obtain methane excessive adsorption isotherms in shales whereas the integrals of P1 may qualitatively but not quantitatively estimate methane excessive adsorption capacity.

5.2 Introduction

Natural gas production from unconventional tight/shale gas reservoirs has been playing an increasingly important role in world energy supply, accounting for more than 70% of the US total natural gas productions in 2020 (U.S. Energy Information Administration, 2021). Gas storage in shale preliminarily consists of three types: (1) free gas within pores and fractures; (2) adsorbed gas onto the nano-scale organic pore surface and (3) dissolved gas in hydrocarbon liquids and formation fluids (Chen et al., 2018; Javadpour et al., 2007; Wang et al., 2019). According to classification from the International Union of Pure and Applied Chemistry (IUPAC), pores with diameter less than 2 nm, between 2 nm and 50 nm and greater than 50 nm are defined as micropores, mesopores and macropores, respectively (Sing et al., 1985; Thommes et al., 2015). Dominated by those nano-scale pores featuring large pore surface areas,

gas adsorption has been considered as the most significant contribution to the estimation of the total shale gas reserve (Song & Kausik, 2019). The adsorbed gas can contribute greater than 50% of the total gas content in some shales, while the proportion of free gas ranges from 30% to 50% (Montgomery et al., 2005; Rani et al., 2015). The quantitative evaluation of adsorbed and free gas in shale is thus a critical consideration for the accurate prediction of gas-in-place and potential hydrocarbon production.

Gravimetry and volumetry methods based on adsorption isotherms are two widely employed methods to determine adsorbed gas content in shales (Belmabkhout et al., 2004; Wu et al., 2019; Wu et al., 2015). Those techniques, however, can only provide information relevant to adsorbed components rather than free gas content and samples employed in those methods normally need to be crushed, resulting in potentially enhanced adsorption capacity whilst destroying the original pore structure (Dick et al., 2017). Non-invasive and robust nuclear magnetic resonance (NMR) has become a powerful method to characterize pore structures and their confined hydrogen-bearing fluids (Coates et al., 1999; Kleinberg, 2001; Mitchell et al., 2013). Characterizations of methane adsorption in crushed shales has received limited investigation using low-field NMR in available literature with the consistent assumption that the adsorbed methane can be fully detected and the shortest T_2 is representative of adsorbed methane (Liu & Wang, 2018; Zhao & Wang, 2019). However, Yao et al. (2014) mentioned that adsorbed methane may only be partially detectable by low-field NMR and the correlation of T_2 amplitude to adsorbed methane may not be accurate. Moreover, the crushed shale samples are unable to maintain the original pore structures, leading to artificial fractures and potential overestimations or underestimations of adsorption capacity. Thus, a better understanding of methane adsorption in intact shale core plug then becomes critical to the estimation of methane adsorption behaviour in shales.

In this study, electron microscopy and energy dispersion spectroscopy (SEM EDS) were initially employed to measure microstructural and compositional details and the distributions of organic matter within the shale samples selected. Nitrogen adsorption/desorption analysis was used to characterize the pore structures (e.g. pore size distributions, surface area) of the shale samples. ^1H NMR Carr-Purcell-Meiboom-Gill (CPMG) measurements were then conducted to obtain T_2 distributions of methane on two shales at a range of experimental pressures up to 150 bar. 2D T_1 - T_2 maps were also acquired to help identify various proton populations of methane in shales. Resultant T_2 distributions were analyzed to obtain adsorbed, confined gas and bulk gas methane contents in shales during the

adsorption process as a function of pressure. Excess methane adsorption was obtained using a combination of T_2 amplitude corresponding to gas phase methane and mass balance calculation based on pump volumetric data. T_2 integrals of adsorbed methane were also directly correlated into adsorption molar amount based on a calibration between NMR signal intensity from bulk methane and the corresponding methane molar quantity. To this end, in order to validate those two methods, conventional gravimetric method was conducted on those same shale samples under identical pressure and temperature conditions as the above NMR measurements with the subsequent adsorption capacity isotherms directly compared.

5.3 NMR Background

NMR techniques have been extensively employed in the characterization of hydrocarbon-bearing porous media to evaluate pore size distributions and pore-confining fluids for example. NMR CPMG pulse sequences work by repeating a series of 180° pulses after an initial 90° pulse generating multiple echoes with a time difference between them known as the echo spacing (Hürlimann, 2012; Li et al., 2019; Mitchell et al., 2013). The NMR signal intensity acquired using a CPMG pulse sequence decays exponentially with T_2 according to (Carr & Purcell, 1954; Meiboom & Gill, 1958; Mitchell et al., 2013):

$$\frac{S(t)}{S_0} = \exp\left(-\frac{t}{T_2}\right) \quad (2.1)$$

where $S(t)$ is the measured signal intensity at time t (normally multiples of echo time), S_0 the maximum signal at $t=0$.

When a fluid is confined to a porous medium, interaction between fluid molecules and pore surface contributes to additional NMR signal relaxation (Kleinberg & Vinegar, 1996). When the methane gas saturates nano-scale pores in shales, gas adsorption forms a thin layer onto the pore surface, resulting in overall shorter T_2 relaxation times. As the pore sizes in shales are comparatively small, gas molecules will exchange between the bulk pore fluid and the adsorbed layer on the pore surface much more rapidly than the echo time of the CPMG train which is a requirement for the so-called fast diffusion limit (Washburn, 2014). Under this limit, the resultant T_2 relaxation becomes a weighted average of contributions from the pore bulk fluid and adsorbed layer as follows (Papaioannou & Kausik, 2015; Song, 2013; Washburn, 2014):

$$\frac{1}{T_2} = \frac{1}{T_{2,bulk}} + \frac{\delta S}{V_p} \times \frac{1}{T_{2,surface}} \quad (5.2)$$

where $T_{2,bulk}$ and $T_{2,surface}$ are the bulk relaxation and surface relaxation times respectively, δ is the thickness of the adsorption layer, S is the total surface area of the porous media, V_p is total pore volume. **Equation (5.2)** is generally expressed as (Song & Kausik, 2019):

$$\frac{1}{T_2} \approx \frac{1}{T_{2,bulk}} + \rho_2 \frac{S}{V_p} \quad (5.3)$$

where $\rho_2 = \delta/T_{2,surface}$ is the transverse surface relaxivity.

According to Bloembergen-Purcell-Pound (BPP) theory (Abragam, 1961), the longitudinal and transverse relaxation times arising from intramolecular dipolar interactions indicate a significant frequency correlation. The T_1 and T_2 times related to the rotational correlation time, τ , are expressed by (Fleury & Romero-Sarmiento, 2016; Song & Kausik, 2019):

$$\frac{1}{T_1(\omega)} = 2C \left(\frac{2\tau}{1+\omega^2\tau^2} + \frac{8\tau}{1+4\omega^2\tau^2} \right) \quad (5.4)$$

$$\frac{1}{T_2(\omega)} = C \left(6\tau + \frac{10\tau}{1+\omega^2\tau^2} + \frac{4\tau}{1+4\omega^2\tau^2} \right) \quad (5.5)$$

where C is a constant and ω is the Larmor frequency. T_1/T_2 ratio then becomes dependent of $\omega^2\tau^2$. Mobile molecules such as bulk fluids typically have a T_1/T_2 ratio slightly larger than 1 and solid-like materials such as organic matter and clay-bound water (with $\omega\tau \gg 1$) feature T_1/T_2 ratios several magnitudes greater than 1 and dependent on the Larmor frequency. Thus the T_1/T_2 ratio becomes a significant characterization of molecular mobility of hydrocarbon fluids in shales.

5.4 Experimental Section

5.4.1 Materials

Two shale rock cores, sourced from the outcrops of major shale plays, Eagle Ford (EF) and Mancos, with a length of 45 mm and a diameter of 25.4 mm (1 inch) were purchased from Kocurek Industries (USA). The masses of the EF and Mancos samples are 53.46 g and 55.56 g, respectively. Cores were cut perpendicular to the bedding plane, ensuring compositional and structural variations along the length of the core are minimized. Nitrogen injection

measurements were initially conducted on those two shale samples to determine porosity and permeability at various pressures using an A-608 automated permeameter-porosimeter (Coretest, USA). The porosity is 1.77% and 2.60% and permeability is 46.87 μD and 21.39 μD for the Mancos and EF samples respectively at a pressure of 1500 psi. The methane used in this study was purchased from Coregas (Australia) with a purity greater than 99.995%.

5.4.2 Total Organic Content

Shale samples cut from the same core plug used in this study were crushed, ground and sieved to a maximum size of twenty micro-meters. The crushed sample powders were then treated with concentrated hydrochloric acid (32%) for 4 hrs to remove carbonates. Samples were then flushed using deionized water and filtered with a glass fiber filter paper to remove both residual acid and the carbonate solution. After being oven-dried at 110 °C for more than 24 hrs, samples were combusted with the temperature at 900 °C to affect the pyrolysis of the organic content using a Vario MACRO Cube organic elemental analyzer (Elementar, Australia). The resultant CO₂ was collected and compared with a calibrated reference to determine total organic content. The measurement was repeated three times for each sample with the TOC results of 1.08% and 12.88% for Mancos and EF shale samples being produced respectively.

5.4.3 Scanning Electron Microscopy

Electron microscopy and energy dispersive spectroscopy (SEM EDS) was used to image 2D microstructural and compositional variations in fresh fracture planes of the shale samples; a Mira3 Oxford Tescan instrument (as shown in **Figure 5.1**) was. To allow for elemental surface mapping, sputter coating is not used, and images were acquired at moderate vacuum to aid dissipation surface charge buildup.



Figure 5.1. *Tescan Oxford SEM EDS (left) and freshly fractured surface of shale samples (right).*

SEM results indicated that the shale cores have a range of mineralogical compositions, micro-textures and organic materials. A key feature for the Mancos sample is that the organic matter occurs as isolated inclusions with very little associated porosity. This provides some evidence to indicate that the organic surface area available for adsorption is comparatively limited, and that correlation of adsorption to TOC in these cases could be misleading. As shown in **Figure 5.2**, the shale matrix of Mancos sample is dominated by clay and silicates and some apatite grains with the organic inclusion in the centre.

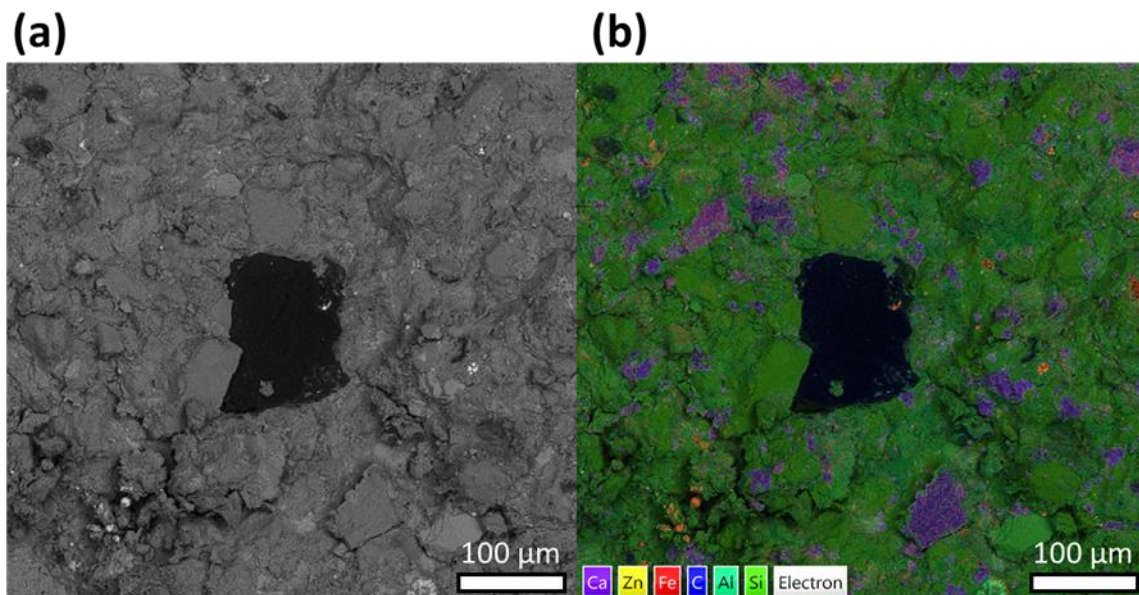


Figure 5.2. *(a) SEM image and (b) elemental map around an organic inclusion in the Mancos shale sample. The shale matrix is dominated by clay with minor carbonate and apatite content.*

In **Figure 5.3**, organic matter is observed as either large structured (often angular) organic inclusions, or amorphous organic matter interbedded with clays, and framboidal pyrite often occurs in conjunction with organic matter, particularly amorphous organic matter.

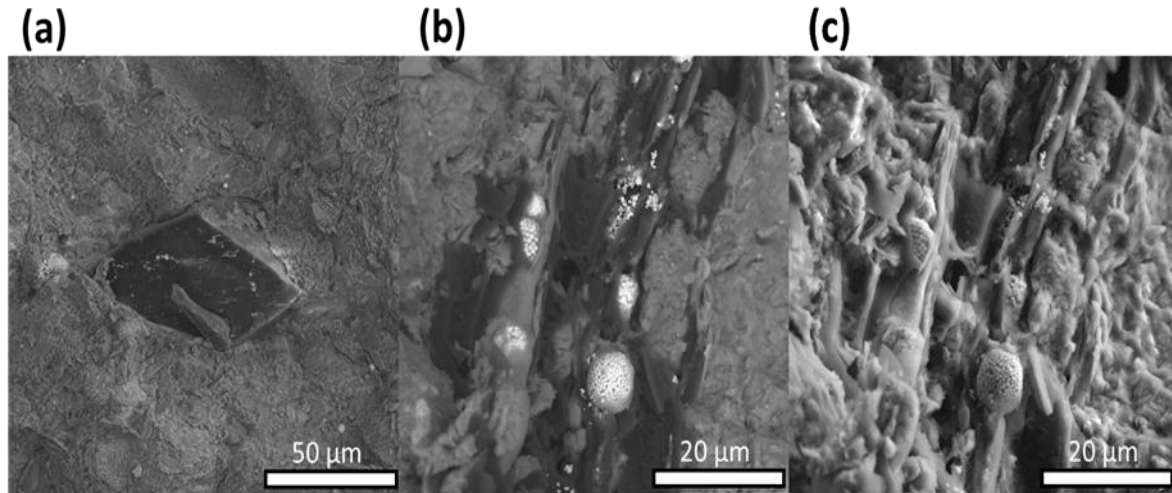


Figure 5.3. SEM images of the Mancos sample showing (a) structured organic matter imbedded in a shale matrix, (b) amorphous organic matter within framboidal pyrite, and (c) same spectrum point as shown in **Figure 5.3(b)** taken with secondary electron image showing organic matter interbedded with clay platelets.

SEM images for the EF sample are displayed in **Figure 5.4**, showing the shale matrix consists of microfossils infilling larger fossil fragments, apatite and silicate grains. The organic matter is mostly amorphous in nature and dispersed throughout the microfossil domains. Limited pyrite content primarily occurs as well formed framboids.

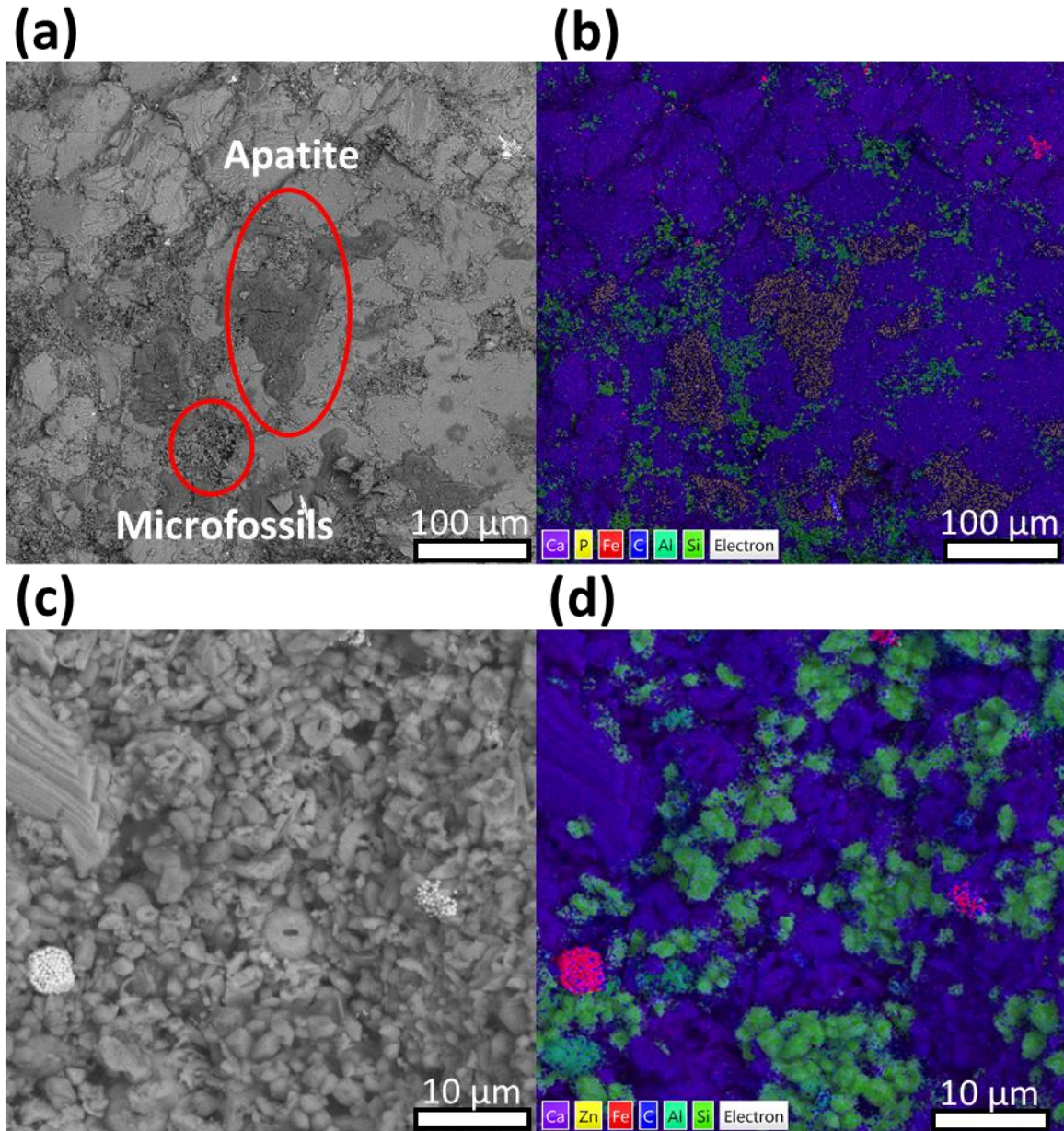


Figure 5.4. SEM images of (a) the EF shale, (b) corresponding elemental map of **Figure 5.4(a)**, microfossils sitting between larger apatite and crystalline carbonate grains; (c) zoomed in shot of the microfossils for the EF shale, and (d) corresponding elemental map of **Figure 5.4(c)**. Organic matter is hosted in microfossil matrix with occasional framboidal pyrite.

5.4.4 Nitrogen Adsorption/Desorption Isotherms

The characterization of the pore structure of those shale samples was conducted based on nitrogen isotherms at 77K using an ASAP 2020 accelerated surface area and porosity analyzer (Micromeritics, USA). Samples were heated up to 200 °C for 10 hours under vacuum to remove moisture and other volatile impurities before measurement. Sample surface area was

obtained by applying the Barrett-Joyner-Halenda (BJH) analysis to the isotherms for the relative pressure (P/P_0) ranging from 0.05 to 0.35. Pore size distributions were determined using the Barrett-Joyner-Halenda (BJH) analysis with a detective sensitivity of 4 Å. The isotherms of the samples are plotted in **Figure 5.5** with noticeable hysteresis loops, indicating a typical Type IV isotherm according to the classification from IUPAC (Sing et al., 1985; Thommes et al., 2015).

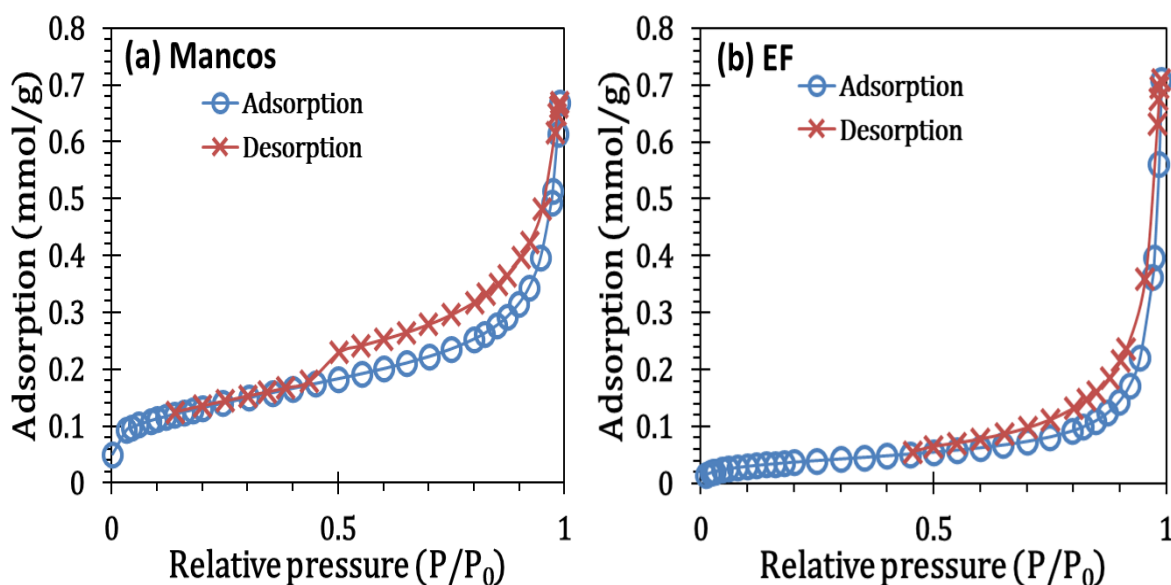


Figure 5.5. Nitrogen adsorption and desorption isotherms for (a) Mancos and (b) EF samples at a temperature of 77K.

The results obtained from analysis of those nitrogen adsorption and desorption measurements are summarized in **Table 5.1**. The surface area of Mancos sample is approximately three times greater than that of EF sample due to its much smaller average pore diameter.

Table 5.1. Summary of results from nitrogen adsorption/desorption measurements.

| | Mancos | Eagle Ford |
|--|--------|------------|
| BET surface area (m ² /g) | 10.68 | 3.15 |
| Averaged pore size (nm) | 6.40 | 15.98 |
| BJH adsorption Pore volume (cm ³ /g) (1.7-300 nm) | 0.021 | 0.024 |
| BJH desorption Pore volume (cm ³ /g) (1.7-300 nm) | 0.024 | 0.025 |

5.4.5 Gravimetric Adsorption

Gravimetric adsorption of methane on the shale samples were conducted along the isotherm $T \approx 24$ °C using a gravimetric sorption analyzer (Rubotherm, Germany, and since 2016, TA instrument, USA). Samples were heated under vacuum (activated) inside the measurement system at 150 °C for 12 hrs to remove residual moisture. The mass of the sample was determined after this activation and the volume of the sample was determined by measuring the buoyancy force on the sample in pure helium along a similar isotherm $T \approx 24$ °C in a pressure range from (0.01 to 8) MPa with the assumption that helium is not adsorbed on the sample. Weighing of the porous sample was conducted with an analytical balance (readability: 1 µg) via a magnetic-suspension coupling. An equilibration time of 30 to 60 minutes was allowed after a change in pressure, and the measurement at a given pressure generally lasted 20 to 40 minutes. The isothermal measurement was conducted twice to check the reproducibility. The noise-to-value ratio of the absolute adsorption is in the order of 0.5 and higher, mainly due to the high uncertainty of the sample volume and the low adsorption. The net adsorbed mass m_{net} on the adsorbent sample is as follows:

$$m_{net} = (W_1 - W_0)_{fluid}/\alpha - (W_1 - W_0)_{vac}/\alpha + \rho_{fluid} \times V_C \quad (5.6)$$

where ρ_{fluid} is the density of the fluid obtained from National Institute of Standards and Technology's (NIST) Chemistry WebBook (Lemmon et al., 2018), V_C is the volume of the sample container together with the lifting rods, W_0 and W_1 are the readings of the magnetic-suspension balance at the tare or zero position and measuring position respectively and α is the balance calibration factor. The subscripts 'vac' and 'fluid' denote that the measurements are conducted with the measuring cell evacuated and filled with fluid, respectively.

For a sample which does not adsorb the investigated gas (normally helium), the volume of the skeleton of the sample V_S can be easily calculated using:

$$V_S = -m_{net}/\rho_{fluid} \quad (5.7)$$

Then the excess adsorbed mass m_{ex} can be calculated as follows:

$$m_{ex} = m_{net} + \rho_{fluid} \times V_S \quad (5.8)$$

The corresponding excess adsorption capacity (N_{ex}) can be expressed as:

$$N_{ex} = \frac{(m_{ex}/M_{fluid})}{m_s} \quad (5.9)$$

where M_{fluid} and m_s are the molar mass of the adsorbate and the mass of the adsorbent, respectively.

5.4.6 NMR Experiments

A schematic of the instrument used in these NMR measurements is illustrated in **Figure 5.6**. An Oxford Instrument Geospec 12.7 MHz (^1H) NMR Rock Core Analyzer coupled with a P5 overburden cell (Green Imaging Technologies, Inc.) is employed in this study. Two syringe pumps (Teledyne ISCO 260D) are operating at constant pressure mode for gas and confining fluid injection and pressure maintenance. Pump flow rate and volume information is logged using a LabVIEW computer program (National Instruments Cooperation, USA). The samples were initially oven-dried at 110°C for 7 days until constant sample masses were recorded; they were then wrapped in a fluorinated ethylene propylene (FEP) heat shrink tubing and placed into the core holder. Following that, samples were vacuumed in the core holder using a vacuum pump (DS-102 Agilent Technologies) for at least 24 hrs prior to commencement of NMR measurements. Methane was then introduced into the rock core with the confining pressure (Maintained by fluorinert FC-40 oil) increasing simultaneously to maintain a differential pressure of 50 bar between the methane gas and the confining oil. Inlet and outlet pressures were monitored and recorded by two pressure transducers (Swagelok S Model). NMR measurements were conducted at a constant temperature of 24°C with a water bath supplying temperature control of the injected methane and confining oil. Measurements were conducted at a 10 bar increment of methane gas pressure up to 150 bar whilst the starting pressure was selected at 30 bar due to the limit of excessively poor NMR SNR at lower pressures. Background NMR signals sourced predominately from the core holder and shale rock core matrix under vacuum condition are subtracted prior to data analysis.

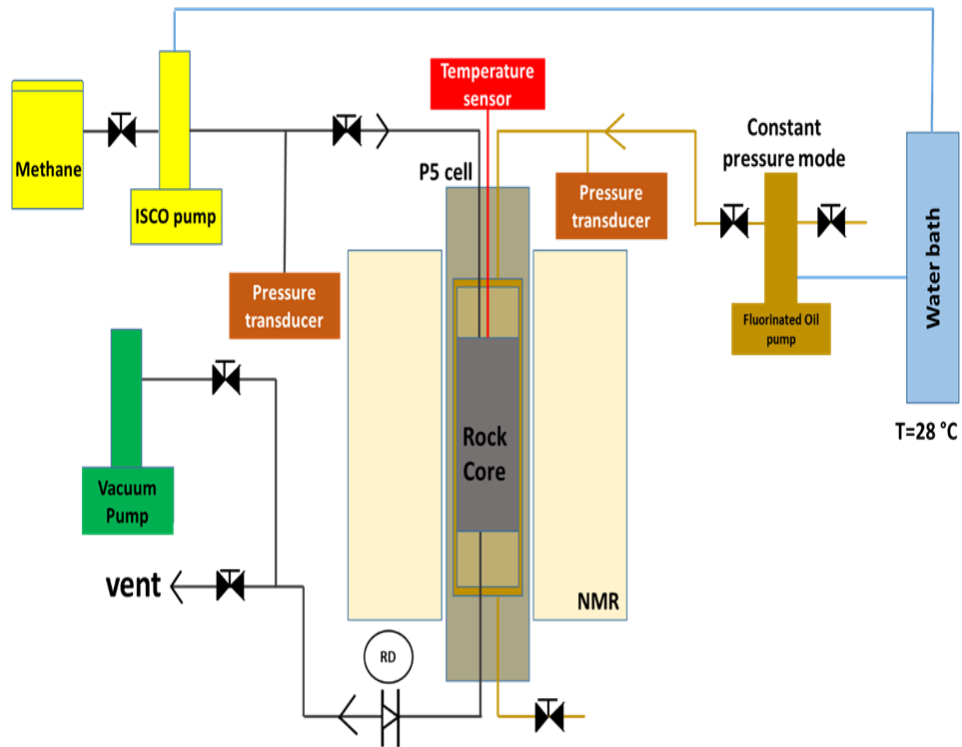


Figure 5.6. Schematic of experimental apparatus used in the NMR measurements.

The NMR pulse sequences used for CPMG and T_1 - T_2 correlation measurements (Mitchell et al., 2013) are schematically shown in **Figure 5.7**. NMR CPMG pulse sequences require the repetition of a series of 180° RF pulses after an initial 90° RF to generate multiple spin echoes separated by an echo time, T_E (Hürlimann, 2012; Li et al., 2019; Mitchell et al., 2013). For the CPMG measurements in this work, an echo time (T_E) of $100 \mu\text{s}$ was used with the number of echoes ranging from 5000 to 15000 such that the series of data attenuate to the noise level. A total of 64 scans and a recycle delay of 10s were applied to ensure a minimum SNR of 200. For the T_1 - T_2 correlation measurements, the relaxation times are measured using an inversion recovery pulse sequence followed by a CPMG echo train (Song, 2013). The indirect dimension (T_1) is encoded using various recovery times (τ_1) ranging from $100\mu\text{s}$ to 12s and the direct dimension (T_2) employs identical parameters to those used in the 1D CPMG measurements.

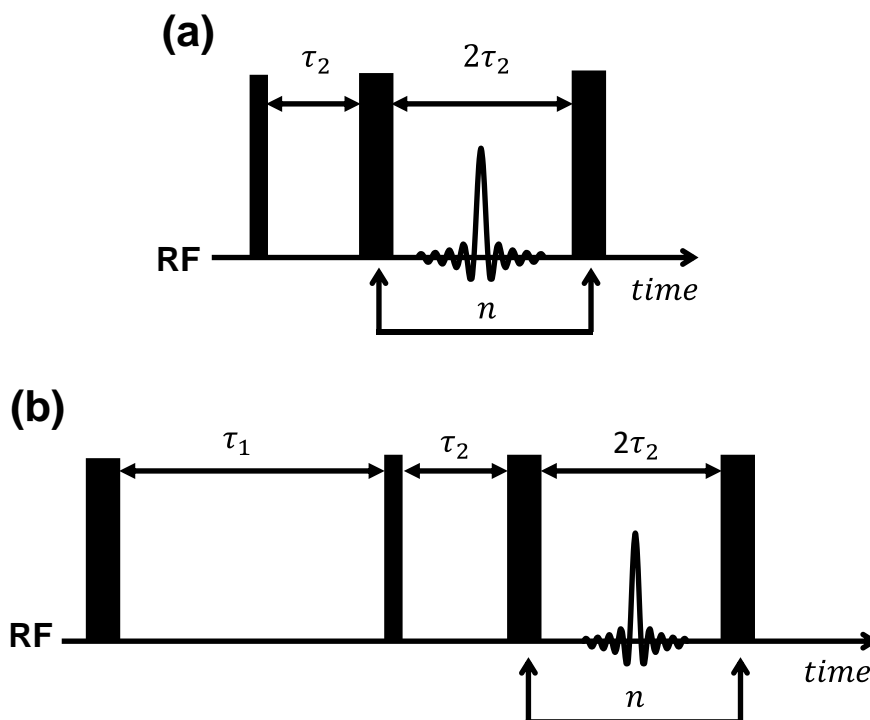


Figure 5.7. Schematic of the NMR pulse sequences for (a) CPMG measurements and (b) T_1 - T_2 inversion recovery-CPMG measurements. Thin and thick vertical bars represent 90° and 180° RF pulses, respectively. The echo time $T_E=2\tau_2$ and a range of τ_1 is repeated for the T_1 - T_2 measurements to encode T_1 .

5.5 Results and Discussion

5.5.1 Bulk Methane Calibration

NMR CPMG measurements were initially conducted on bulk gas methane at various pressures with a temperature of 24°C . The resultant bulk gas methane T_2 spectra are shown in **Figure 5.8(a)**. Both the T_2 peak values and area integrals increase as pressure increases. Using the specific methane molar density as a function of pressure, as obtained from NIST Chemistry WebBook (Lemmon et al., 2018) and the known volume of the sample holder space, the corresponding quantity of methane was readily calculated and plotted against the integrated area of each peak at various pressures with the number of averages of 64 in **Figure 5.8(b)**. A linear relationship with an excellent correlation ($R^2=0.9994$) is observed since the signal intensity is dependent of the number of ^1H protons, and hence the experimental pressures at a constant temperature. The correlations between methane quantity and NMR T_2 peak area signal intensity are calculated as follows:

$$N_{\text{methane}} = 1.2652 \times 10^{-5} \times A_{\text{methane}} \quad (5.10)$$

where N_{methane} is the number of methane moles (mmol) in the detection volume of the NMR apparatus and A_{methane} is the NMR signal intensity of the first CPMG echo.

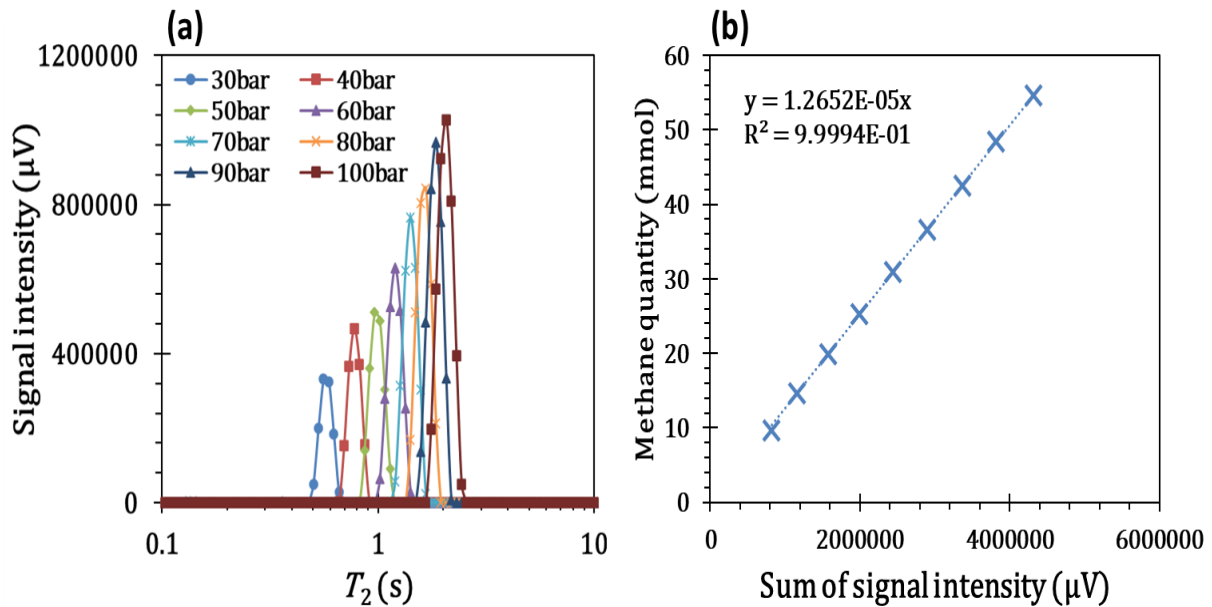


Figure 5.8. (a) T_2 spectra of bulk gas methane at different pressures. (b) The correlation between the sum of signal intensity of T_2 peaks and molar quantity of bulk gas methane in the pressure range from 30 bar to 100 bar.

5.5.2 NMR T_2 Distributions and T_1 - T_2 Maps of Methane in Shales

The T_2 spectra of methane in Mancos and EF shales at various pressures are plotted in **Figure 5.9(a)** and **5.9(b)**, respectively. The y-axis was updated to the methane amount according to **Equation (5.10)**. Based on the T_2 relaxation mechanism as shown in **Equation (5.3)**, methane in smaller pores tends to relax faster than that in larger pores when dominated by surface relaxation. For those two samples, the population peaks with $T_2 < 1$ ms (P1) are assigned to be adsorbed dominant methane in organic pores and negligible dissolved methane in organic matrix. The peak P1 integrals initially increase rapidly at low pressure range (below 100 bar) due to the existence of vacant surface sites, forming presumably monolayer adsorptions. For the EF sample, when the pressure increases to approximately 100 bar, adsorption reaches a plateau and slightly decreases as pressure increases further as the density of gaseous methane approaches that of adsorbed methane. The dominant methane population peaking approximately at 2 ms and 20 ms (P2) for Mancos and EF samples, respectively, are assigned as gas methane confined in inorganic pores. Compared to the Mancos shale, the longer

T_2 times of methane for P2 in EF samples are caused by a relatively larger average pore size, and hence weaker overall NMR signal surface relaxation. Peak P3 with T_2 ranging from 0.1 s to 1 s for EF shale are sourced from bulk gas methane in fractures and similarly large pores. However, for Mancos sample, multiple peaks are observed from the T_2 time of 0.01 s to 3 s, these partially overlap with each other. Considering their bulk-like long relaxation times, these peaks are all considered as effectively bulk relaxation dominated methane in different fractures and pore sizes and are labelled collectively as P3 as well. Notably, P3 components representing essentially bulk methane gas are not the main focus in this study.

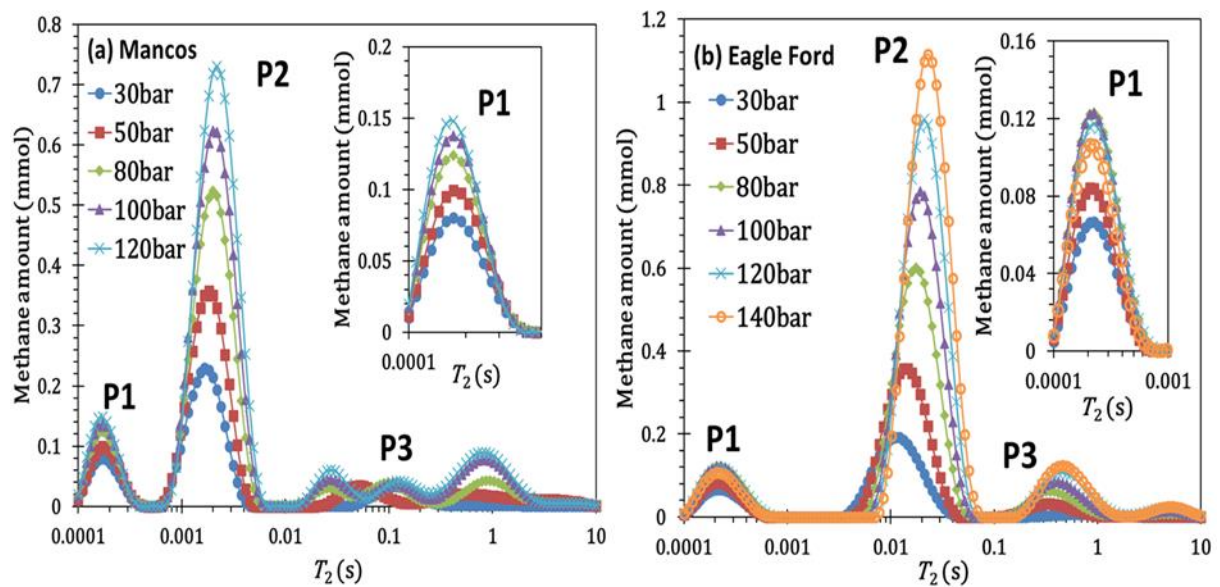


Figure 5.9. T_2 distributions of methane in (a) Mancos shale and (b) EF shale at different pressures. The P1 peaks of those two samples are reproduced in the inset as higher resolution.

Peak P1 is shown at higher resolution in the inserts of **Figure 5.9**. This clearly increases in area as pressure increases (despite a slight drop for the EF sample when pressure is above 100 bar), its mean or modal T_2 value is however unchanged. Regarding peak P2, this occurs at a larger value for the EF sample relative to the Mancos sample, consistent with the larger pore size measured for the EF shale (as reported in **Table 1**). As pressure increases, the peak area of P2 increases along with a subtle shift in the mean T_2 value indicative of a greater contribution from slightly larger pores towards this signal contribution. **Figure 5.10** shows the evolution in the corresponding methane quantity of P1-P3 as a function of pressure for both shale samples. Immediately evident is the linear increase in the methane quantity of peaks P2 and P3 with pressure. This dependency is consistent with bulk methane (**Figure 5.8(b)**) and the interpretations of P2 and P3 as methane in inorganic pores and large pores/fractures

respectively. The area of peak P1 initially increases with pressure before, at a pressure of approximately 100 bar, it plateaus. This trend is broadly consistent with simple monolayer adsorption. In the case of the Eagle Ford shale, a slight decrease in peak area is observed. This corresponds to the density of the gaseous methane approaching that of the adsorbed methane material.

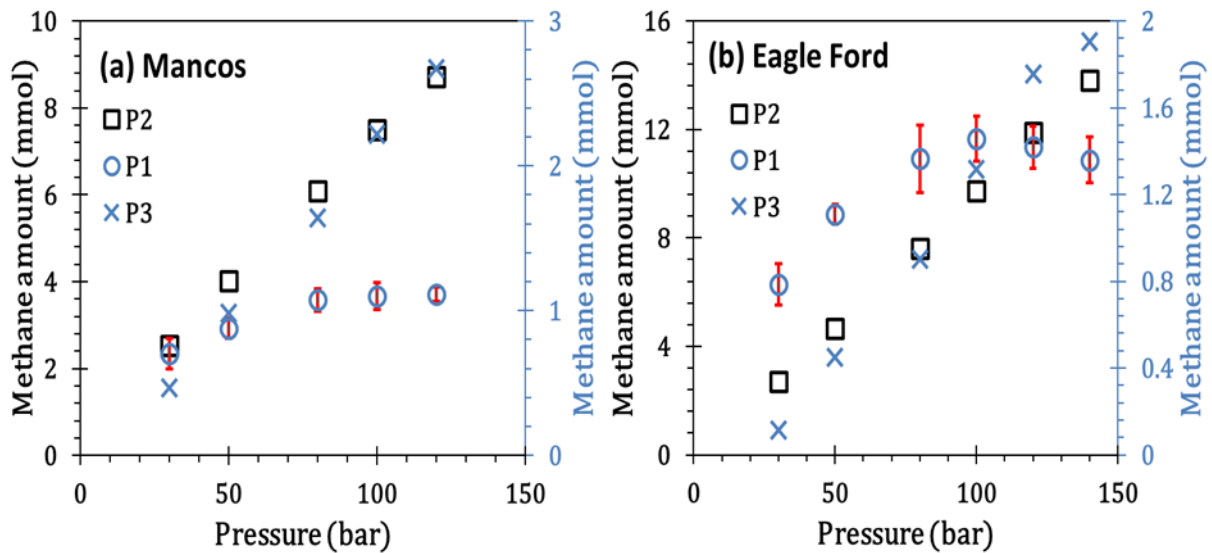


Figure 5.10. Relationships between experimental pressures and the corresponding methane amount of T_2 peaks of adsorbed methane in organic pores (P1), free gas methane in larger inorganic pores (P2) and bulk gas methane in fractures (P3) for (a) the Mancos shale and (b) the EF shale. Note P1 and P3 are plotted on the secondary vertical axis with different scales. Error bars for peak P1 are sourced from repeated NMR experiments.

Sample results of 2D T_1 - T_2 maps for methane in EF and Mancos samples at 50 bar and 100 bar are shown in **Figure 5.11**. These data are consistent with the 1D data shown in **Figure 5.9**; Peaks P1 -P3 are clearly distinct. Peaks P2 and P3 for both Mancos and EF samples present with T_1/T_2 ratios close to 1; this is indicative of comparatively limited adsorption and surface interaction and thus methane gas residing in fractures and inorganic pores. However in the case of peak P1, a significantly larger T_1/T_2 ratio is evident consistent with this peak being dominated by adsorption in organic pores.

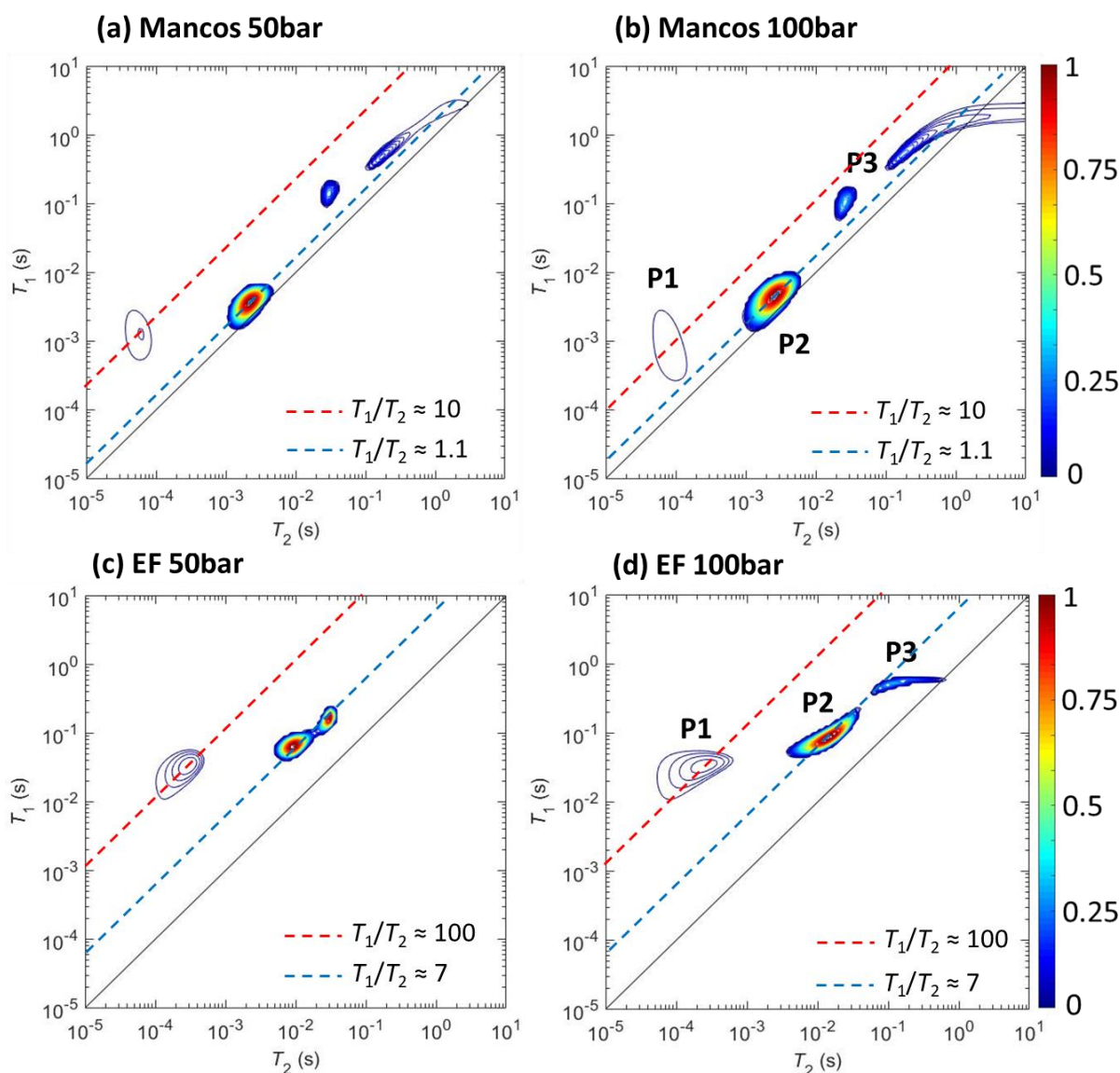


Figure 5.11. T_1 - T_2 maps of methane in (a) the Mancos shale at 50 bar, (b) the Mancos shale at 100 bar, (c) the EF shale at 50 bar and (d) the EF shale at 100 bar.

5.5.3 Evaluation of Methane Adsorption

Using **Equation (5.10)**, the signal intensities for the three peaks were converted into the amount of methane in units of mmol/g of shale. **Figure 5.12** presents these data as a function of pressure for peak P1. The equivalent (and independent) gravimetric data is also shown in **Figure 5.12**. For both shale samples, the NMR data significantly underpredicts the excess methane adsorption by a considerable amount. The most likely explanation for this is that methane NMR signal contributions with T_2 relaxation times that are shorter than 100 μ s

(T_E) are beyond the detectable range of the NMR instruments. The data inversion process to produce the T_2 distributions does not allow for T_2 values shorter than 100 μs (equals to T_E). Consequently the apparent T_2 peak values for peak P1 are 172 μs and 226 μs for the Mancos and EF shales respectively; however in reality these peaks might extend considerably below 100 μs . Thus we can conclude that peak P1 is considerably attenuated with significant loss of signal.

However also shown in **Figure 5.12** is the evolution in peak P1 multiplied by a constant; 3.6 and 1.9 for Mancos and EF respectively. Excellent agreement is clearly evident with the gravimetric measurements for both samples indicating that the fractional signal loss is interesting and somewhat surprisingly independent of pressure and that the attenuated data for peak P1 still faithfully captures the adsorption isotherm shape. This is reinforced by the two techniques (NMR and gravimetric measurement) reproducing a subtle reduction in excess adsorption with increasing pressure for the EF shale. Using these constants, we can estimate the real mean T_2 values for the two shale samples; these amount to 77 μs and 152 μs for the Mancos and EF shale samples respectively which is considerably lower than those that are measured.

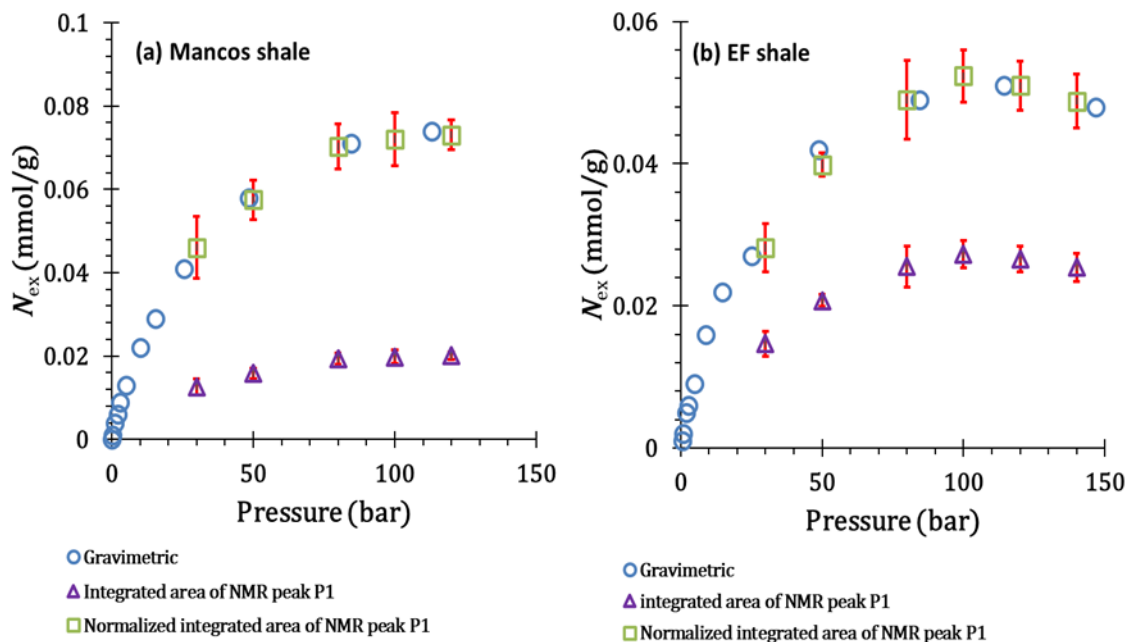


Figure 5.12. Comparison of excessive methane adsorption in (a) the Mancos shale and (b) the EF shale as a function of pressure. Blue circles are data obtained from gravimetric method; red crosses are sourced from the NMR peak P1 integrals; green squares are the normalized NMR peak P1 integrals by multiplying a constant.

We now consider an alternative methodology based on NMR to quantify the excess adsorption isotherms for the shales. This incorporates a mass balance based on methane volume using the supply pump data. Instantaneous pump and pipeline volumes and pressures are recorded at each equilibrium pressure and the corresponding methane molar amount are calculated as below:

$$\Delta N = (V_{pump,1} + V_{pipe,1}) \times \rho_{methane,1} - (V_{pump,2} + V_{pipe,2}) \times \rho_{methane,2} \quad (5.11)$$

where ΔN is the methane molar change between two equilibrium pressures, V_{pump} is the reading of methane volume in the pump, V_{pipe} is the volume of the entire pipeline, $\rho_{methane}$ is the methane molar density obtained from NIST Chemistry WebBook (Lemmon et al., 2018) and the subscripts 1 and 2 refer to different equilibrium pressures. Note that the shale samples fit completely within the NMR detection volume; thus ΔN is equal to the change of the sum of methane as measured by peaks P1-P3 at two different equilibrium pressures. In this case we avoid the use of peak P1 (which we know to be corrupted by signal relaxation) and use P2 and P3 to determine the excess adsorption amount based on **Equation (5.12)**:

$$\Delta N_{ads} = \Delta N - \Delta N_{gas} = \Delta N - 1.2652 \times 10^{-5} \times (\Delta A_{P2} + \Delta A_{P3}) \quad (5.12)$$

where ΔN_{ads} is the calculated change of adsorbed methane amount, ΔN_{gas} is the variation of total molar amount of gas methane and ΔA_{P2} , ΔA_{P3} are the changes in integrated area for P2 and P3 respectively. The resultant adsorption results thus obtained are plotted against those from the gravimetric adsorption measurements in **Figure 5.13** for both the Mancos and EF shale samples. Excellent agreement is produced between the independent NMR/mass balance methodology and that produced by the gravimetric method, including reproduction of the slight decrease in excess adsorption amount with pressure for the EF shale.

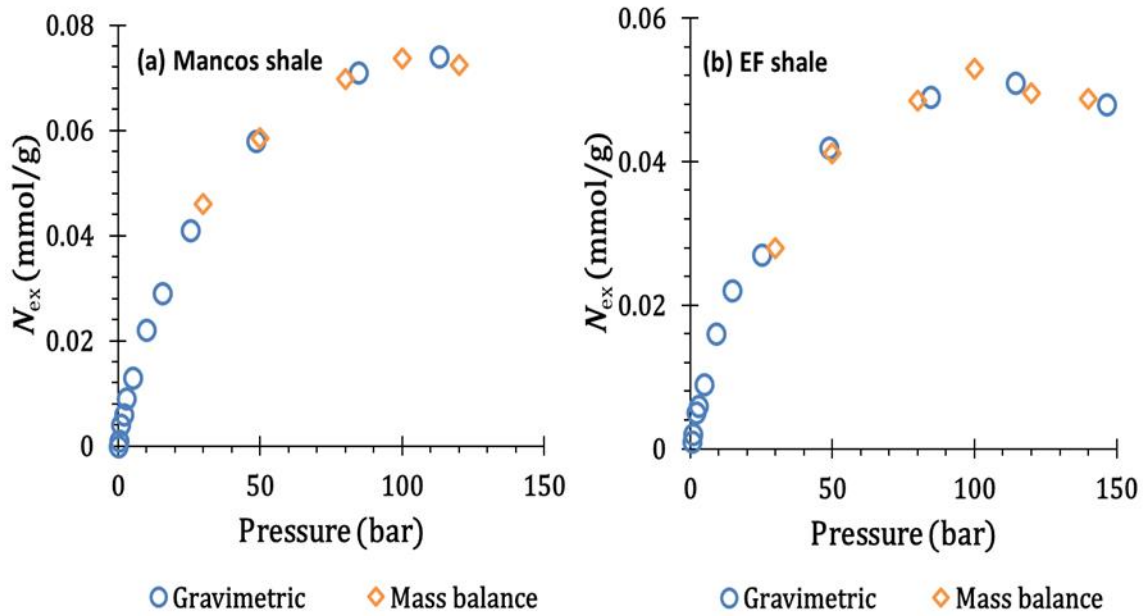


Figure 5.13. Excessive methane adsorption in (a) the Mancos shale and (b) the EF shale as a function of pressure. Blue circles are data obtained from gravimetric method; orange rhombuses represent adsorption data acquired from the combination of mass balance calculation and the corresponding methane quantity obtained from the integrated areas of NMR peaks P2 and P3 in **Figure 5.9**.

The adsorption isotherms for the two shale samples are roughly equivalent in magnitude. It appears that the much larger surface area of the Mancos shale sample (**Table 5.1**) is being effectively ‘compensated’ by the larger total organic content of the EF shale sample. This needs significantly more data to be validated however.

5.6 Conclusions

In this study, low-field NMR techniques are applied to investigate methane adsorption capacity at various pressures in two shale rock cores. NMR T_2 spectra are separated into three contributions, corresponding to adsorbed methane in organic pores (P1), effectively free gas in inorganic pores (P2) and bulk gas methane in fractures and/or large pores (P3). T_1 - T_2 maps are employed to confirm these methane population are not overlapping and correctly allocated. Methane adsorption isotherms are also obtained via a more conventional gravimetric method. Peak P1 was found to significantly underestimate excess adsorption; however it was able to accurately predict the shape of the adsorption isotherm. It was clear that peak P1 experienced significant signal loss due to T_2 content that was shorter than the lower NMR detection limit. However a combination of a volumetric-based mass balance from which the amount of

methane represented by peaks P2 and P3 (free methane in inorganic pores and fractures) were subtracted was able to quantitatively determine the system adsorption isotherm. As such this approach represents a novel and quantitative technique for NMR-based adsorption studies in intact shale plug samples.

5.7 References

- Abraham, A. (1961). *The Principles of Nuclear Magnetic Resonance*. Clarendon, Oxford.
- Belmabkhout, Y., Frère, M., & De Weireld, G. (2004). High-pressure adsorption measurements. A comparative study of the volumetric and gravimetric methods. *Measurement Science and Technology*, 15(5), 848–858. <https://doi.org/10.1088/0957-0233/15/5/010>
- Carr, H., & Purcell, E. (1954). Effects of Diffusion on Free Precession in Nuclear Magnetic Resonance Experiments. *Physical Review*, 94(3), 630-638. doi: 10.1103/physrev.94.630
- Chen, M., Kang, Y., Zhang, T., You, L., Li, X., Chen, Z., Wu, K., & Yang, B. (2018). Methane diffusion in shales with multiple pore sizes at supercritical conditions. *Chemical Engineering Journal*, 334, 1455–1465. <https://doi.org/10.1016/j.cej.2017.11.082>
- Coates, G., Xiao, L., & Prammer, M. (1999). *NMR logging: Principles and applications*. Halliburton Energy Services.
- Dick, M. J., Muir, C., Veselinovic, D., & Green, D. (2017). Measuring Methane Adsorption in Shales Using NMR. *Society of Core Analysts*, 1–7.
- Fleury, M., & Romero-Sarmiento, M. (2016). Characterization of shales using T_1 - T_2 NMR maps. *Journal of Petroleum Science and Engineering*, 137, 55–62. <https://doi.org/10.1016/j.petrol.2015.11.006>
- Hürlimann, M. D. (2012). Well Logging. *Encyclopedia of Magnetic Resonance*. <https://doi.org/10.1002/9780470034590.emrstm0593.pub2>
- Javadpour, F., Fisher, D., & Unsworth, M. (2007). Nanoscale gas flow in shale gas sediments. *Journal of Canadian Petroleum Technology*, 46(10), 55–61. <https://doi.org/10.2118/07-10-06>
- Kleinberg, R. L., & Vinegar, H. J. (1996). NMR properties of reservoir fluids. *Log Analyst*,

37(6), 20–32.

- Kleinberg, R. L. (2001). NMR well logging at Schlumberger. *Concepts in Magnetic Resonance*, 13(6), 396–403. <https://doi.org/10.1002/cmr.1026>
- Lemmon, E., McLinden, M., & Friend, D. (2018). *Thermophysical properties of fluid systems. In P.J. Linstrom, & W.G. Mallard (Eds.), NIST Chemistry WebBook, NIST Standard Reference Database Number 69.* National Institute of Standards and Technology, Gaithersburg MD, 20899. <https://doi.org/10.18434/T4D303>
- Li, M., Vogt, S. J., May, E. F., & Johns, M. L. (2019). In Situ CH₄–CO₂ Dispersion Measurements in Rock Cores. *Transport in Porous Media*, 129(1), 75–92. <https://doi.org/10.1007/s11242-019-01278-y>
- Liu, Y., & Wang, C. (2018). Determination of the Absolute Adsorption Isotherms of CH₄ on Shale with Low-Field Nuclear Magnetic Resonance. *Energy & Fuels*, 32(2), 1406–1415. <https://pubs.acs.org/doi/10.1021/acs.energyfuels.7b03428>
- Meiboom, S., & Gill, D. (1958). Modified Spin-Echo Method for Measuring Nuclear Relaxation Times. *Review Of Scientific Instruments*, 29(8), 688–691. doi: 10.1063/1.1716296
- Mitchell, J., Chandrasekera, T. C., Holland, D. J., Gladden, L. F., & Fordham, E. J. (2013). Magnetic resonance imaging in laboratory petrophysical core analysis. *Physics Reports*, 526(3), 165–225. <https://doi.org/10.1016/j.physrep.2013.01.003>
- Montgomery, S. L., Jarvie, D. M., Bowker, K. A., & Pollastro, R. M. (2005). Mississippian Barnett Shale, Fort Worth basin, north-central Texas: Gas-shale play with multi-trillion cubic foot potential. *American Association of Petroleum Geologists Bulletin*, 89(2), 155–175. <https://doi.org/10.1306/09170404042>
- Papadopoulos, A., & Kausik, R. (2015). Methane Storage in Nanoporous Media as Observed via High-Field NMR Relaxometry. *Physical Review Applied*, 4(2), 024018. <https://doi.org/10.1103/PhysRevApplied.4.024018>
- Rani, S., Prusty, B. K., & Pal, S. K. (2015). Methane adsorption and pore characterization of Indian shale samples. *Journal of Unconventional Oil and Gas Resources*, 11, 1–10. <https://doi.org/10.1016/j.juogr.2015.03.003>
- Sing, K. S. W., Everett, D. H., Haul, R. A. W., Moscou, L., Pierotti, R. A., Rouquerol, J., &

- Siemieniowska, T. (1985). Reporting Physisorption Data for Gas/Solid Systems with Special Reference to the Determination of Surface Area and Porosity. *Pure and Applied Chemistry*, 57(4), 603–619. <https://doi.org/10.1351/pac198557040603>
- Song, Y. Q. (2013). Magnetic resonance of porous media (MRPM): A perspective. *Journal of Magnetic Resonance*, 229, 12–24. <https://doi.org/10.1016/j.jmr.2012.11.010>
- Song, Y. Q., & Kausik, R. (2019). NMR application in unconventional shale reservoirs – A new porous media research frontier. *Progress in Nuclear Magnetic Resonance Spectroscopy*, 112–113, 17–33. <https://doi.org/10.1016/j.pnmrs.2019.03.002>
- Thommes, M., Kaneko, K., Neimark, A. V., Olivier, J. P., Rodriguez-Reinoso, F., Rouquerol, J., & Sing, K. S. W. (2015). Physisorption of gases, with special reference to the evaluation of surface area and pore size distribution (IUPAC Technical Report). *Pure and Applied Chemistry*, 87(9–10), 1051–1069. <https://doi.org/10.1515/PAC-2014-1117>
- U.S. Energy Information Administration. (2021). *Annual Energy Outlook 2021 (AEO2021)*. https://www.eia.gov/outlooks/aeo/pdf/AEO_Narrative_2021.pdf
- Wang, M., Huang, K., Xie, W., & Dai, X. (2019). Current research into the use of supercritical CO₂ technology in shale gas exploitation. *International Journal of Mining Science and Technology*, 29(5), 739–744. <https://doi.org/10.1016/j.ijmst.2018.05.017>
- Washburn, K. E. (2014). Relaxation mechanisms and shales. *Concepts in Magnetic Resonance Part A: Bridging Education and Research*, 43A(3), 57–78. <https://doi.org/10.1002/cmr.a.21302>
- Wu, T., Zhao, H., Tesson, S., & Firoozabadi, A. (2019). Absolute adsorption of light hydrocarbons and carbon dioxide in shale rock and isolated kerogen. *Fuel*, 235, 855–867. <https://doi.org/10.1016/J.FUEL.2018.08.023>
- Wu, Y., Fan, T., Jiang, S., Yang, X., Ding, H., Meng, M., & Wei, D. (2015). Methane adsorption capacities of the lower paleozoic marine shales in the Yangtze Platform, South China. *Energy and Fuels*, 29(7), 4160–4167. <https://doi.org/10.1021/acs.energyfuels.5b00286>
- Yao, Y., Liu, D., & Xie, S. (2014). Quantitative characterization of methane adsorption on coal using a low-field NMR relaxation method. *International Journal of Coal Geology*, 131, 32–40. <https://doi.org/10.1016/j.coal.2014.06.001>

Zhao, G., & Wang, C. (2019). Influence of CO₂ on the adsorption of CH₄ on shale using low-field nuclear magnetic resonance technique. *Fuel*, 238, 51–58.
<https://doi.org/10.1016/j.fuel.2018.10.092>

Chapter 6 Conclusions and Future Work

6.1 Conclusions

The main objective of this thesis was to ultimately develop experimental methodologies to quantitatively characterize both adsorbed and free gas methane in intact shale rock cores using low field ^1H NMR techniques. However initially, quantitative measurements of tortuosity in heterogeneous carbonate rocks were initially conducted as a precursor to shales. Bitumen content and capillary trapped water within shale rock cores were then characterized using a novel application of a simultaneous Gaussian and exponential data inversion. Those results were subsequently used to effectively underpin the characterization of short-chain hydrocarbon adsorption capacity in both model mesoporous silicas and shale rock cores. This thesis has demonstrated the utility of NMR techniques for obtaining gas adsorption isotherms in shales and has provided NMR experimental methods to quantitatively estimate adsorbed and gas methane amount in shales and thus to accurately predict gas productions from shale gas reservoirs. The following summarizes the novel insights and deliverables of the research detailed in Chapter 2 to 5 of this thesis:

Chapter 2 presented the quantitative measurements of tortuosity in heterogeneous carbonate rocks using pulsed field gradient NMR method. NMR-based experimental protocols for the measurements of high-pressure gas confined within porous media were established. The collective ‘diffusive’ tortuosity results acquired from NMR method were consistent as a function of both methane pressure (above 25 bar) and observation time used, consistent with the desired asymptotic limit being achieved. For three of the samples there was good agreement (within 10%) between ‘diffusive’ and ‘electrical’ tortuosity despite the very different tortuosity measurement methods used. In the case of Indiana carbonate there was no such good agreement, the measured ‘electrical’ tortuosity was significantly larger than the measured ‘diffusive’ tortuosity. This was hypothesized to be a consequence of the much larger pores present in this particular carbonate sample.

Chapter 3 demonstrated successful characterization of bitumen and capillary trapped water content in a range of shale samples with variable moisture content using multiple ^1H NMR frequencies (20, 40 and 60 MHz). A novel application of a simultaneous Gaussian and exponential (SGE) data inversion to spliced ^1H FID and CPMG NMR signal attenuation data to interpret proton populations originated from different components in the shale was utilized.

Gaussian peak areas of the shales were consistently independent of decreasing relative humidity and moisture content, suggesting that this signal was due to solid-like bitumen content in the shale. The magnitude of this Gaussian peak was then shown to scale with organic content. The exponential peaks areas showed excellent and consistent linear correlation with the increase in sample mass due to moisture addition. As relative humidity was reduced, moisture was observed to be removed first from larger inorganic pores featuring longer T_2 values. The standard deviation of the Gaussian component signal total was broadly consistent across the range of ^1H frequencies (20 to 60 MHz) and shale samples analyzed, indicating no systematic deterioration in NMR data quality as frequency was increased.

Chapter 4 presented the characterization of ethane dynamics within mesoporous silica materials exhibiting mean pore diameters between 6 and 50 nm using low-field ^1H NMR relaxation measurements, as a precursor to studies on gas adsorption in shales. NMR T_2 and diffusion coefficient distributions were acquired to separate the adsorbed ethane within intraparticle mesopores and bulk gas ethane within interparticle pores. Excellent agreement is observed through a direct comparison of NMR calculated excess adsorption capacities and gravimetric adsorption measurements, while T_2 and diffusion distribution data was demonstrated to provide unique insight into differing adsorption environments. Benchtop NMR was suggested as a potentially useful tool in the screening of short chain hydrocarbon adsorption phenomena within porous materials of relevance to gas separation and storage processes.

In *Chapter 5*, methane saturated in shale rock cores was quantitatively characterized in terms of adsorbed and free methane using low-field ^1H NMR techniques. NMR CPMG measurements were conducted on two intact shale rock cores at a temperature of 24 °C with pressure up to 150 bar. NMR T_2 spectra are separated into three components, corresponding to adsorbed methane in organic pores (P1), free gas in inorganic pores (P2) and bulk gas methane in fractures (P3). A combined application of mass balance and integrated NMR peak area was established to obtain NMR-based methane adsorption capacities. Excellent agreement was observed with adsorption isotherms obtained from a more conventional gravimetric approach. Clay minerals contributing additional surface area were found to be critical to the methane adsorption capacity in these shale samples whereas TOC content indicated no correlation with adsorption capacity. Organic surface area available for adsorption was limited based on the results from both SEM images and Brunauer-Emmett-Teller (BJH) surface areas applied to the two samples in this case.

6.2 Future Work

The results obtained during the completion of this PhD work have led to the following suggestions for potential future research programs:

6.2.1 Impact of organic content and clay minerals on methane adsorption capacities in shales

Preliminarily, results from this PhD work suggest that it is clay minerals rather than organic matter that play a significant contribution to the additional surface areas, and hence methane adsorption capacities in shales (Chapter 5). However, since only two intact shale rock cores have been investigated, this data set needs to be extended to a much wider set of shale rock samples with different proportions of clay minerals and organic matters. To achieve this, effective improvements in sample composition control are required. The use of synthetic shales varying the fraction of either clay minerals or organic matters while maintaining constant proportion of the other component will significantly help determine the influence of each material on methane adsorption capacities. To this end the UWA FSRR research group has developed compacted model shales in which composition can be systematically varied; a significant difficulty is in realising the low porosity of shale cores. The application of a simultaneous Gaussian and exponential (SGE) data inversion to spliced FID and CPMG NMR attenuation data to interpret proton populations originated from different components in the shale (Chapter 3) can also be used to calibrate the composition of organic content.

6.2.2 NMR measurements of ethane saturated shales

The integrated NMR signal intensities corresponding to adsorbed methane component cannot be directly correlated to methane adsorption amount since the part of the signal arising from adsorbed methane in nano-scale pores appears with relaxation times that are effectively faster than the NMR relaxation time lower detection point. Thus, the adsorbed methane is only effectively and partially detectable for low field ^1H NMR measurements. To overcome this, the use of probe fluids featuring relatively longer relaxation times such as ethane (Chapter 4) may become an alternative to enable complete detection of the adsorbed phase via NMR

instruments in shales. Since the bulk saturation pressure of ethane is approximately 40 bar at ambient temperature, the experimental pressure needs to be controlled below this point to enable the observation of adsorption behaviour. While an ethane pressure exceeding this point helps identify the pore structures in shales in terms of inter- and intra- particle pore spaces by avoiding the interference from the adsorbed phase since all ethane becomes liquid under this condition. Moreover, longer T_2 relaxation times of ethane may enable the application of PFG NMR measurements to acquire diffusion coefficients of the confining fluids. Considering a ten-times difference in diffusion coefficient for adsorbed phase and gas phase, the distributions of diffusion coefficient is a powerful tool to identify and quantify adsorbed and gas ethane in shales. NMR T_2 - T_2 exchange measurements will also be conducted to verify if diffusive coupling contributes significantly in the T_2 distributions obtained from CPMG measurements.

6.2.3 CO₂-CH₄ displacement in shales for enhance gas recovery (EGR)

Methane adsorption isotherms in shale rock samples at various pressures were measured using NMR. The injection of CO₂ into shale gas reservoirs to displace methane has become a method to not only enhance the gas recovery factor (EGR), but also mitigate the CO₂ emissions via a geo-sequestration approach. The physical mechanism of this technique is based on the higher adsorption capacity of CO₂ on organic pore surface than that of CH₄ (Kim et al., 2017; Rios et al., 2013) whilst the injected CO₂ can maintain the reservoir pressure and hence improve the sweep efficiency of the reservoir (Honari et al., 2016; Oldenburg et al., 2001). However, native natural gas and the injected CO₂ are fully miscible in all proportions at typical reservoir conditions, leading to early CO₂ breakthrough at gas producing wells and the very undesirable abandonment of the wells at the beginning production stage. Predictive reservoir simulations then become necessary to quantitatively estimate the risk of excessive mixing of CO₂ and CH₄ during EGR process. Accurate estimation of input parameters such as tortuosity and dispersion coefficient for the simulations is then required (Patel et al., 2016; Patel et al., 2017). Estimations of CH₄ adsorption capacity and the influence of the injected CO₂ on it during dynamic displacement within shales are significant to evaluate the effectiveness of the associated EGR process (Du et al., 2018). Thus, systematic experiments with respect to CO₂-CH₄ displacement in various shale samples to obtain both dispersion coefficients and dynamic CH₄ adsorption capacities are required.

To achieve this, improvements to the NMR-based experimental system to enable the injection of CO₂ into low permeability shale samples are required. An additional outlet pump is necessary to collect the effluent gas and maintain the system pressure. CO₂ breakthrough profiles need to be recorded using an *ex-situ* technique such as infrared spectroscopy to monitor the gas mixing processes. The employment of T_2 relaxation time measurements and the corresponding correlation between T_2 peak areas and methane molar amount combined with mass balance calculation introduced in this thesis offers a unique opportunity to investigate dynamic CH₄ adsorption isotherms after introducing CO₂ into shale cores under *in-situ* environmental conditions. Those results can be directly compared against those obtained from *ex-situ* measurements for validation purposes. The distributions of T_2 relaxation time of CH₄ in shale samples are distinguished into three regimes as adsorbed methane, free gas methane and bulk methane. With the dynamics of methane T_2 time distributions acquired during the displacing process, the influence of CO₂ injection on different types of methane within shales can be investigated by observing the peak area alteration of each individual methane component. Furthermore, additional measurements over a wider range of experimental parameters such as CO₂ injection rates and experimental pressures would enable better understanding of the displacing process.

6.2.4 References

- Du, X., Gu, M., Duan, S., & Xian, X. (2018). The Influences of CO₂ Injection Pressure on CO₂ Dispersion and the Mechanism of CO₂-CH₄ Displacement in Shale. *Journal of Energy Resources Technology, Transactions of the ASME*, 140(1). <https://doi.org/10.1115/1.4037687>
- Honari, A., Zecca, M., Vogt, S. J., Iglauer, S., Bijeljic, B., Johns, M. L., & May, E. F. (2016). The impact of residual water on CH₄-CO₂ dispersion in consolidated rock cores. *International Journal of Greenhouse Gas Control*, 50, 100–111. <https://doi.org/10.1016/j.ijggc.2016.04.004>
- Kim, T. H., Cho, J., & Lee, K. S. (2017). Evaluation of CO₂ injection in shale gas reservoirs with multi-component transport and geomechanical effects. *Applied Energy*, 190, 1195–1206. <https://doi.org/10.1016/j.apenergy.2017.01.047>
- Oldenburg, C. M., Pruess, K., & Benson, S. M. (2001). Process modeling of CO₂ injection into

natural gas reservoirs for carbon sequestration and enhanced gas recovery. *Energy and Fuels*, 15(2), 293–298. <https://doi.org/10.1021/ef000247h>

Patel, M. J., May, E. F., & Johns, M. L. (2016). High-fidelity reservoir simulations of enhanced gas recovery with supercritical CO₂. *Energy*, 111, 548–559. <https://doi.org/10.1016/j.energy.2016.04.120>

Patel, M. J., May, E. F., & Johns, M. L. (2017). Inclusion of connate water in enhanced gas recovery reservoir simulations. *Energy*, 141, 757–769. <https://doi.org/10.1016/j.energy.2017.09.074>

Rios, R. B., Stragliotto, F. M., Peixoto, H. R., Torres, A. E. B., Bastos-Neto, M., Azevedo, D. C. S., & Cavalcante, C. L. (2013). Studies on the adsorption behavior of CO₂-CH₄ mixtures using activated carbon. *Brazilian Journal of Chemical Engineering*, 30(4), 939–951. <https://doi.org/10.1590/S0104-66322013000400024>